MOLECULAR MODELING OF DIFFUSION IN CONDENSED ORGANIC SYSTEMS

A Dissertation

Presented to the Faculty of the Graduate School

of Cornell University

in Partial Fulfillment of the Requirements for the Degree of

Doctor of Philosophy

by

Yaset Miguel Acevedo

August 2018

MOLECULAR MODELING OF DIFFUSION IN CONDENSED ORGANIC SYSTEMS

Yaset Miguel Acevedo, Ph.D.

Cornell University 2018

Condensed organic molecules have distinct mechanical and electronic properties that differ from their metallic and organometallic counterparts. In the field of organic electronics, organic materials are an attractive alternative to inorganic materials due to their lower cost and inherent flexibility. In addition, organic molecules can be readily integrated into biological systems to perform functions on the molecular and cellular level. In this work, we explore three condensed organic systems using computational modeling methods. First, we investigate the formation of a heterojunction formed by two organic semiconductors: C_{60} growth on pentacene. This system is driven by an interest in flexible electronics, effective charge transport characteristics, and organic solar cells. Using coarse-grained molecular dynamics and kinetic monte carlo simulations, we elucidate the growth mechanics and surface morphology as a function of temperature. Second, we investigate the solution-phase structure of sulfonated oligothioetheramides (oligoTEAs), which will allow us to probe the interface between chemical sequence and macromolecular structure. By understanding the atomic and molecular configuration space, we can predict macromolecular binding and target recognition in biological contexts. Here, we were able to validate and illuminate the mechanics behind oligomer collapse using aqueous phase molecular dynamics. Finally, we characterize the mechanical and chemical properties of an organic woven material, COF-505, which couples the flexibility of organic molecules with the strength of covalent or-

ganic frameworks. Using molecular dynamics and a suite of optimization methods, we parameterize a force field describing this material. Subsequently, we characterize gas diffusion through COF-505 as a function of thermal and mechanical stress. While this new material has yet to be deployed in an applied setting, we expect this new hybrid material to have applications related to gas adsorption and carbon capture.

BIOGRAPHICAL SKETCH

Yaset Acevedo graduated *cum laude* with a Bachelor of Science degree in Chemical Engineering from the University of Notre Dame in 2012. He received the Naughton Fellowship to complete a one year masters program in Cork, Ireland. Yaset graduated with distinction with a Masters of Engineering Science degree in Sustainable Energy from University College Cork in 2013. He joined the doctoral program in Chemical Engineering at Cornell University in 2013, and received a Master of Science degree from this program in 2015.

Dr. Acevedo has received a number of honors and awards during his time at Cornell. He joined the doctoral program as a Cornell Colman Fellow in 2013. He received the Robert Mozia Graduate Student Distinguished Service Award in May 2015, the Outstanding Teaching Assistant Award within the Chemical Engineering department in May 2017, and the Austin Hooey Award in December 2017.

While studying at Cornell, Dr. Acevedo conducted an internship with ExxonMobil during the summer of 2017. His work in the ExxonMobil Upstream Research Company has led to an employment offer as a full time process engineer within the same research group.

Dr. Acevedo presented his research at a number of conferences, including the Spring 2016 Materials Research Symposium (MRS) Conference and the Spring 2017 MRS Conference.

Dr. Acevedo's dissertation *Molecular Modeling of Diffusion in Condensed Organic Systems* was supervised by Prof. Paulette Clancy.

To Carolyn, who challenges me and makes me smarter. To my parents, who taught me to reach for excellence. To my sister, who remains my oldest friend.

ACKNOWLEDGEMENTS

First and foremost, I would like to thank my advisor, Paulette Clancy, for her unwavering support and guidance. She taught me to balance the establishment of fundamental rigor and the production of valuable results, a core skill of a quality researcher. She is also an advocate of diversity and inclusion at Cornell and in academic communities, a trait that continues to inspire me. Professor Clancy continually enabled me to pursue my passions and career aspirations, which I will forever be grateful.

I would like to thank my committee members, James Engstrom (Chemical and Biomolecular Engineering) and Nandini Ananth (Chemistry and Chemical Biology) for their support and mentorship. I would like to thank Susan Daniel, who continues to promote the CBE Graduate Women's Group and fosters scientific outreach to the surrounding New York area.

I would also like to thank the Paulette Clancy group members who have intersected with my time at Cornell, particularly Aron Coraor, Ryan Heden, Henry Herbol, Brian Koo ('15), Alexandra Raymunt ('14), Mardochee Reveil ('18), Jonathan Saathoff ('16), Nikita Sengar, Blaire Sorenson, Victoria Sorg, James Stevenson ('16), and Jingyang Wang. Special mention goes to Rebecca Stehle (Cantrell) ('11) who provided the foundation of my work in Chapter 2 and continues to mentor me.

I would like to acknowledge my funding sources including the Cornell Sloan Fellowship and the Cornell Provost Diversity Fellowship.

TABLE OF CONTENTS

LIST OF TABLES

LIST OF FIGURES

CHAPTER 1

INTRODUCTION

1.1 Introduction to Modeling of Condensed Organic Systems

Condensed organic molecules form molecular crystals that have distinct mechanical and electronic properties that differ from their metallic and organometallic counterparts. This is primarily due to the fact that organic molecules interact predominantly through van der Waals forces, which have a weaker attraction potential and a bond energy lower than that of covalent or ionic bonds. This generally leads to low melting and sublimation temperature, low mechanical strength, and high compressibility.[4] Organic materials are an attractive alternative to inorganic materials due to their lower cost and inherent flexibility. In addition, organic molecules can be integrated into biological systems to perform functions on the molecular and cellular level.

One outcome of these weak intermolecular forces is that condensed organic crystals are prone to disordered metastable states. Experimental techniques can discern when crystallinity and its inherent properties are lost, but often cannot probe the mechanisms through which this disorder originates. Therefore, computational methods are essential to understanding the atomic and molecular morphology of condensed organic systems. The complete picture of an organic system can only be understood by coupling experimental and computational perspectives.

1.2 Systems of Interest

In this dissertation, we will look at three condensed organic systems that were investigated using computational modeling methods. First, we will explore the formation of a heterojunction formed by two organic semiconductors: C_{60} growth on pentacene.[5] This system is driven by an interest in flexible electronics, effective charge transport characteristics, and organic solar cells. Next, we investigate the solution-phase structure of sulfonated oligothioetheramides (oligoTEAs), which will allow us to probe the interface between chemical sequence and macromolecular structure.[2] By understanding the atomic and molecular configuration space, we can predict macromolecular binding and target recognition in biological contexts. Finally, we will characterize the mechanical and chemical properties of an organic woven material, COF-505, which couples the flexibility of organic molecules with the strength of covalent organic frameworks. While this new material has yet to be deployed in an applied setting, we might expect this new hybrid material to have applications related to gas adsorption and carbon capture.

1.3 Modeling Work Flow: Verification, Validation, Property Prediction

Computational models such as Molecular Dynamics and Kinetic Monte Carlo, can resolve the atomic and molecular morphology of organic systems. However, model credibility must be established before scientists can be expected to extrapolate information based on model predictions. Specifically, the model developer must ascertain that: 1) the mathematical equations governing the model are implemented

correctly, and 2) the model is an accurate representation of the underlying physics of the problem. To achieve these goals, it is preferable for the methodologies and data from both computational and experimental methods to be combined. Only when validated should computational predictions be performed. Proper verification and validation increases peer acceptance and helps to bridge the gap between computational chemists and experimentalists.[6] All three systems studied in this dissertation follow this process of verification and validation prior to engaging in any property predictions. The author asserts that prospective model developers should follow these best practices to maximize the impact of their work.

CHAPTER 2

MULTILAYER HETEROEPITACTIC GROWTH OF C_{60} ON PENTACENE

2.1 Introduction

2.1.1 Organic Electronic Devices

The study of thin film growth has been a staple of materials research for decades [see, for example, refs. 7–9]. More recently, there has been increased interest in studying the growth kinetics of organic semiconductor thin films on organic substrates,[10–16] driven by applications related to display technologies and RFID tags, light-emitting diodes, field effect transistors, and solar cells. So-called "pi-conjugated" small molecules (*e.g.*, pentacene and the other acenes, thiophenes, *etc.*) have dominated organic electronics since they are thermally stable (to about $400°C$), capable of being created in an ultra-pure fashion, and can be readily grown in ultra-high vacuum systems.

One critical aspect of organic semiconductor electronic device performance is the ability of the heterojunction formed between adjacent electron-conducting and hole-conducting layers to efficiently separate the excitons formed when light is absorbed. The efficiency of exciton splitting depends sensitively on the structure of the heterojunction[16], but molecular-level details of the interfacial structure are generally not well known, and they vary across the interfacial surface. This provides the impetus for molecular-scale computational studies which are suited to address such tiny length scales and provide some clarity as to the evolving nature of the

interfacial structure as growth proceeds.

2.1.2 Background on the System

Previous Work on C_{60} Growth on Pentacene

Despite the importance of the heterojunction to facilitate charge separation, large-scale morphological computational studies of molecular-scale organic semiconductor heterojunctions are still relatively uncommon [17–19, for instance]. Computationally intensive *ab initio* simulations have been used to probe small fragments of the heterojunction (typically around 100 atoms) to determine whether very local atomic-scale morphological differences affect charge transport, *e.g.*, in polymeric semiconductors[20], and for the C_{60}/pentacene interface studied here.[21,22] *Ab initio* studies provide binding energies at the heterojunction that are valuable input into larger-scale calculations. But their computational intensity means that they can have nothing more to say about the growth (in terms of structure or kinetics) of multiple layers of a deposited organic molecule on a dissimilar organic substrate that will be the focus of this paper.

Non-equilibrium dynamics of growth are also important since the ability to grow large crystalline domains and reduce defects affects the scalability of large-scale manufacturing processes. Experiments show that attempts to grow C_{60} on pentacene cause C_{60} to dewet the pentacene surface.[23] Growth experiments by Breuer and Witte show that this dewetting is exacerbated by temperature and is shaped by the presence of pentacene terraces.[24] The nature of the C_{60} aggregates changes from a 2D structure at low temperature to 0D clusters along the pentacene step edges at higher temperatures.

Since C_{60} and pentacene each prefer different crystal habits, thin film growth for these systems is an example of heteroepitactical growth. [In contrast, heteroepitaxy concerns situations in which A and B materials share the same preferred crystal habit (*e.g.*, Si on Ge).] There have been just two prior reports of KMC simulation of heteroepitactic growth; one uses a multi-lattice KMC method we created and applied to sub-monolayer growth.[1] In the second, Hoffman investigated how environmental conditions of a CO molecule on a Pd (100) surface (*e.g.*, different adsorption site geometries) determined which of the two lattices (CO or Pd) it adopted.[25] Unlike Hoffman's method, our algorithm[26] did not require the two dissimilar lattices to match at the periodic boundary conditions, which effectively changes the lattice parameters.

Growth of pentacene on C_{60} is, interestingly, quite different from growing C_{60} on pentacene. The former was studied using MD for an impressively long time (60 ns).[27] They showed that the second layer of pentacene starts to grow before the first is finished, and the third starts before the second is finished, emulating the experimentally observed behavior of pentacene growth on pentacene.[11] This follows Volmer-Weber growth, which is characterized by the formation of discrete islands on a surface. Based on their calculations and our previous work on sub-monolayer growth,[26] we anticipate that growing C_{60} on pentacene is also likely to follow this mode.

To summarize, there has been a dichotomy of approaches used to look at fullerene/pentacene interfaces: *ab initio* studies have studied small motifs of the interface to explore charge transport, while larger-scale all-atom Molecular Dynamics simulations have uncovered the motifs that dominate the interfacial morphology. To date, there has been no simulation study of multilayer growth of a fullerene

on pentacene and hence a determination of the growth habit of this system. A large gap in length- and time- scales exists between the morphological predictions of MD simulations and experiment, and it is unclear how best to bridge them from a computational viewpoint.

2.1.3 Project Objective

Our approach here will be to observe the growth kinetics as we deposit fullerene molecules on a pentacene surface. *Ab initio* studies are too resource-intensive to consider as the preferred simulation technique and, indeed, the best computational approach to take for this system, is unclear. The mesoscale "reach" of a lattice-based Kinetic Monte Carlo (KMC) is attractive, but we might expect strained heteroepitactic growth to involve off-lattice events of (*a priori*) unknown importance. For KMC, we can anticipate issues in terms of both the effort required to generate all the needed energy barriers and, of more concern, whether a lattice-based approach can capture the transition from the triclinic structure of pentacene to the FCC-dominated C_{60}. Our earlier work suggested that a multilayer KMC approach can be constructed.[26] But Cantrell's results were only shown for sub-monolayer growth and new computational issues may well arise as we consider a multilayer growth process, as will be described here.

Molecular Dynamics offers an alternative to KMC, since it has no limitation associated with the constraint of pre-defined lattices. In practice, our goal of studying multiple layers of deposition renders the use of an all-atom approach infeasible. Simulations of the stepped pentacene surface require a sufficiently wide area of the lower terrace relative to the height and area of the step. This requirement defines the configuration of our system (in terms of $x - y$ dimensions). For this layout,

it would be prohibitively expensive in terms of computing resources to consider the deposition of more than a hundred C_{60} molecules using an all-atom approach. Unfortunately, 100 C_{60} molecules would cover less than two monolayers and our interest in studying multiple layers of deposition would be infeasible. To circumvent this problem, we will use a coarse-grained MD simulation (CGMD) to study the multilayer growth of C_{60} on pentacene, particularly in the presence of pentacene terraces. C_{60} molecules are stabilized by pentacene step edges and form aggregates as a function of temperature[24]. But can a model for C_{60} be coarse-grained with sufficient accuracy to capture the details of a multilayer growth process *via* this simpler, faster MD simulation approach?

Lattice-based KMC and CGMD can both be thought of as representing different ways of "coarse-graining" the system, and both offer access to mesoscopic regimes. In addition, as a means of validating and expanding the results of the on-lattice KMC, we developed a reaction-diffusion continuum model for sub-monolayer growth, which essentially coarsens the system's description even further and brings us closer to experimental length- and time-scales.[5] We expect that the kinetic trapping and aggregation of C_{60} molecules shown experimentally will lead to different thin film morphologies. A continuum approach will help us understand how detailed a description of the intermolecular interactions is really needed to follow the key growth characteristics of this unusual system. The goal of our model is to describe the size distribution of clusters that form by diffusion of adatoms on the original substrate and reaction at a cluster surface during sub-monolayer growth. While simpler models exist,[28–30] none of them deal with a cluster size distribution. Instead, they model the surface coverage corresponding to various numbers of layers. Also, none of the models solve the problem of transport on a substrate among a random array of clusters and the diffusion-limited flux to the cluster which is

the main focus of our model. Trofimov and Mokerov [28] solve a transport problem for diffusion on top of an island and stepping down to the next level. The other models use the strategy of Tomellini and Fanfoni [31], which has the number of atoms in a cluster growing at a constant rate independent of any transport problem and, in some cases, clusters merging or coalescing when they contact. Our reaction-diffusion continuum model and the results pertaining to C_{60} growth on pentacene will be presented in this chapter.

This chapter will determine the merits and drawbacks of each approach (2D reaction-diffusion modeling, KMC, and CGMD) to model multilayer thin film growth processes *in the presence of a terrace*. Including the terrace is important: Firstly, steps are invariably present during growth processes and, secondly, it affords a comparison to the more recent experimental data of Breuer and Witte in whose work the presence of the step edge was critical. No simulations of multilayer growth in the presence of steps exists in the literature for this system and, indeed, for very few other systems. Consideration of all three approaches will allow us to offer recommendations of the best computational approach to capture the nuances of epitactical growth processes, from sub-monolayer to multilayer growth, which has, so far, not been possible, nor explored.

2.2 Simulation Methods

2.2.1 Kinetic Monte Carlo

Kinetic Monte Carlo (KMC) uses a library of known transitions to study multilayer surface growth. Since standard KMC codes are unsuited to study heteroepitactic

growth, we previously developed an algorithm tailored to do so, and hence follow the growth of C_{60} on pentacene.[1] The algorithm featured a multi-lattice framework with a seamless ability to switch "grids" from those suitable for pentacene and C_{60} to match the selected event.

In the revised (2nd generation) version of the code described here, we added interlayer diffusion for the C_{60} molecules and removed any possibility that molecules in the 2nd and higher monolayers can occupy the same space upon deposition. Importantly, we also added the ability of C_{60} molecules to dewet, that is, to jump up from the C_{60} layer sitting on the pentacene substrate onto a C_{60} island by computing the relevant energy barrier for this event (essentially a reverse Schwoebel barrier). The energy barrier for dewetting was calculated to be 0.23 eV at 300 K, which is surprisingly low, and reflects the preference of C_{60} to cluster.

Beyond the growth of a first monolayer, the interaction of C_{60} with other C_{60} molecules begins to dominate the kinetics of the system and more closely resemble the hexagonal bulk lattice characteristic of C_{60} molecules. Accordingly, deposition events in the multiple-layer code involve determining whether or not a C_{60} molecule is deposited onto a C_{60} "triangle" (a three-fold hollow site). In the 1st generation code, if a molecule was posited to land on such a triangle, the deposition event was ignored. In the multiple layer version of the KMC code, a C_{60} molecule may be deposited onto any layer, except in grain boundaries where only off-lattice sites exist. The requirement that a C_{60} molecule must always stay on top of a C_{60} "triangle" imposes two constraints on the KMC simulations: 1) C_{60} molecules cannot move into and across grain boundaries where only off-lattice sites exist, and 2) C_{60} molecules underneath a higher layer C_{60} are "frozen" in place since their movement would violate the requirement for a three-fold hollow site. These inhibitions on

movement and position prevent higher C_{60} monolayers from achieving full coverage once the grain boundaries have been established on the 1st C_{60} monolayer. These effects can be seen in the KMC results, especially during multilayer growth.

The 1st-generation code produced [110]-shaped islands of C_{60} molecules in the first monolayer[1], which we considered an artifact caused by the slightly asymmetric jump rates that resulted from the stochastic nature of the MD-derived data. Accordingly, in the current multiple layer version of the code, we set the jump rates in opposite directions to be the same. In addition, pentacene lattice jump rates were tuned to meet the constraint of "detailed balance" for a temperature of 300 K. This reduces the occurrence of anisotropic island shapes for C_{60} deposition on the pentacene film and dampens any net C_{60} motion that stems from jump asymmetry. However, due to the presence of multiple lattices and the unequal effect of temperature on the jump rates, the constraint of "detailed balance" is difficult to achieve and can only be approximated within the error of the calculated jump energy barriers.

A final consideration involves the presence of pentacene terraces, which exist on real thin films. In CGMD, it is relatively straightforward to insert a small terrace, say, one monolayer high, as in this work. In KMC, adding a terrace is less straightforward. To accurately simulate multilayer C_{60} growth in the presence of a pentacene terrace, an extensive library of additional moves would need to be generated for jumps up onto, and down from, the pentacene wall. To avoid having to create this additional library, we approximated the *pentacene* step by a fixed, three-layer high, C_{60} step along the center of the simulation box. The height of three C_{60} molecules is similar to the height of a monolayer of pentacene. The hex lattice transition library naturally promotes C_{60} aggregation and permits upward

growth. In this manner, we allow the KMC code to approximate the pentacene steps present in the experimental system.[24]

2.2.2 Coarse-Grained Molecular Dynamics (CGMD)

CGMD allows us to address the greatest weakness of lattice-based KMC, namely consideration of off-lattice behavior. This is critical for capturing C_{60} aggregation along pentacene step edges and C_{60} island coalescence and multilayer growth. A periodic 10 nm x 13 nm thin film pentacene surface was simulated using LAMMPS, Sandia's widely used Molecular Dynamics software package[32]. Since we are interested in comparison to experiments that feature monolayer pentacene steps, we included a representative pentacene step that was eight pentacene molecules wide, one layer deep, and spanned the entire length of the simulation box (to emulate the typically long terraces in experiments). We determined that eight pentacene molecules constituted the smallest acceptably stable step width; smaller pentacene walls resulted in the wall decomposing (falling apart) at simulation temperatures higher than 400 K. The pentacene step accounts for 18% of the total surface area.

Coarse-grained C_{60} molecules, modeled as a single sphere (details in the next paragraph), were randomly generated a fixed height ($\sim$35 Å) above the pentacene surface and directed toward the surface at -1.1 Å/ps (0.045 eV), to emulate the experimental conditions used by Breuer and Witte for their studies of C_{60} growth on pentacene[24]. An isothermal, NVT, ensemble was implemented in the MD simulation using a Nosé-Hoover thermostat to maintain a set of temperatures from 100 K to 500 K, in 100 K intervals. Similar to the KMC simulations, the deposition rate was significantly increased to 1 C_{60} molecules per 5 ps (or 7.7 x 10^8 monolayers per second) in order to achieve the deposition of experimentally relevant quantities of

C_{60} molecules at computationally feasible time scales. For sub-monolayer growth, 65 C_{60} molecules were deposited over 400 ps in order to approximate the 0.5 nm coverage used in the study by Breuer and Witte.[24] For multilayer studies, 390 C_{60} molecules were deposited (the quantity required to complete three monolayers) and the simulations were run proportionally longer (2 ns).

The quality of the coarse-grained C_{60} model will strongly influence the accuracy of reproduction of monolayer and cluster growth morphologies. But coarse-graining C_{60} molecules is aided by the fact that the molecules are approximately spherical, rigid, unreactive, and charge-neutral. Indeed, many coarse-grained models exist for C_{60}.[33–35] We chose to use a recent united-atom model by Lim[36] which generated a Mie-like (m,n), or Lennard-Jones-like, potential in which m = 35.5 and n = 8.87. The Lim model represents a simplification of a model by Liu and Wang[35] that was parameterized using experimental data and optimized for use in MD. All the referenced models[33–35] seem to be comparable in accuracy. We chose Lim's model because it can be readily implemented in LAMMPS. The OPLS (Optimized Potentials for Liquid Simulations) force field was used to model the pentacene substrate due to its accuracy for modeling condensed phase organic molecules[37]. We used surface diffusion coefficients calculated from MD simulations to validate Lim's coarse-grained model for C_{60} against our previously published all-atom simulations[38]. The resulting surface diffusion coefficients from CGMD were within an order of magnitude of the previously published values, with an average percentage error of 78%. We considered this to be an acceptable difference.

2.3 Parameterization of Energy Barriers

2.3.1 Calculation of Reverse Schwoebel Barrier

The ability for a C_{60} molecule to jump up from the pentacene onto a C_{60} layer (essentially a reverse Schwoebel barrier) absent from the previous list of allowed transitions in the first-generation code. Results from CGMD and experiments[24] suggested that not only was this transition possible, it was critical to the 3D growth present at higher temperatures.

CGMD (as opposed to "all atom" MD) was used to calculate the reverse Schwoebel barrier in order to reduce the computational cost. An adsorption energy map of C_{60} on the thin film pentacene generated using CGMD compares favorably with the "all atom" model used with previous transition barrier calculations[26].

While an isolated C_{60} prefers the low energy sites (from which the QP lattice is derived), aggregated C_{60} molecules are more strongly attracted to each other than they are to the surface. The net effect is that many C_{60} molecules are forced onto unfavorable adsorption sites, as can be seen in Figure 2.2. While some periodicity is suggested by the image, the lattice mismatch inherent in this system means that an infinitely large C_{60} sheet will assume an approximately even distribution of C_{60} sites.

The reverse Schwoebel barrier is correlated with the energy of adsorption. By assuming a constant transition state energy (derived from our energy barrier calculations) and assuming an even distribution of adsorption sites, we were able to calculate the average Schwoebel energy barrier as a function of temperature and number of C_{60} neighbors. Values for the Schwoebel barrier at 300 K are shown in

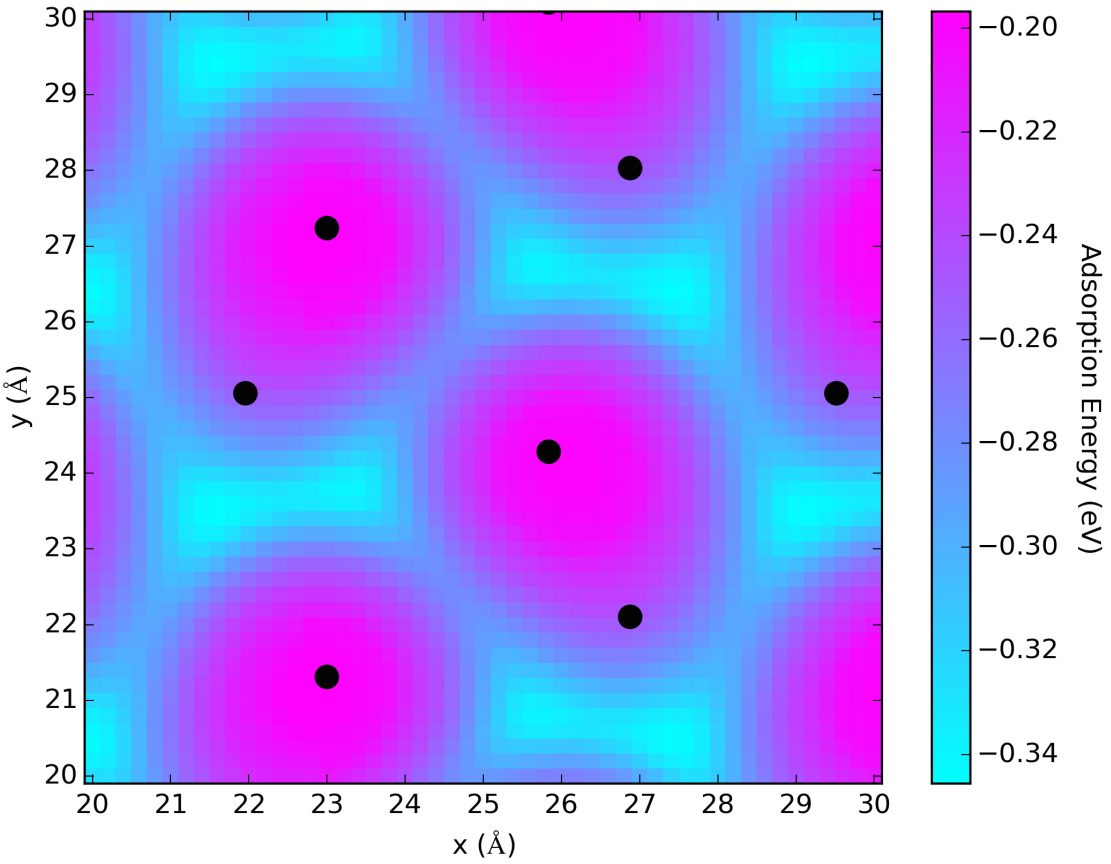

Figure 2.1: Adsorption energy maps of C_{60} on thin film pentacene. The black dots indicate the location of the top hydrogen positions of the pentacene molecules with which the C_{60} molecules are in contact. Magenta colors signify high-energy areas; aqua colors signify low-energy areas.

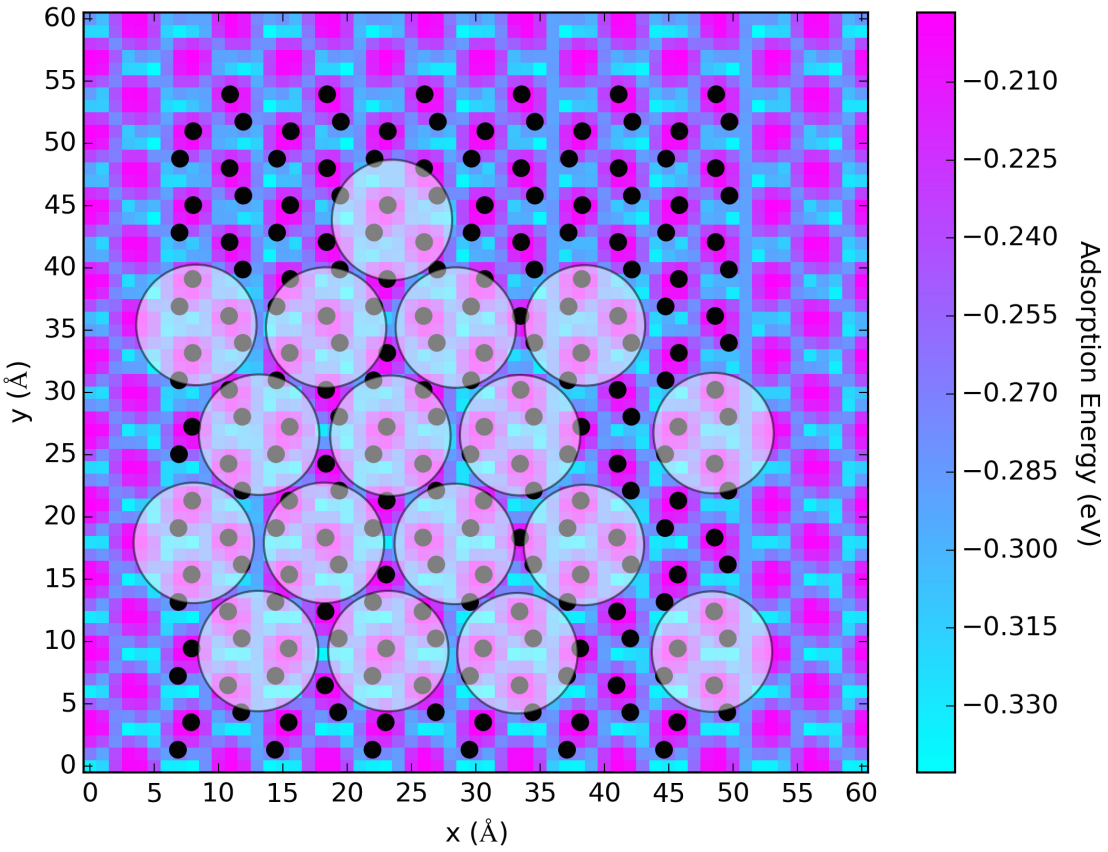

Figure 2.2: Relaxed CGMD C_{60} sheet superimposed onto an adsorption energy map. The black dots indicate the location of the top hydrogen positions of the pentacene molecules with which the C_{60} molecules are in contact. The transparent white circles indicate the location and approximate size of the C_{60} molecules. The C_{60} molecules prefer low energy (aqua) sites but may accept the compromise of adopting high energy (magenta) sites due to the abiity to be attracted to other C_{60} molecules.

Table 2.1: Reverse Schwoebel Barrier

Neighbors	2	3	4	5	6
Transition State Energy (eV)	0.017	0.267	0.542	0.840	1.108
Avg. Energy Barrier at 300K (eV)	0.231	0.481	0.756	1.101	1.322

Table 2.1.

2.4 Validation of Models

2.4.1 Diffusion Coefficients

As an additional confirmation of the continuum model, we compared the calculated diffusion coefficient for C_{60} on bulk phase pentacene at 300 K for the KMC model[38] (5 x $10^{-4} cm^2/s$), all-atom MD model[38] (2 x $10^{-4} cm^2/s$), and continuum model (0.5 x $10^{-4} cm^2/s$).[5] Since diffusion is not easy to determine accurately, we consider agreement within an order of magnitude to be good. The continuum model provides the benefit of being able to simulate slow deposition rates (*e.g.*, 1 monolayer per second), which are not accessible using the KMC code. However, this continuum method is valid only for two-dimensional, sub-monolayer growth, where clusters are assumed not to impinge upon one another.

2.4.2 CGMD Radial Distribution Function

As a measure of the crystallinity of the C_{60} thin film, the radial distribution function g(r) was calculated, which describes the density as a function of distance from

a reference particle. Figure 2.3 shows g(r) plotted as a function of temperature.

Overall, the g(r) functions show little variation with temperature (Figure 2.3) and a high degree of crystallinity. This demonstrates that the C_{60} - C_{60} interaction is stronger than its C_{60} - pentacene equivalent and does not conform to the pentacene lattice.

2.4.3 CGMD: Formation of C_{60} Monolayers

In order to generate the Nth Layer Coverage graph in Figure 2.14, we had to first determine how to assign each deposited C_{60} to a particular monolayer. Because of the frequent off-lattice movement of the C_{60} molecules, it was difficult to know *a priori* if the C_{60} molecules could be assigned to a specific monolayer. To investigate this, the $z-$ position of every deposited C_{60} molecule at every time step was plotted on a single graph, as shown in Figure 2.4 for two temperatures, 100 K and 500 K. Subsequently, the height data was processed into a histogram to determine the peak C_{60} locations, as shown in Figure 2.5.

As an FCC crystal, the distance between C_{60} layers on the vertical axis is equal to the *sphere diameter* $* \sqrt{(3)}/6$. The united-atom model by Lim[36] prescribes the C_{60} diameter as 10.048 Å. We used this information to calculate the theoretical monolayer heights of a perfect FCC C_{60} lattice. Comparing the theoretical monolayer heights with the simulated CGMD monolayer heights in Table 2.2, we find there is excellent agreement between the two sets of values. The observed split peaks represent portions of monolayers 3 and 4 that settled slightly higher or lower due to underlying gaps or defects in monolayers 1 and 2. Having confirmed that the deposited CGMD C_{60} molecules behave like a FCC crystal, we used these

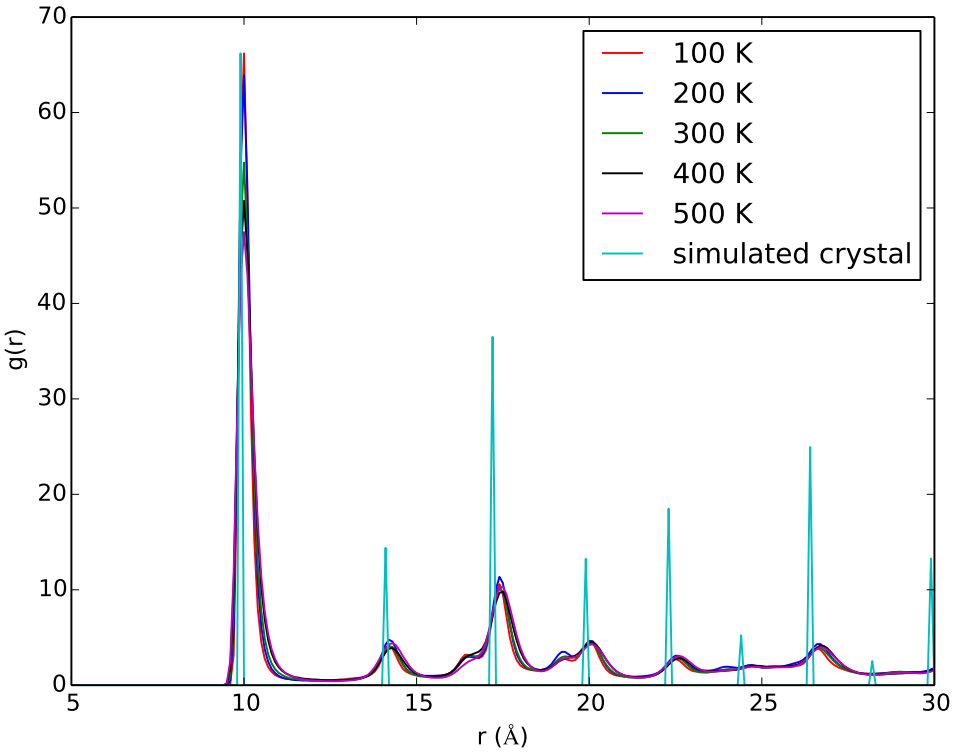

Figure 2.3: Radial Distribution Function, g(r) of a C_{60} thin film as a function of temperature.The lattice sites for 1st-9th NN are represented by the ideal, delta function curves for a perfect C_{60} [FCC] lattice (aqua). All the simulations showed significant crystallinity, regardless of temperature. This indicates that the C_{60} - C_{60} interaction dominates over the effects of the C_{60} - pentacene surface/terrace interactions.

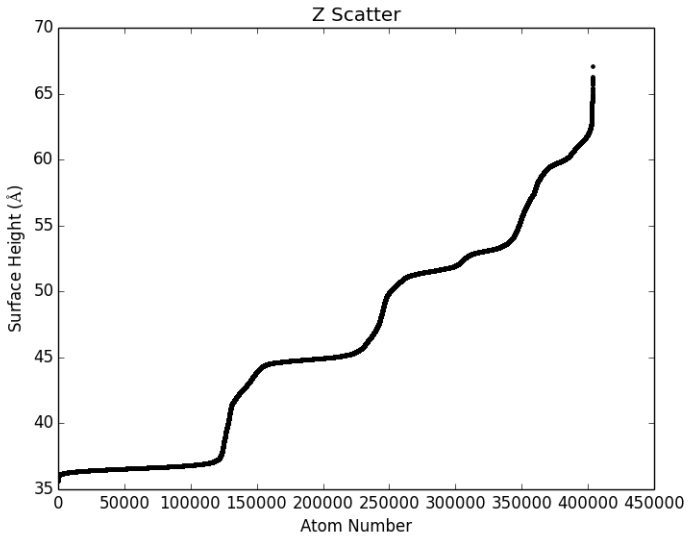

100 K

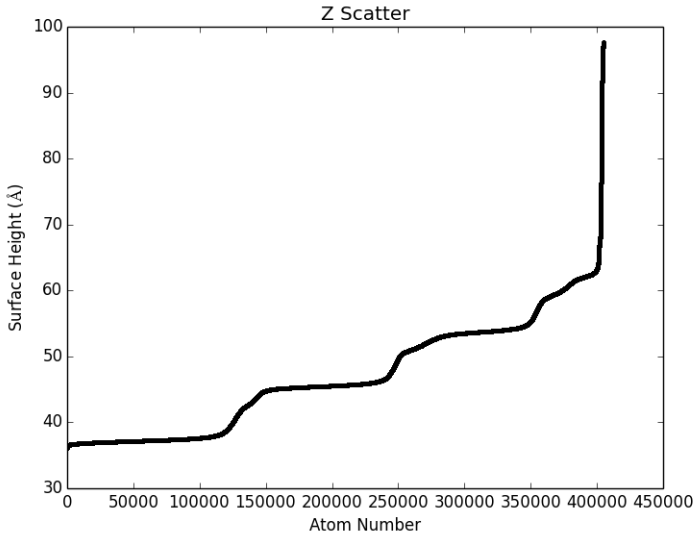

500 K

Figure 2.4: Cumulative scatter plot of all z positions of every deposited C_{60} molecule at every time step for the 2 ns CGMD depositions.

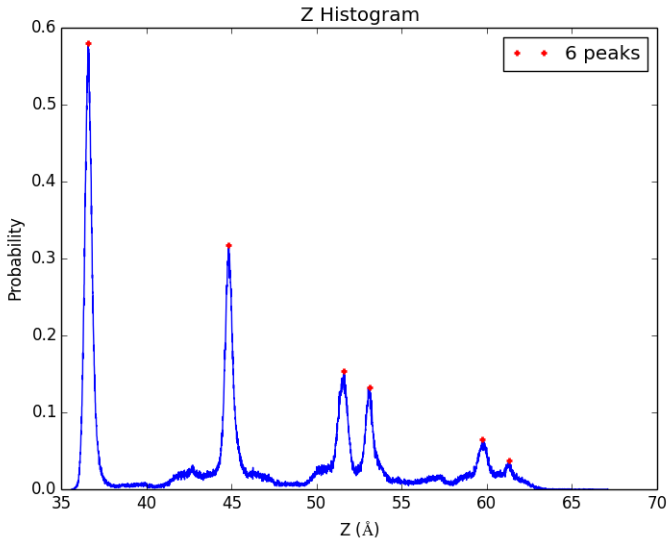

100 K

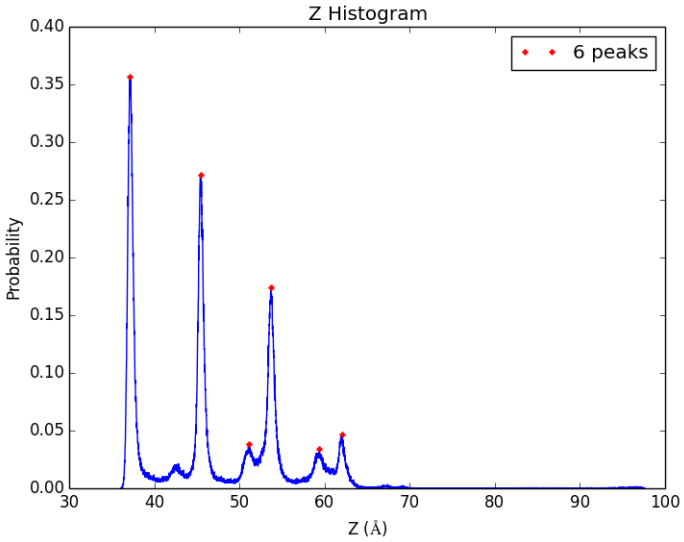

500 K

Figure 2.5: Histogram data for the z positions of deposited C_{60} molecules for the 2 ns CGMD depositions. 400 bins used.

Table 2.2: Monolayer Height (Å)

Theoretical Peaks	Simulated Peaks (100 K)	Simulated Peaks (500 K)
36.6 (ML 1)	36.6	37.1
44.8 (ML 2)	44.9	45.4
53.0 (ML 3)	51.6; 53.1	51.1 53.7
61.2 (ML 4)	59.7; 61.3	59.4; 62.1

theoretical monolayer values to generate the Nth Layer Coverage graph presented in Figure 9.

2.4.4 Sub-Monolayer Growth: CGMD Results and Comparison to Experiments

We used CGMD to explore the growth of a sub-monolayer of C_{60} at a step edge of a pentacene terrace. Emulating the experimental results, we observed a clear preference for C_{60} to adhere to the step-edge wall by comparing simulation results at 100 K and 400 K, as shown in Figure 2.6. At 100 K, deposition is dominated by C_{60} interactions with the pentacene surface, producing anisotropic growth of numerous small clusters along energetically favorable pentacene valleys. These fullerene clusters were distributed roughly evenly across the pentacene surface, as shown in Figure 2.6. In contrast, at 400 K, the picture shows compact islands dominated by fcc-like C_{60}-C_{60} interactions, and a preference for the islands to be located at the step edge. Indeed, the molecules are capable of "climbing up" the step edge, and can form a contiguous line from the flat terrace below to the top of the step edge. Both of these observations mirror the low and high temperature experimental results of Breuer and Witte, validating both the Lim CG model and the simulation approach. Without the computational efficiency of the CG fullerene model, this large-scale simulation would not have been possible.

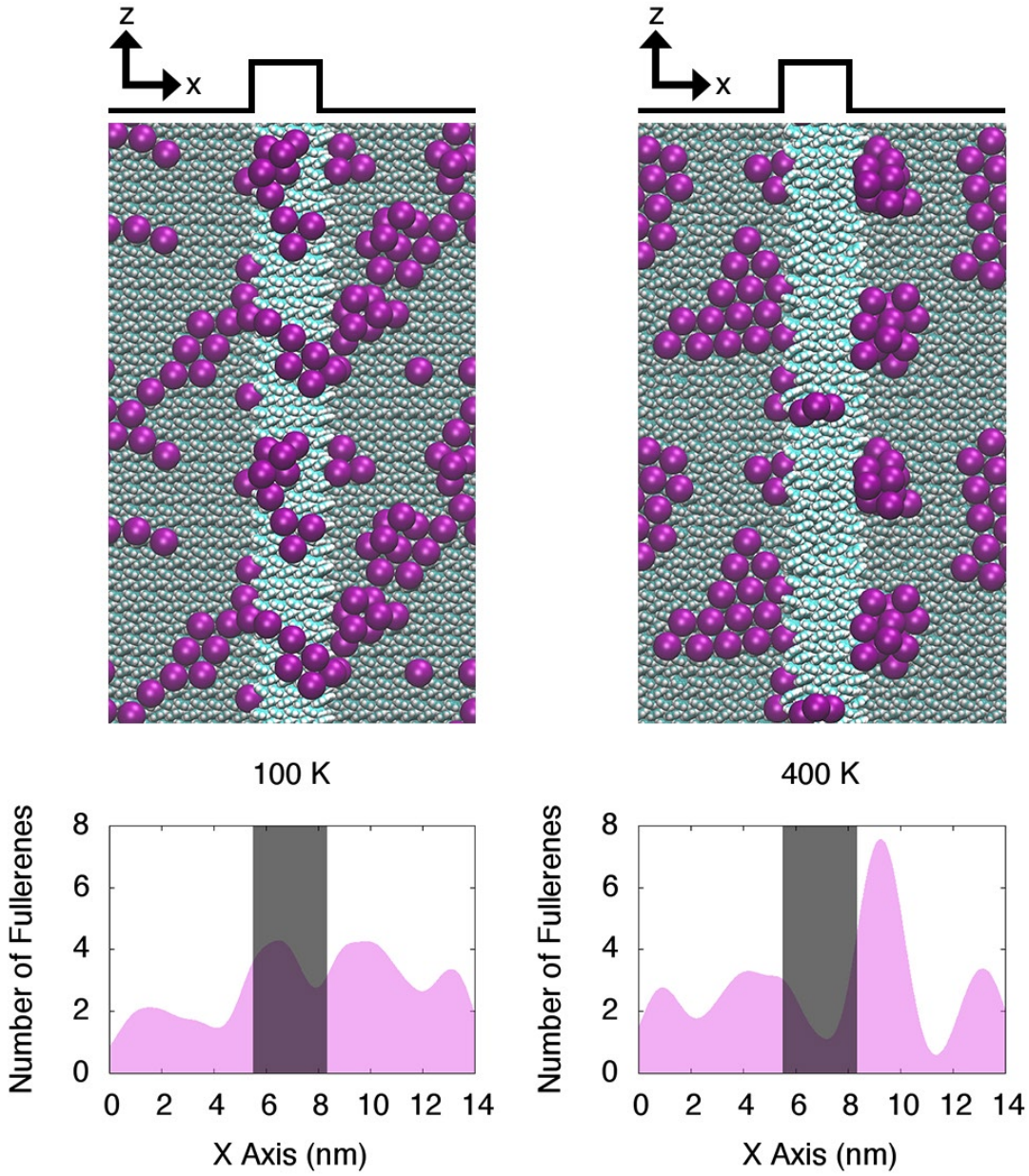

Figure 2.6: Clustering of C_{60} molecules on a pentacene step edge as a function of temperature; left 100 K, right, 400 K. Top row: CGMD snapshot of the end of a 0.4 ns simulation of 65 C_{60} molecules (purple) on a pentacene surface showing terraces (in black) and a central pentacene monolayer-high pentacene step (grey). Bottom row: Histogram of the location of C_{60} molecules across the width of the simulation box. Results for 100 K (left) show a relatively even distribution of C_{60} molecules on the surface with perhaps a small tendency for C_{60} to aggregate at the step edges (especially on the RHS of the wall). At 400 K (right), the tendency for C_{60} to aggregate on the RHS of the wall) is pronounced.

Unlike the KMC simulations, where we see that 3D C_{60} mounds occur stochastically on the surface, the CG MD results suggest that C_{60} will prefer to form mounds at step edges of the pentacene surface. This behavior is reasonable since we know (from all-atom simulations of a single C_{60} molecule[38]) that C_{60} has a strong binding energy with a kink site. In addition, C_{60} grain boundaries are unlikely to form along the pentacene wall since the attraction to the pentacene step edge is stronger than the lattice constraint imposed by the surface underneath.

2.4.5 Sub-Monolayer Growth: KMC Results

During sub-monolayer growth (<50% coverage), the growth mechanism is dominated by the nucleation and growth of C_{60} clusters on the pentacene surface. We focused on obtaining results for the "thin film" phase of pentacene due to its known higher surface diffusion rate compared to bulk phase pentacene.[26] Snapshots for the thin film phase pentacene simulation are shown in Figure 2.7 The different colors in Figure 2.7 do not represent unique clusters, but instead reflect whether the molecule is positioned on the A, B, or C lattice, designations for the three possible hexagonal lattices.[1] Regions of neighboring C_{60} molecules labeled with a different lattice color represent the initial formation of grain boundaries.

The final thin film phase snapshot was recorded after 390 ns of simulation, corresponding to 60% surface coverage. The appearance of growth beyond the 1st monolayer is already apparent. These results are fully consistent with earlier results by Cantrell *et al.*[1]

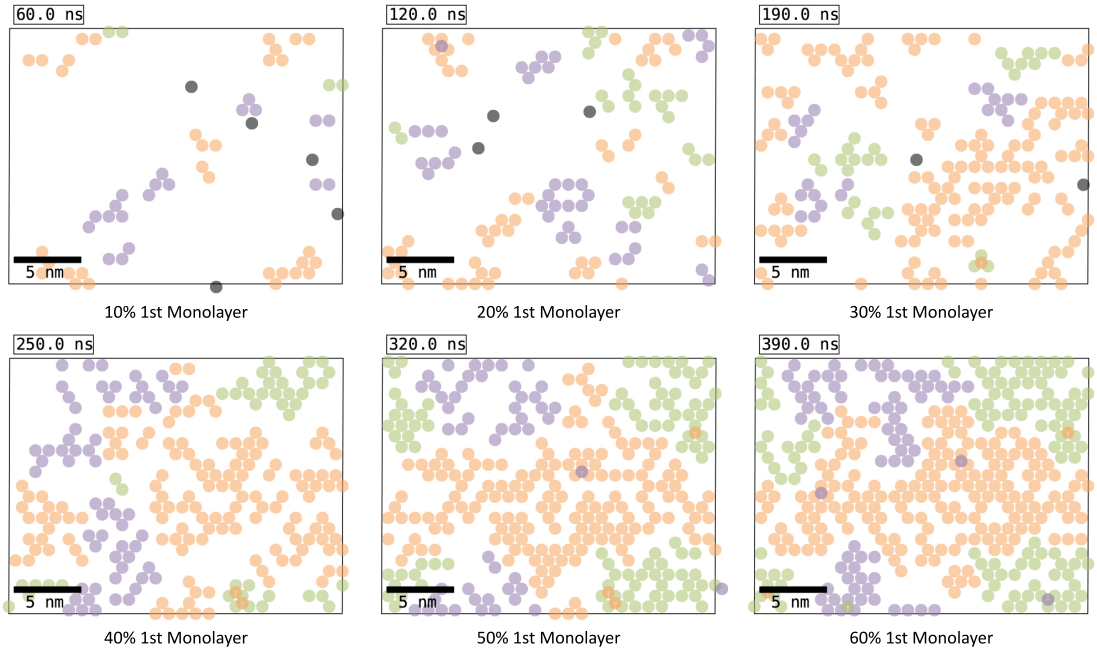

Figure 2.7: KMC-derived snapshots representing low coverage (10-60% of a monolayer) at 300 K. Corresponding times are given in the top LH corner of each snapshot. Molecules are colored in terms of their location: molecules are either on the QP lattice (dark gray) or on the Hex lattice as part of the A (green), B (orange), or C (purple) lattice[1]. Deeper colored Hex atoms represent the appearance of atoms on a second layer. Whether these atoms stay on the higher level or jump down to a lower layer will be resolved as the simulation proceeds.

2.5 Results for Multilayer growth

2.5.1 Understanding Multilayer Growth using Surface Roughness

During multilayer growth, the growth mechanism is characterized by the growth and coalescence of grains. The growth mode is determined by the balance between intermolecular forces (C_{60}-C_{60}) and film-substrate forces (C_{60}-pentacene).

Surface roughness was used as a measure of thin film cohesion and morphology. The Roughness Average (Ra), the typical reported value of surface roughness, measures the average deviation from the mean across a surface. For a 2D surface, the Roughness Average is

$$Ra = \frac{1}{A} \iint_A |Z(x, y)| dxdy \tag{2.1}$$

where $|Z(x)|$ is the deviation from the mean height and A is the surface area sampled. At each simulation time point, the 3D deposition was rasterized into a 2D height-map using a 2 Å probe with a resolution of 1 pixel/Å. The mean height and the deviation from the mean height were calculated from the resulting 2D surface.

2.5.2 Multilayer Growth: KMC Results

In this case, the heteroepitactical growth of C_{60} on pentacene introduces a strained film-substrate force and promotes dewetting, characteristic of Volmer-Weber (island) growth. The substrate temperature provides a way to tune the energy avail-

able to dewet and form islands. Counter-intuitively, we shall show that, due to this strain energy, *reducing* the temperature allows a somewhat *smoother* thin film to be created for C_{60} growth on pentacene. At sufficiently high temperatures, we can also draw a distinction between the growth habits of C_{60} on pentacene and C_{60} on itself: At high temperatures, we observe that C_{60} on C_{60} prefers layer-by-layer growth, whereas C_{60} on pentacene promotes dewetting at high temperature. This high temperature behavior follows Stranski-Krastanov growth, with an initial layer deposition followed by island formation.

To investigate this, we began by evaluating the growth mechanism of C_{60} on C_{60}. In comparison to our subsequent simulations of C_{60} on pentacene, this will allow us to differentiate growth characteristics that result from pentacene-induced strain. KMC simulations of C_{60} growth on C_{60} were run for 2.7 μs at six different temperatures that cover the range of experimental studies and stay below the melting point: 150 - 400 K in 50 K increments.

As shown in Figure 2.8, the surface roughness at higher temperatures (350 K and 400 K) is oscillatory. This pattern is typical of layer-by-layer growth: As a new layer is grown, the roughness increases until the monolayer completes, at which point the roughness decreases to its lowest level. In contrast, at lower temperatures (150-300 K), the growth is more irregular, with distinct islands growing on top of incomplete monolayers. This is especially clear at 150 K where the roughness grows at a higher pace than the higher temperature simulations. Overall, the growth of C_{60} on C_{60} follows expected behavior, where high temperature promotes layer-by-layer (Frank-van der Merwe) growth, whereas low temperature promotes 3D island formation and Vollmer-Weber growth.

The high temperature KMC simulations qualitatively match the results for

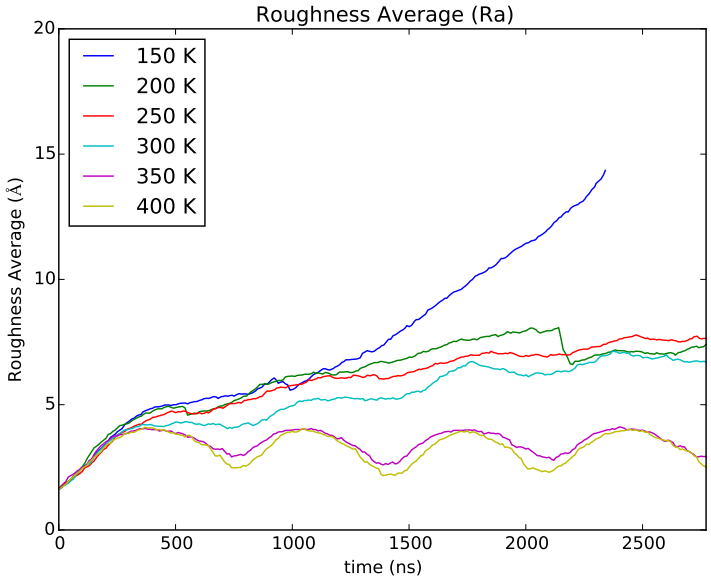

Figure 2.8: Roughness Average obtained from KMC simulations of C_{60} on C_{60} as a function of temperature from 150 K (blue) to 400 K (yellow). Color code given in the inset. The oscillatory roughness of the higher temperature simulations reflects Frank-Van der Merwe (layer-by-layer) growth, whereas the continuously increasing roughness of the lower temperature simulations is a product of island growth.

C_{60} on C_{60} that were predicted by Bommel et al..[39] They calculated just three energy barriers that they posit were sufficient to capture experimentally observed behavior in KMC simulations at high temperatures (313 K, 333 K, 353 K). Their results are similar to Figure 2.9(b) where the deposition follows Frank-Van der Merwe (layer-by-layer) growth. However, the KMC code presented in this paper is also capable of running simulations at lower temperatures, where the growth mode instead follows island growth, as shown in Figure 2.9(a). At 150 K, the 2nd monolayer reaches 10% coverage when the 1st monolayer is 53% covered while the 3rd monolayer reaches 10% coverage when the 1st monolayer is 81% covered. Bommel *et al.* did not investigate what would happen to the growth morphology at lower temperatures using their interesting 3-barrier approach. We speculate that three barriers would not be sufficient to capture the island growth mode, but it would be an interesting study.

Unlike the growth of C_{60} on C_{60}, we found that heteroepitactical growth of C_{60} on pentacene introduces strain into the film-substrate forces and promotes dewetting. In addition, if pentacene terraces are present, as they will under experimental conditions[24], they will influence both the nucleation sites and the mode of multilayer growth. To show this, KMC simulations of C_{60} growth on pentacene were run for 2.7 μs at six different temperatures: 150 K - 400 K in increments of 50 K. As mentioned above, to approximate the effect of a pentacene terrace, a fixed, three-layer high C_{60} island (in lieu of a monolayer step of pentacene) was placed in the center of the simulation box consisting initially of a flat terrace. Similar to a pentacene terrace, this island promotes the aggregation of C_{60} molecules around the edge. Figure 2.10 shows the surface roughness of C_{60} thin film growth on pentacene as a function of time.

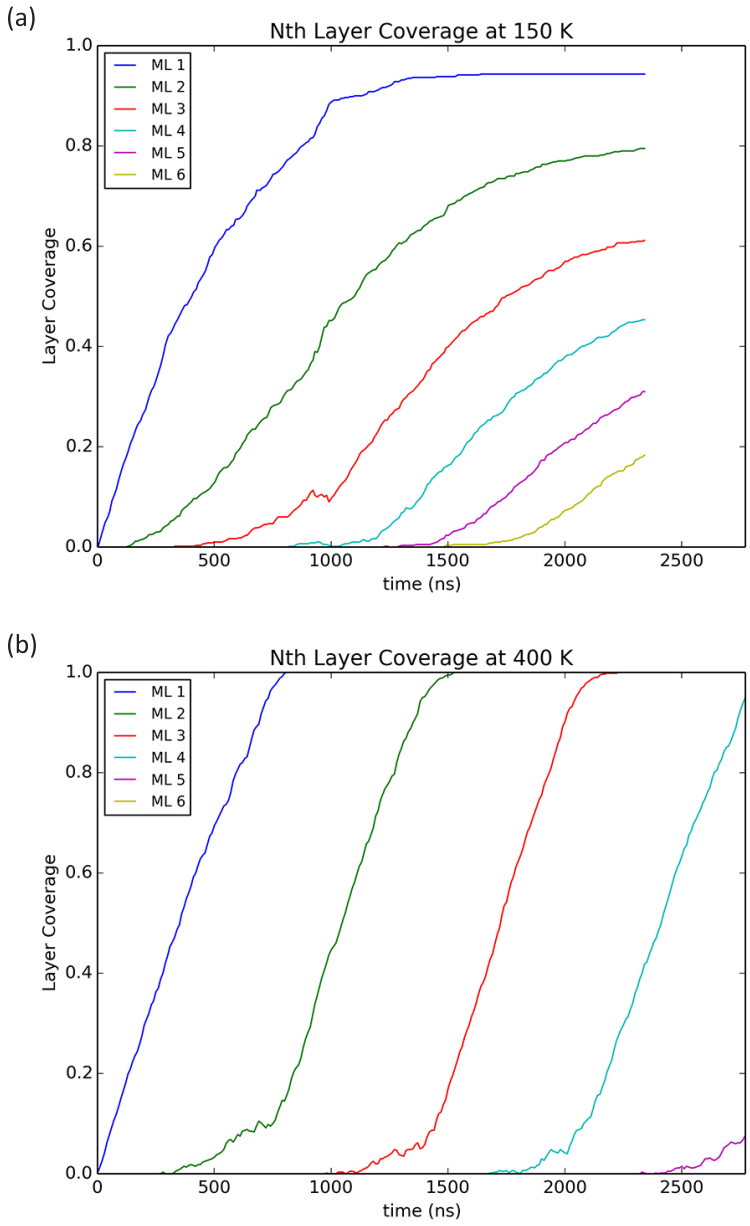

Figure 2.9: Nth-monolayer coverage of C_{60} on C_{60} as a function of simulated time at (a) 150 K and (b) 400 K showing the timing of the appearance of subsequent monolayers as growth proceeds. Each monolayer (ML) is shown by a different color, annotated in the inset. Low temperature simulations follow Vollmer-Weber 3D growth, whereas higher temperature simulations show Frank-Van der Merwe (layer-by-layer) growth.

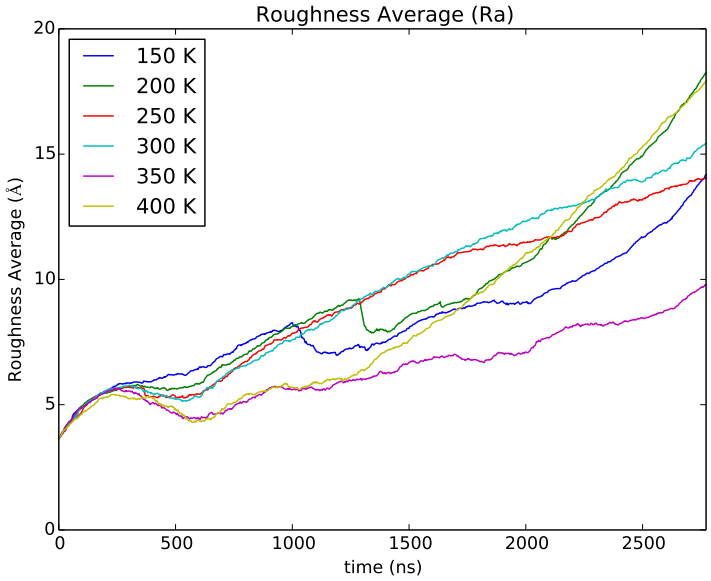

Figure 2.10: Roughness Average from KMC Simulations of C_{60} on pentacene as a function of temperature from 150 K (blue) to 400 K (yellow). Color code given in the inset. The early time behavior of the higher temperature simulations shows one clear oscillatory peak, followed by 3D growth as time proceeds. This is characteristic of Stranski-Krastenov growth (layer-by-layer followed by 3D island growth).

As for our earlier study of C_{60} deposition on C_{60}, the higher temperature simulations of C_{60} on pentacene (350 K to 400 K) in Figure 2.10 show a lower roughness as the early layers fill to completion more systematically than the lower temperature simulations. The 150 K and 200 K simulations show a delayed dip in roughness around 1.2 μs that corresponds to the first monolayer completely filling and the second monolayer partially filling. All the simulations show a continuous increase in roughness after around 1.5 μs. Breuer and Witte[24] showed similar results in that their larger-scale deposition experiments (5 nm) showed significant roughness at all temperatures. However, Breuer and Witte's results (not shown in Figure 2.10) showed larger peaks and deeper wells at higher temperatures, which are not clearly shown in the KMC simulations. Like the simulation results, experiments predict that lower temperature results will produce a lower roughness, on average, than those at higher temperatures.

The higher temperature experiments by Breuer and Witte[24] show a large grain size ($\sim$60 nm), which is impossible to reflect accurately in the KMC simulations since the KMC box size is only 24.9 nm by 20.8 nm. This could be a possible source of the difference between the finer details of the experimental results and the simulations. Capturing this high temperature behavior would require a box at least three times as large in both $x-$ and $y-$ directions, and an even larger simulation box to observe multiple grains. It would also require the deposition of at least nine times as many C_{60} molecules in order to reach similar monolayer coverage. This scale of simulation is beyond our reach and the reproduction of grain size is, in any case, not a focus here.

The low temperature, 150 K, KMC simulations for C_{60} on pentacene in Figure 2.11 show 3D growth similar to what we observed for C_{60} on C_{60} deposition. At

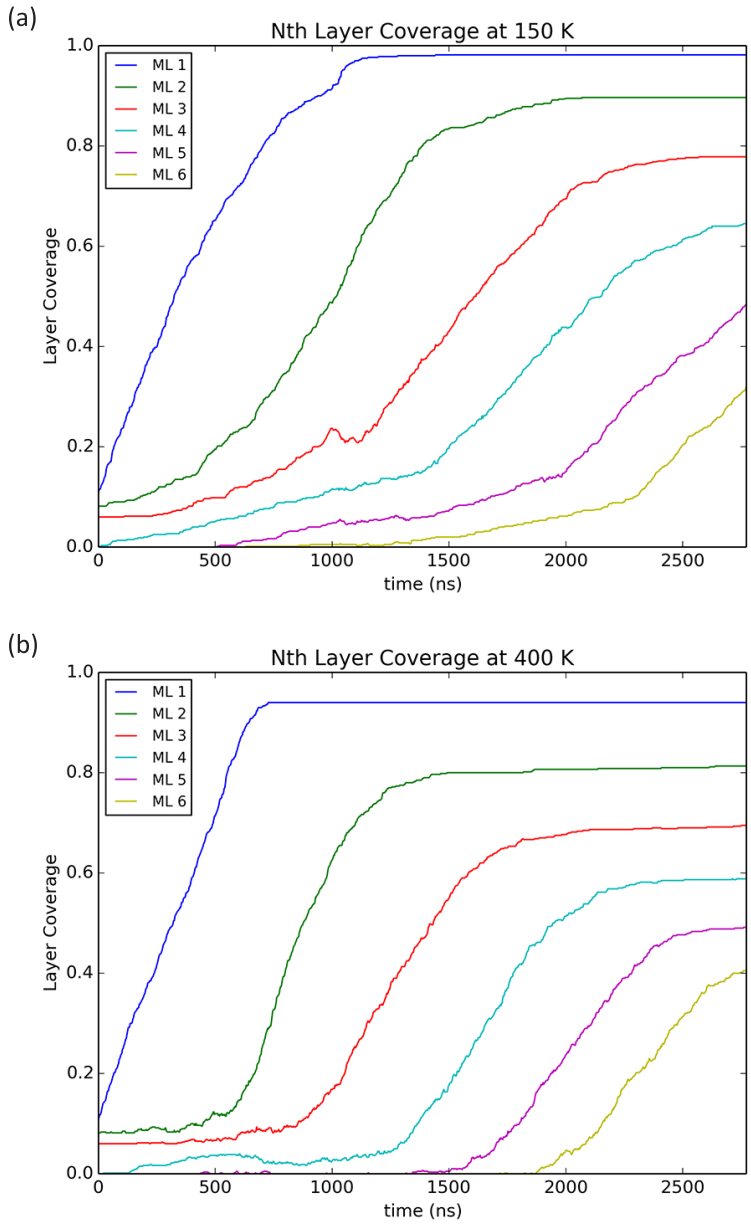

Figure 2.11: Nth-monolayer coverage of C_{60} on pentacene as a function of simulated time at (a) 150 K and (b) 400 K as predicted by KMC. A fixed island of C_{60} molecules is present in the center of the simulation box to replicate a pentacene terrace and contains C_{60} molecules up to three layers high. These fixed molecules are counted as part of the initial condition at t = 0 ns for normalization purposes. This figure shows the timing of the appearance of subsequent monolayers as growth proceeds. Each monolayer (ML) is shown as a different color, annotated in the inset. Early coverage (first 1-2 MLs) during the high temperature simulations show Frank-Van der Merwe (layer-by-layer) growth, but the film transitions to 3D growth with decreasing overall coverage per layer. Lower temperature simulations exclusively show island growth. The progressively lower maximum coverage values result from a decrease of allowable lattice sites.

high temperature, 400 K, Figure 2.11 shows that the first layer completes before the second begins, but that subsequent layers start to grow well before the preceding one completes. This behavior is different from our observations of C_{60} on C_{60} growth and suggests that the grain boundaries in the first monolayer, induced by strain with the underlying lattice, constrain layer-by-layer growth. The coalescence of grain boundaries, not possible with this code, might allow a single crystalline first monolayer to form. Or it might not, but resolving this is not possible with a lattice-based KMC approach. The lower values for the maximum coverage exhibited in subsequent monolayers result from a decrease of available lattice sites (a corollary to the grain boundary issue).

These simulations of C_{60} growth on pentacene reveal a limitation of KMC codes: Our KMC code, like all lattice-based KMC codes, is designed to operate on the basis of transitions among well-defined lattice sites. However, strained systems, such as C_{60} on pentacene, tend -in practice- to generate defects in order to reduce tension. While the KMC algorithm presented could be updated to include energy barriers to and from defect sites, this is a large undertaking and there is a high risk of not including an important mechanism. The additional effort might not reveal more than the level of intuition of the code developer. The lack of off-lattice sites has several important effects. First, C_{60} molecules cannot be deposited in grain boundaries. In addition, C_{60} molecules cannot cross grain boundaries, which will artificially enhance island growth. Another artifact of this KMC limitation is that the maximum coverage at higher monolayers is limited by the formation and size of grains. The cumulative effect in this system is that the accuracy and reliability of the KMC simulations tends to decrease as the simulation time increases.

2.5.3 Multilayer Growth: CGMD Results

Experimental results from multilayer depositions predict that lower temperature depositions of C_{60} on pentacene will produce a smoother thin film topology[24]. This is counter-intuitive and is not borne out by the KMC simulations. In contrast, CGMD simulations allow C_{60} molecules to move freely across terraces, grain boundaries and step edges. These simulations allow us to probe the accuracy of the KMC simulations and test whether the assumptions made by the KMC are sufficient to capture experimentally observed growth mechanisms.

The CGMD method was used to simulate the "annealing" of the surface starting from the final multilayer C_{60} snapshots predicted by KMC. The CGMD simulations were run for 0.5 ns at the temperatures at which the KMC simulations were run (150-400 K, in increments of 50 K). Even within this short time scale (0.5 ns), the CGMD simulations showed the coalescence of smaller grains with larger grains, which would not have been possible with the KMC code. However, the islands themselves did not reshape themselves in any way, which suggests that the crystal structure introduced during deposition has already been defined by short time scales.

Multilayer CGMD simulations were then performed as described in Section 2.2.2, but run until 390 molecules of C_{60} molecules have been deposited, enough to form three monolayers. The final snapshots of the 100 K and 500 K depositions are shown in Figure 2.12. As an FCC crystal, the distance between C_{60} layers on the vertical axis is equal to $sphere\ diameter * \sqrt{(}3)/6$. We take advantage of this property to assign each C_{60} molecule to the closest theoretical monolayer and label it appropriately in Figure 2.12.

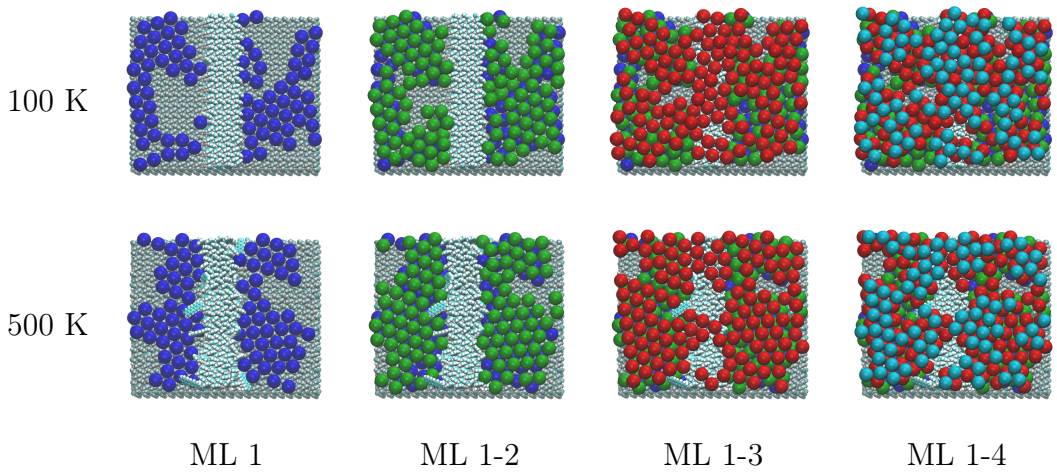

Figure 2.12: Final snapshots of 2 ns CGMD simulations of 3 nm C_{60} deposition on pentacene at 100 K and 500 K. Each monolayer has been labeled with a different color to highlight the morphology of each layer. Both simulations show significant crystallinity as the C_{60} molecules tend to form ordered FCC sheets, especially in monolayers 1 and 2. The first monolayer does not fill in either the low temperature or high temperature case, which is caused by the occlusion of the surface by the higher monolayers and the propensity for the C_{60} molecules to dewet the pentacene surface. Monolayers 3 and 4 show significant disorder and off-lattice behavior, especially in the 100 K simulation.

The CGMD simulations in Figure 2.12 show a high degree of crystallinity and island coalescence, especially in monolayers 1 and 2. Even at long time scales, the first monolayer does not fill in either the 100 K or 500 K depositions, which is caused by the occlusion of the surface by the higher monolayers and the propensity for C_{60} molecules to dewet from the pentacene surface. This dominance of the C_{60} - C_{60} interactions has been seen by us and others in MD simulations in which surface C_{60} molecules push pentacene molecules in the substrate out of their way.[40] As predicted by Figure 2.6, the C_{60} molecules tend to aggregate toward the pentacene step edge during the higher temperature 500 K simulation. Higher monolayers show significant disorder and off-lattice behavior, especially in the 100 K simulation. The cumulative effect of these observations on long-term film growth can be seen in the surface roughness calculations, shown in Figure 2.13.

The extent of surface roughness and layer-by-layer growth predicted by the CGMD diverges from the KMC results. The surface roughness for all the simulations initially increases as the smooth pentacene surface is perturbed by C_{60} molecules. Results at different temperatures begin to diverge after around 500 ps. The lowest temperature simulation (100 K) hovers around a 7.5 Å roughness average, while the highest temperature simulation (600 K) peaks at about 10 Å roughness, on average, after $\sim$1000 ps. These two simulations form an upper and lower bound for the early surface roughness. The intermediate temperatures fall between these two extremes and show no clear correlation. This suggests that there is a significant standard deviation between simulation results of the same temperature.

All other variables being constant, we believe that a higher temperature promotes the ability of C_{60} molecules to climb up an adjacent step edge, thereby

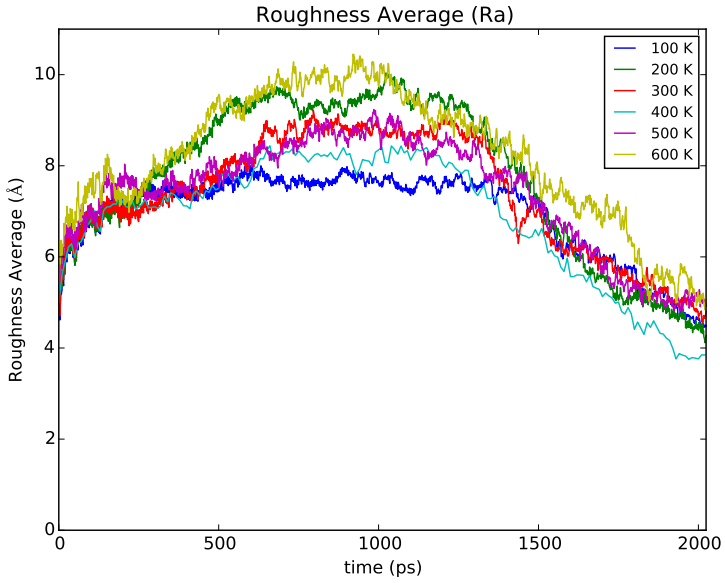

Figure 2.13: Roughness Average from KMC simulations of C_{60} on pentacene as a function of temperature from 100 K (blue) to 600 K (yellow). Color code given in the inset. The 100 K and 600 K simulations show lower and upper bounds, respectively, for surface roughness during early thin film growth.

increasing the surface roughness. All the simulations decrease in roughness starting at around 1250 ps and falling below the initial value of the surface roughness to about 4 Å. In contrast to the KMC results in Figure 2.11, the surface roughness does not continue to increase as time proceeds after the first few monolayers complete. The CGMD simulations are not limited to lattice sites and can form complete monolayers beyond the first one, despite a small distribution of molecule heights within a layer. This promotes the smoothness seen at the end of the CGMD simulation, in contrast to the KMC.

Figure 2.14 shows that the growth mode of both the low temperature and the high temperature simulations is dominated by 3D island growth. The lattice strain introduced by the C_{60}/pentacene lattice mismatch is almost certainly responsible. At low temperatures, upward jumps of C_{60} to promote immediate 3D growth is hindered by the lack of energy to overcome the Schwoebel barrier. This, non-intuitively, promotes a smoother surface during the growth of the first few monolayers. However, stochastic deposition means that roughness is still introduced. 3D growth is more pronounced in the high temperature simulation where enough energy is present in the system to overcome kinetic barriers and upward jumps are easier. CGMD simulations show that empty lattice sites and defects frequently occur in the 1st monolayer, since off-lattice positions are stabilized when there are at least three neighbors. Some of these defects are probably an artifact of the fast deposition times that have to be employed in MD simulations. Once the 1st monolayer is complete, simulations at all temperatures reach the same surface roughness, which shows that the C_{60} - C_{60} interaction now dominates and the pentacene surface no longer influences the crystal structure. The effect of the appearance of, perhaps spurious, early defects is reduced as the distance away from the substrate increases.

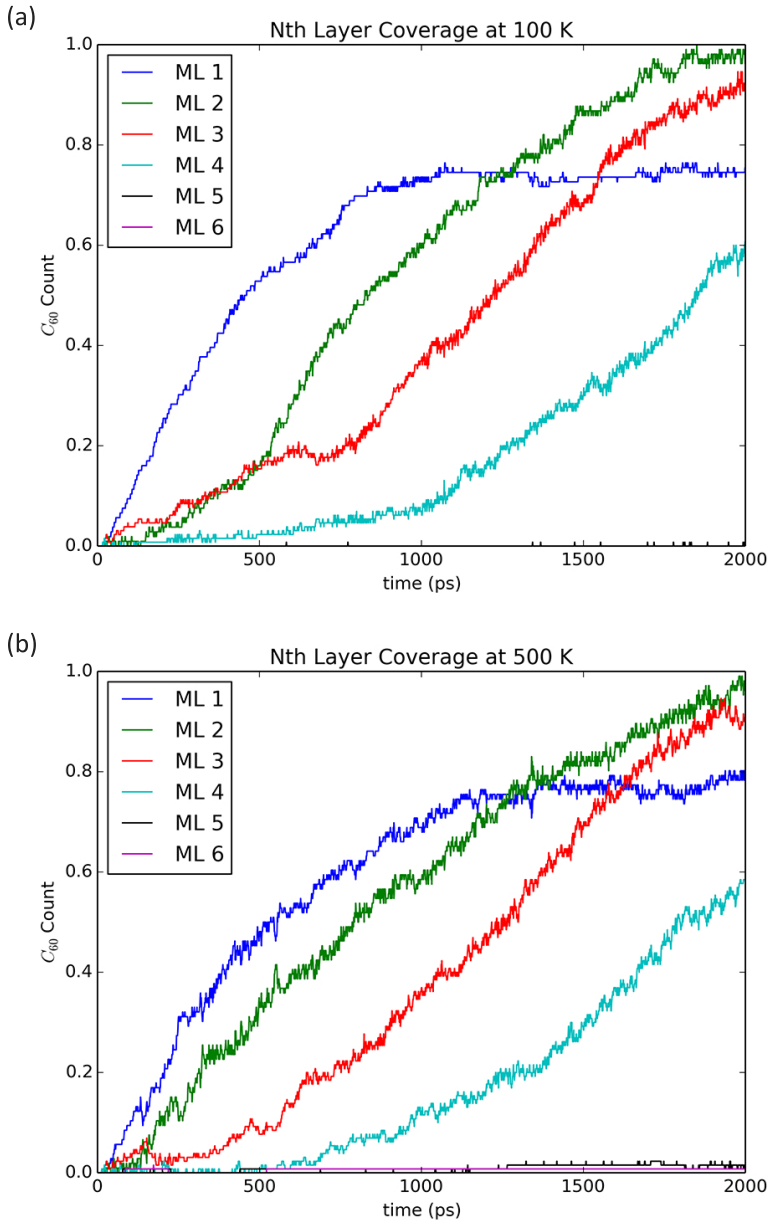

Figure 2.14: Nth-monolayer coverage of C_{60} on pentacene as a function of simulated time at (a) 100 K and (b) 500 K as predicted by CGMD. Key as in Figure 2.11. Each monolayer is normalized by the accessible surface area: ML 1 and 2 can access 82% of the surface (excludes the pentacene step), whereas ML 3-6 can access the entire surface. In contrast to the KMC simulations, the high temperature (500 K) simulation shows immediate 3D growth, with the 2nd layer growing almost as quickly as the 1st layer. The low temperature (100 K) simulation shows delayed growth of the 2nd layer until the first ML is perhaps 40-50 per cent complete. Subsequent growth remains 3D.

2.6 Conclusions

Our goals for this work were to understand how best to simulate heteroepitactical growth and test our predictions of such growth against relatively recent experimental results for sub-monolayer growth. As validation, our new 2nd-generation KMC model reproduced the sub-monolayer results of a previous KMC study[1]. Comparison of KMC and a new 2D reaction-diffusion continuum model allowed us to test the ability of a much faster, simpler, model to capture the nuances of the sub-monolayer growth process. The comparison shows generally excellent confirmation of results between the two approaches, especially at longer time frames, as we might expect. This comparison also allowed us to show that the thin film phase of pentacene will be a more effective surface for producing larger (and more ordered) C_{60} grains than the bulk phase of pentacene. This is intuitively reasonable due to the larger C_{60} diffusion coefficient on the thin film pentacene surface compared to that on the bulk phase, which will promote grains merging and reordering.

Our 2nd-generation epitactical KMC code allowed us to simulate the growth of more than six layers of C_{60}. When applied to high temperature C_{60} on C_{60} growth, the KMC simulations show layer-by-layer growth similar to the 3-barrier KMC study by Bommel et al.[39]. Our model is robust enough to also simulate low temperature simulations where the island growth mode is expressed. The surface roughness demonstrates that the formation of polycrystalline-like grains, a result of the on-lattice constraints of the method, has long-term implications for the morphology of the C_{60} thin film.

The CGMD model expanded our knowledge of sub-monolayer growth by relaxing the on-lattice constraint and introducing an explicit pentacene terrace. The lattice mismatch causes C_{60} aggregation and the generation of defects. This ag-

gregation is particularly pronounced at high temperatures where C_{60} clusters form along pentacene terraces. This mirrors experimental results of Breuer and Witte[24]. The growth of irregularly sized grains will be difficult to overcome without improved deposition techniques that can circumvent the 3D mound-like growth at low temperatures and the C_{60} aggregation into clusters along pentacene terraces at higher temperatures.

Differences became apparent as we compared KMC to CGMD simulations over a range of temperatures suggested by experiments. While higher temperature KMC simulations suggest Stranski-Krastenov growth (layer(s) followed by islands), corresponding CGMD simulations showed that C_{60} deposition at a step edge corresponding to a 1-monolayer high pentacene terrace will yield C_{60} aggregates preferentially along the pentacene step edge. Since pentacene terraces form naturally under experimental conditions, this implies that single crystalline C_{60} thin films may be impossible at high temperatures unless the formation of pentacene terraces can be regulated. Instead, CGMD simulations suggest that the kinetic trapping present at low temperatures will promote smooth but disordered thin film growth. These CGMD results reproduce multilayer deposition experiments by Breuer and Witte[24], which show the unexpected result that high temperature deposition produces a *rougher* surface compared to that at lower temperatures. We attribute this to the increased viability of C_{60} molecules to overcome the Schwoebel barrier at higher temperatures and thus climbing up an adjacent step edge. Our CGMD results thus confirm that the roughness of the growth can be influenced by higher temperatures and suggest that the interface morphology will be disordered.

A summary of the growth modes presented in this chapter, in comparison to classic homoepitactic growth (such as C_{60} on C_{60}) and experimental results[24] is

Table 2.3: Growth Mode

Model	Low Temperature	High Temperature
Homoepitactic Growth	Island[b]	Layer-by-Layer[d]
Kinetic Monte Carlo	Island[b]	Layer plus Island[c]
Coarse-Grained Molecular Dynamics	Island[b]	Island[b]
Experimental Results[a]	Island[b]	Island[b]

[a] Breuer and Witte [24]; [b] Volmer-Weber; [c] Stranski-Krastanov; [d] Frank-Van der Merwe.

shown in Table 1.

While a higher temperature usually promotes the production of a more single crystal-like thin film, as we showed for the layer-by-layer growth of C_{60} on C_{60}, the strain caused by the lattice mismatch between the C_{60} and the pentacene causes 3D growth. The impact of clustering on electronic device performance has been explored by Conrad *et al.*[23]. They write that clustering of C_{60} potentially improves charge separation at the cost of a slightly reduced maximum open circuit voltage due to a lessening by ∼0.2 eV of the pentacene HOMO to C_{60} LUMO. In contrast, low temperature growth is polycrystalline and will introduce defects into the lattice. This disordered C_{60} thin film will negatively impact electron transport[41]. Overall, we recommend that future computational studies of heteroepitactic and strained growth use CGMD, which, given a sufficiently accurate coarse-grained potential, appears to accurately simulate the defects promoted in these systems.

CHAPTER 3

MOLECULAR MORPHOLOGY OF SEQUENCE-DEFINED OLIGOTEAS

3.1 Introduction

3.1.1 Background on OligoTEAs

Sequence-defined polymers are macromolecules with precisely controlled monomer configuration. The importance of sequence control has been demonstrated in biological systems, such as nucleic acids and peptides, as a method to manipulate structural, physical, and chemical properties.[42] Common synthetic polymers are usually homopolymers, made of the same monomer unit, or copolymers with simple chain microstructures, such as random or block copolymers. In order to enhance the capabilities of synthetic polymers, researchers have been exploring ways to produce sequence-defined polymers to create new materials with engineered properties such as solubility, conductivity, molecular recognition, biocompatibility, and reactivity.[43] To this end, the Alabi group at Cornell has explored and developed the assembly of sequence-defined oligothioetheramides (oligoTEAs).[42]

In order to engineer useful sequence-defined polymers, fast and accurate methods of characterizing solution phase oligomer structure and dynamics are required. In this work, Molecular Dynamics (MD) simulations were used to rapidly discriminate between oligomer properties and predict properties of unsynthesized oligomer variants. In particular, molecular dynamics can probe the atomistic configuration and average conformational ensemble of the oligomers, properties that can only

be indirectly probed by experimental approaches. These computational methods served as a validation of the experimental methods used by the Alabi lab: variable temperature pulse field gradient (PFG) NMR and double electron-electron resonance (DEER).[2] This chapter will explore how the molecular dynamics methods were implemented and what can be learned from Molecular Dynamics simulations of oligoTEAs.

Fully atomistic Molecular Dynamics simulations have been used to characterize the relationship between structure and dynamic properties in solution-phase polymers. One advantage of this methodology is that individual polymers can be observed to understand how structure evolves over time. Atomistic simulations have been used to characterize various properties including elasticity,[44,45] conjugation,[46] shearing[47] and diffusion.[48,49,50]

Using Molecular Dynamics to characterize oligoTEAs will allow us to validate experimental results and enhance our understanding of their solution-phase dynamics. The first set of oligomers was synthesized by iterating dithiothreitol (DTT) dithiol and the protected sulfonate N-allyl acrylamide monomer. Experimental results for (DTT-Sulf)$_n$ suggested that there was significant collapse of the oligomer strand. In order to probe this behavior, Molecular Dynamics simulations were performed for oligomer chains of degree of polymerization 2-12 (*i.e.*, 2mer to 12mer) to calculate dynamic behavior as a function of molecular weight. To probe the effects of the different functional groups on the oligomer contraction, three alternative oligomers were simulated, which contained: (1) a noncharged methyl sulfone (MeS) pendant group, which removes electrostatic repulsion with minimal structural change, (2) a methylene backbone using butanedithiol (BDT), which removes backbone hydrogen bonding, and (3) a positively charged guanidine (G)

group. An outline of oligothioetheramide assembly and the monomers used are shown in Figure 3.1.

3.2 Computational techniques

3.2.1 Molecular Dynamics

The oligomer simulations were run in LAMMPS, Sandia's widely used Molecular Dynamics software package[32]. A single oligomer chain was simulated for 50 ns with 1 fs timesteps in a water-filled box with periodic boundary conditions to simulate the motion of disperse oligomers in aqueous solution. An isothermal, NVT, ensemble was implemented in the MD simulation using a Nosé-Hoover thermostat set to 300 K. The OPLS (Optimized Potential for Liquid Simulations) force field developed by Jorgensen[37] was used for the oligomers and is expected to well represent the system since OPLS parameters are optimized to fit experimental properties of liquids, particularly the density and heat of vaporization, in addition to fitting gas-phase torsional profiles. To supplement the core OPLS parameters, the sulfonate parameters were taken from research by Canongia Lopes and Padua, which studied ionic liquids[51,52]. Since ionic liquid properties are heavily derived from charge interactions, we expect this force field to appropriately handle charge contributions to the system's dynamics. Finally, the force field selected for the water solvent was the TIP4P model, which offers a good compromise between computational efficiency and charge accuracy.[53]

Accurately simulating an isolated oligomer required careful design of physical constraints and charge constraints. The periodic simulation box was constructed

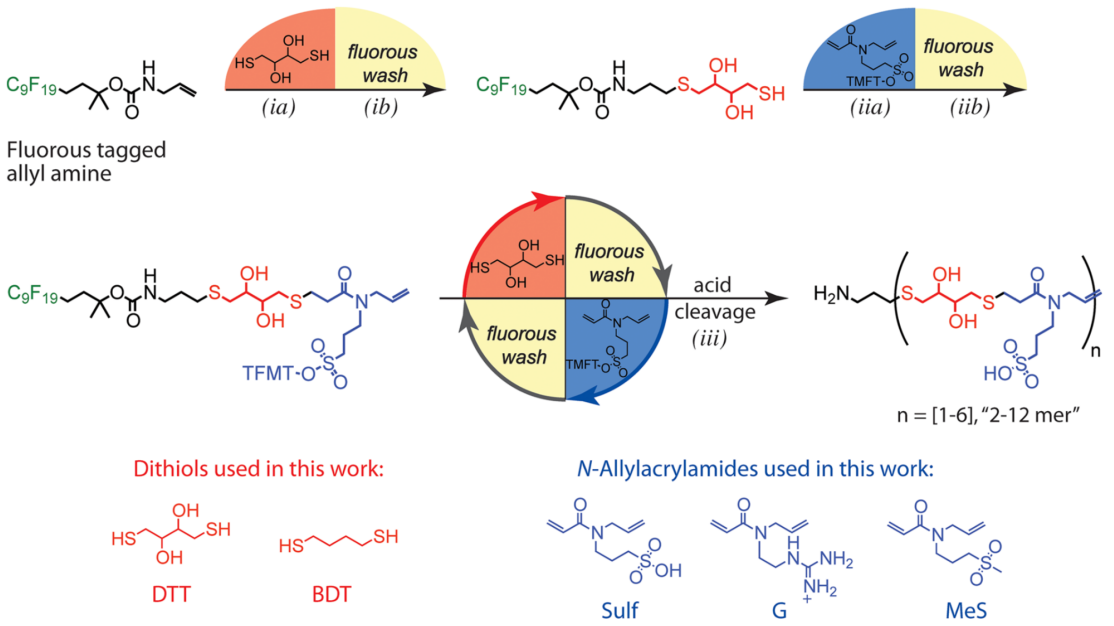

Figure 3.1: Oligothioetheramide assembly. (*ia*) A fluorous olefin is reacted with a dithiol in a UV-initiated thiolene and the product is purified (*ib*) by fluorous solid-phase extraction (FSPE). (*iia*) A fluorous thiol is reacted with an N-allyl acrylamide monomer in a phosphine-initiated thiol Michael addition and purified by FSPE (*iib*). These two reactions are repeated until the desired oligomer length is reached. (*iii*) The fluorous support is cleaved with trifluoroacetic acid and HPLC purified to give the final desired oligomer. TMFT = α-trifluoromethyltolyl protecting group. Reprinted with permission from [2]. Copyright 2017 American Chemical Society.

to be large enough to minimize any self-interaction errors. This was achieved by running a relatively long 10 ns simulation for each oligomer size to determine the approximate end-to-end distance distribution. We determined that less than 1% of the collected data were affected by self-interactions. The box sizes thus selected ranged from 3.7 nm for the shortest oligomers to 7 nm for the longest oligomers. The amount of water molecules required to fill those respective simulation boxes, ranged from 1700 molecules to 7200 molecules. The total amount of atoms simulated, including the oligomer, ranged from 5100 atoms to 22000 atoms.

The charge calculation was performed using a long-range particle-particle particle-mesh solver in LAMMPS. In solution, $(\text{DTT-Sulf})_{1-6}$ has a permanent negative charge on each sulfonate group, with proton counterions in solution. Conversely, $(\text{DTT-G})_{1-6}$ has a permanent positive charge on each guanidine group, with hydroxyl counterions. As an approximation, charge neutrality was achieved in the simulations by the inclusion of chloride ions, equivalent in quantity to the number of guanidine groups. Since experiments were performed in a salty solution, this was deemed an acceptable approximation.

3.3 Diffusion of OligoTEAs

3.3.1 End-to-End Distance

For the each oligomer type and size, 50 ns of Molecular Dynamics trajectory data were used to calculate an ensemble of end-to-end oligomer distances. Sample images of $(\text{DTT-Sulf})_{1-6}$ trajectory configurations are shown in Figure 3.2.

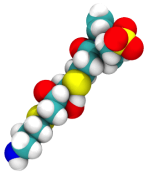

(a) $(\text{DTT-Sulf})_1$

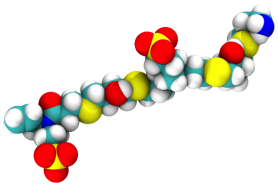

(b) $(\text{DTT-Sulf})_2$

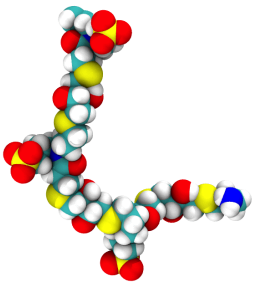

(c) $(\text{DTT-Sulf})_3$

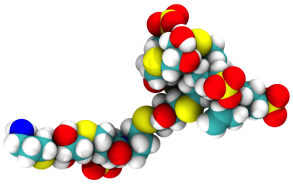

(d) $(\text{DTT-Sulf})_4$

(e) $(\text{DTT-Sulf})_5$

(f) $(\text{DTT-Sulf})_6$

Figure 3.2: Sample all-atom molecular dynamics images of DTT-Sulf (a) 1mer, (b) 2mer, (c) 3mer, (d) 4mer, (e), 5mer and (f) 6mer. H_2O molecules and hydrogen counterions omitted for clarity. These images illustrate how oligomers can have an elongated or collapsed state.

The aqueous diffusion simulations for $(\text{DTT-Sulf})_{1-6}$ (Figure 3.3) were validated against double electron electron resonance (DEER) EPR measurements of 100μM $(\text{DTT-Sulf})_{1-6}$ oligoTEAs in 20% ethylene glycol in water vitrified to 70 K from room temperature.[2] The values we calculated for the mean end-to-end distance of the oligomers calculated by MD were found to be in agreement with the EPR data, both of which showed an increase in end-to-end distance with increasing oligomer length. MD simulations observe a slightly greater end-to-end distance with the $(\text{DTT-Sulf})_{5,6}$, which falls within the experimentally observed conformational ensemble. Overall, these data highlight oligomer flexibility, given that we observed an average $\sim$50% collapse in length from their fully extended theoretical length (Figure 3.3B).

End-to-end distance measurements from MD (Figure 3.4) were used to visualize the individual contributions of backbone hydroxylation and pendant groups, revealing a large effect deriving from the nature of the oligoTEA backbone. We characterized oligomers with a methylene backbone, *i.e.*, $(\text{BDT-Sulf})_n$, positive charge $(\text{DTT-G})_n$, and neutral charge $(\text{DTT-MeS})_n$. All these oligomers appeared to experience some level of collapse. The reasons for the collapse could be entropic effects, hydrophobic collapse, or screening of intramolecular electrostatic repulsion. The MD data shows that both the cationic $(\text{DTT-G})_n$ and the methylene backbone of $(\text{BDT-Sulf})_n$ result in a relatively smaller end-to-end distance than we predicted for the $(\text{DTT-Sulf})_n$ and $(\text{DTT-MeS})_n$. This difference is highlighted by comparing the simulation and experimental results for the 10mers in Figure 3.5. The methylene backbone of $(\text{BDT-Sulf})_5$ results in a smaller end-to-end distance in both DEER and MD experiments. This effect could be rationalized by greater hydrophobic collapse without backbone hydroxylation. The hydroxylated backbone might be expected to participate in intramolecular interactions, aiding collapse by

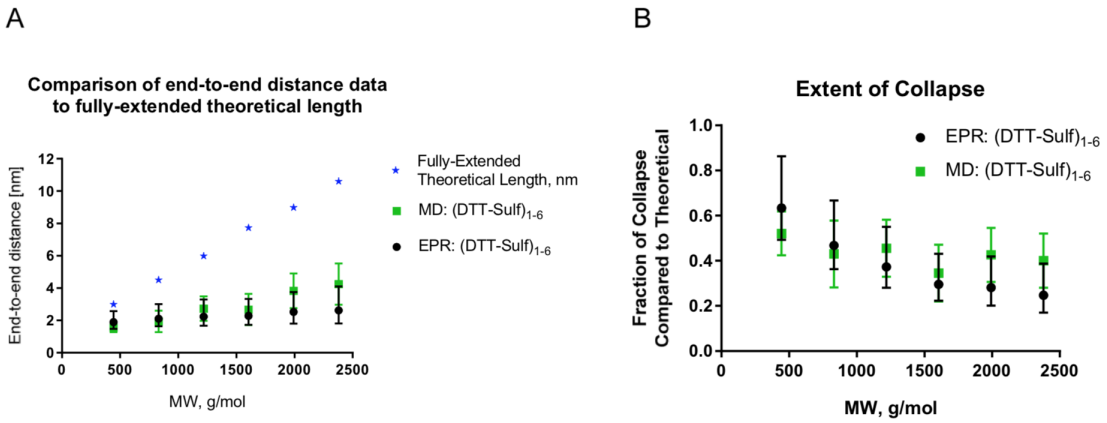

Figure 3.3: A. Comparison of end-to-end distances calculated from MD and experimental measurements. The fully-extended theoretical length for each oligomer is shown for reference. Experimental results come from DEER EPR measurements of 100uM $(DTT\text{-}Sulf)_{1-6}$ oligoTEAs in 20% ethylene glycol in water vitrified to 70K from room temperature. Error bars represent the standard deviation from the MD simulation after equilibration or the full-width at half-maximum (FWHM) from EPR. B. Calculation of the fraction of (DTT-Sulf)1-6 oligoTEA collapse.

attractive forces (*i.e.*, hydrogen bonding) to result in a smaller hydrodynamic size than the BDT-Sulf.

3.3.2 Aspect Ratio

The aspect ratio of a macromolecule quantifies the ratio of the longest molecular axis to the shortest molecular axis. We used this quantity as an alternative measure of oligomer shape during solution phase diffusion for the $(\text{DTT-Sulf})_n$ macromolecules. The shape of the molecule can be defined by the space occupied by its constituent atoms. Experimental methods of calculating the aspect ratio cannot discriminate to the level of atoms and instead relate diffusion to shape models using the Stokes-Einstein-Sutherland (SES) model.[54,55] In order to find a discrete shape model using Molecular Dynamics results, the set of oligomer atoms at each timestep was decomposed into a representation of the shape of the molecule in terms of the minimum volume-enclosing ellipsoid (MVEE). The resulting ellipsoid takes the form:

$$\frac{x^2}{a^2} + \frac{y^2}{b^2} + \frac{z^2}{c^2} = 1 \tag{3.1}$$

where a, b, c are the lengths of each ellipsoid axis. A visual representation of an ellipsoid is shown in Figure 3.6. This geometric form is convenient because the calculated axes can be used to solve the SES rod model.[56–59] The length of the rod corresponds to the longest ellipsoid axis, while the width of the rod can be estimated by averaging the shorter two axes. The simulated aspect ratio distribution for $(\text{DTT-Sulf})_n$ is compared to experimental results using the SES model in Figure 3.7.

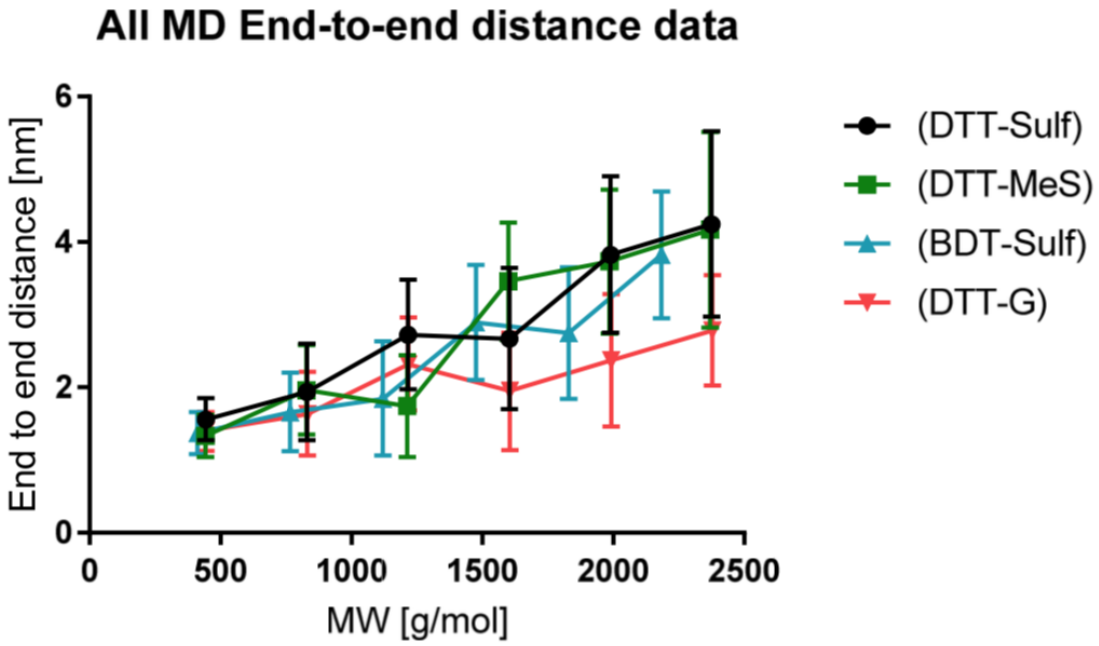

Figure 3.4: End-to-end distance measurements produced by single-chain Molecular Dynamics (MD) simulations at 300 K in an explicitly modeled water solvent versus the molecular weight of the oligoTEA. Error bars represent a standard deviation of the end-to-end distance. All the oligoTEAs tested showed an expected increase in end-to-end distance with increasing molecular weight.

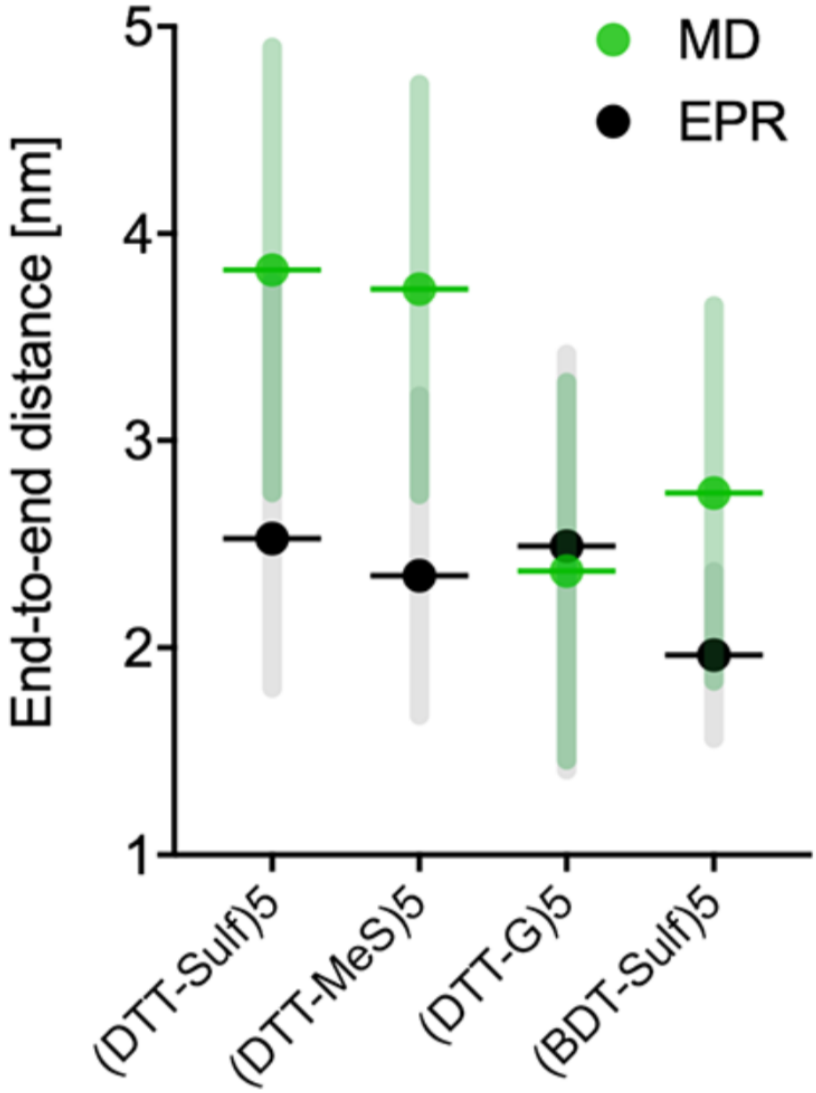

Figure 3.5: Mean end-to-end distance from DEER distance reconstruction and single-chain Molecular Dynamics simulation (300 K, explicit model for the water solvent). Data points represent the mean end-to-end distance. Error bars represent the full-width at half-maximum (EPR) or standard deviation (MD). EPR and MD results show roughly the same trend with change in oligoTEA character, though the MD results are generally higher by up to 1 nm, due to the experimental use of spin-labeled additives which add to their apparent length.

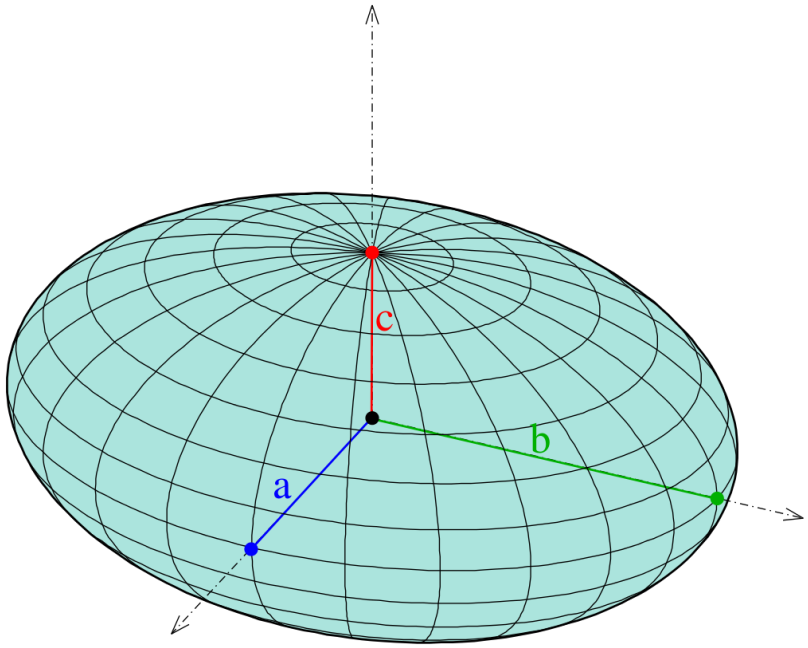

Figure 3.6: Visual representation of an ellipsoid. In this example, axis b is the longest direction, and the width of the rod would be estimated by averaging axes a and c.[3]

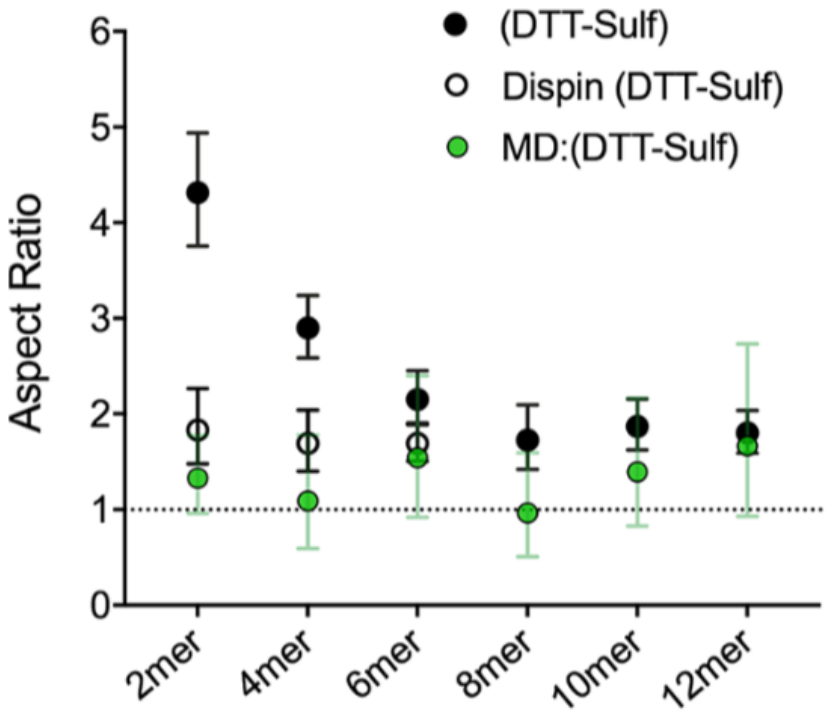

Figure 3.7: Aspect ratio of the $(\text{DTT-Sulf})_{1-6}$ series calculated from the solution to the SES rod model assuming the end-to-end distance data describes the long dimension (length) of the rod. Data in the filled green circles represent solutions to the SES rod model using the end-to-end distance data obtained from MD simulations. Data in the black filled circles were computed using end-to-end distance measurements from EPR and the diffusion coefficient of oligomers without the spin probes present. The open circles represent the aspect ratio of the $(\text{DTT-Sulf})_{1-6}$ oligomers computed using the diffusion coefficient of the oligomers bearing the two spin probes. The error bars on the experimental $(\text{DTT-Sulf})_{1-6}$ data series represent errors from the PFG NMR data and a 95% confidence level in the DEER data, all propagated through the SES model.

In a similar manner to the end-to-end distance data, our analysis of the aspect ratio data suggests a macromolecule with a flexible, spherical shape, especially at longer oligomer lengths. The original experimental data deviated from MD results by suggesting a longer macromolecule shape at shorter longer oligomer lengths. One strong possibility to explain this observation is that the addition of spin-labels required for experimental DEER measurements adds significant size (length) to the smaller oligomers. To investigate this theory, the first three di-spin-labeled oligomers ((DTT-Sulf)$_{1-3}$) were oxidized, measured by PFG NMR and reanalyzed with the SES rod model. The new aspect ratio which takes into account the spin labels on (DTT-Sulf)$_{1-3}$ confirms that the original aspect ratio of the smaller oligomers was inflated by the length added by the spin labels. With this analysis, Molecular Dynamics results were able to highlight a flaw in the assumptions present in the experimental set-up and enhance our understanding of oligomer conformation.

3.3.3 Diffusion Coefficient

The translational diffusion of the oligoTEAs is affected by the hydrodynamic size, shape, and hydration state of the molecule. The diffusion coefficient of each oligomer was calculated by tracking the center of mass of the macromolecule over time. The self-diffusion coefficient of a Brownian particle can be related to the mean squared displacement using:

$$2dDt = \left\langle |r(t) - r(0)|^2 \right\rangle \tag{3.2}$$

where d is the number of translational dimensions, D is the self-diffusion coef-

ficient, t represents time, and $r(t)$ is the distance traveled as a function of time.[60] The MD diffusion was compared to experimental results using data from variable temperature pulse field gradient (PFG) NMR, as shown in Figure 3.8. The data follow expected trends in that these macromolecules diffuse quicker at higher temperatures or shorter oligomer length. We observed a similar range of diffusion coffiecients and trends in the data between the experiments and MD, providing validation for both techniques with respect to the oligomer dynamics. We observed, at most, a factor of three difference between the MD and the PFG NMR, which is a very encouraging result for this macroscopic property. Oligomers with a hydroxylated (DTT) backbone diffused slightly faster than the aliphatic backbone (BDT). This result can be rationalized from the hydration effect caused by the more hydrophobic BDT backbone, or stronger hydrogen bonding in the DTT hydroxylated backbone resulting in a more collapsed, faster diffusing oligomer.

3.4 Conclusions

In this work, we used atomistic models to simulate sulfonated oligoTEAs and characterize their chain dynamics, conformational ensemble and mobility a function of synthetic length (2mer to 12mer) and individual monomer functional groups. We demonstrated that entropic and hydrophobic forces can promote oligomer collapse of these flexible structures. At atomistic time scales, this collapse is stronger than intramolecular electrostatic repulsion, which was validated by experimental results. Comparison of individual monomer contributions suggest that changes in the rigidity of the backbone have a stronger effect than changes to the pendant groups. While high computational costs limit the statistical certainty of certain metrics, Molecular Dynamics simulations have provided experimentally unobtain-

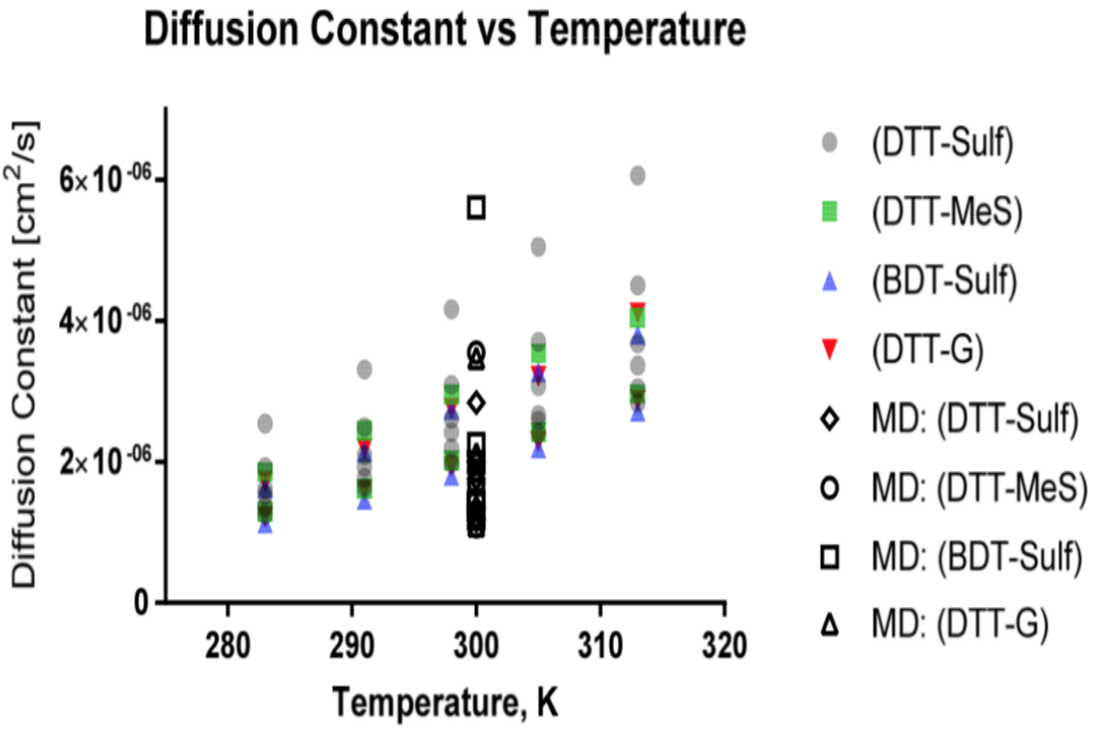

Figure 3.8: Diffusion data from both single-chain MD simulations (shown as open symbols as in the attached key) and PFG NMR in water for a range of oligoTEAs (shown as colored symbols).

able insight into the ensemble of highly flexible oligoTEAs. This methodology can be used to characterize other short flexible oligomers, which will further the understanding of sequence-structure relationships toward the design of novel foldamers and macromolecular architectures.

CHAPTER 4

COMPUTATIONAL MODELING OF DIFFUSION IN A NOVEL COVALENT ORGANIC FRAMEWORK WEAVE

4.1 Introduction

The synthesis of woven materials that resemble textiles in their interlacing of molecular strands is an emerging class of new materials.[61–63] These can be 3D Covalent Organic Frameworks (COFs)[61,63] or 2D polymer materials.[62] These materials are intriguing for the novel properties that they might possess, or their potential applications in gas storage, adsorption, optoelectronics or tailored surfaces with "smart" nanoscale morphologies.[61–63] The recent emergence of a woven Covalent Organic Framework[61] marked the first time that the concept of a fabric has been expressed at the molecular level. COFs are similar to their larger Metal Organic Framework "cousins" (MOFs) and Zeolitic Imidazolate Frameworks (ZIFs). They are crystalline nanoporous materials that are designed using the synthesis principles of reticular chemistry.[64] COFs are made by a combination of organic building units (known as "connectors" and "linkers") that are covalently linked to form extended ordered structures. They have have been synthesized into both 2D[65] and 3D[66] materials. Due to their low density, large surface area, tunable pore size, and designable functionality, COFs have been used for gas storage,[67–69] photoelectronics,[70] catalysis,[71] and chemosensing.[72]

In a similar fashion to conventional fabrics, the "weaving" of organic threads creates a strong, but elastic, material that can retain its shape under deformation and stress. COF-505, for example, was shown to exhibit a ten-fold increase in elasticity from its metallated form, an integral and critical part of the synthesis, and its

final, demetallated, woven form.[61] In this study, we will show how woven Covalent Organic Frameworks, such as COF-505, can be modeled using molecular simulation and then illustrate the potential of this, as yet experimentally unexplored, woven COF to act as a molecular sieve with tunable adsorption as a function of temperature and pressure.

4.2 Computational Modeling of Porous Materials

The atomic-scale conformations and forces in porous materials play a key role in gas adsorption dynamics. For rigid microporous materials, like MOFs, the standard computational method used to capture gas adsorption is Grand Canonical Monte Carlo (GCMC).[73] This approach couples a rigid scaffold using highly accurate *ab initio* potentials with simpler (computationally faster) united atom ("coarse-grained") potentials for the adsorbents. The inherent flexibility and microporous structure (<2 nm pores) of COF-505 prohibits this methodology. Instead, we will use atomistic (so-called "all-atom") Molecular Dynamics (MD) to predict the structure of COF-505 under thermal and mechanical stress, and determine the diffusional properties of guest molecules residing within the pores. This approach has been used to describe the diffusion of small molecules in MOFs and Silica Zeolites.[74–76]

The ability of Molecular Dynamics to accurately predict structural and dynamical properties is largely determined by the appropriateness of the selected force field, which describes short-range and long-range inter- and intra- molecular interactions. Molecular modeling simulations usually rely on one of the many published force fields, of which common examples are Dreiding,[77] CHARMM,[78] or OPLS.[37]

In the case of COF-505, none of the previously published force fields contained sufficient parameters to describe all of the atoms that are present. We chose to adapt and expand an existing force field, OPLS due to its widespread use for organic molecules. The OPLS force field, with its numerous parameter set expansions,[79–81] has the most inclusive list of parameterized atom types. OPLS was designed to be accurate for condensed phases of organic molecules and was originally parameterized to fit experimental data for the density and heat of vaporization of many liquids. This makes it the ideal platform upon which to simulate the unusual woven COF-505.

Modern force field development is usually concerned with achieving three aims: accurate atomic or molecular potentials, validation against known macroscopic properties, and the transferability of the force field. Gaps in our understanding of atomic interactions and the lack of experimental data pertinent to the molecular scale are often addressed by using first-principles quantum mechanical calculations to calculate the missing information.[82] In this approach, force field parameters are obtained by fitting calculated Density Functional Theory (DFT) energies to classical potential functions. Such an approach allows developers to expand the predictive abilities of the model, since experimental measurements were not required to validate these potential functions. While fitting parameters to DFT data alone is generally sufficient for molecular systems, it can be limited in systems with complex, long-range atomic environments such as polymer networks. As a result, we looked to fitting both to DFT *and* experimental data.

In the case of COF-505, we are particularly interested in matching experimental crystal structure and elasticity, since these are essentially the only experimental information known about this new material. But because these macroscopic proper-

ties result from both enthalpic and entropic contributions, parameterizing against these metrics is particularly challenging. Current best practices recommend an iterative approach where both atomic potentials and macroscopic properties are optimized in sequence.[83]

The historical goal of force field development is to produce parameters that can describe related, or as yet unknown, materials, a property known as transferability.[84] As molecular models tackle more specialized and complex systems, determining transferable parameters can either become infeasible or unrealistic.[85] And, indeed, parameter transferability is rarely achieved in practice, except for simple homologous series of chemical species. Our goal in this study was to create an effective force field that captures the known characteristics of COF-505, without any particular concern for parameter transferability. Given that this is the first synthesized woven COF, this is a reasonable starting point. Future Molecular Dynamics studies of any future interwoven deformable crystals are sure to benefit from the creation of this force field, through its exploration of atomistic and macroscopic parameterization.

4.3 Force Field Development for COF-505

Molecular Dynamics solves Newtonian equations of motion as a means to follow the time evolution of atomic/molecular trajectories in phase space. The aim, during the creation of a force field, is to find a suitable mathematical form for the interatomic potential and an associated set of parameters that accurately describes the thermodynamic and kinetic properties of the system under the conditions of interest. For COF-505, that means we want the woven material to behave realistically,

under not only standard temperature and pressure conditions, but also under the physical conditions that it will experience in its use for chemical sensing, gas adsorption, or other chosen uses. We expect the most interesting properties of woven materials to occur when the organic fabric is deformed due to variable temperature and pressure. Hence, using first-principles calculations to develop the force field would not be particularly appealing since DFT calculations are invariably limited to studies at 0 K. On the other hand, we will need DFT calculations (as described below) to help us model charge-charge interactions. Our approach for creating a model for COF-505 must then combine the accuracy of DFT force field development for some properties with validation against the very few experimentally known macroscopic properties of this new material.

4.3.1 Model Development for Woven Organic Materials

Woven materials contain an inherent porosity with long-range order. Whether compressing the mesh will fully close any of the pores is unknown. In order to accurately represent COF-505, we validated our model by attempting to reproduce two known macroscopic properties: 1) experimental elasticity measurements for the Young's Modulus of COF-505, and 2) unit cell parameters for the *metallated* COF-505, as determined by powder X-ray diffraction.[61] Note that the unit cell parameters for the demetallated version are unknown.

As a precursor to optimization against experimental results, we needed to determine OPLS force field parameters that would describe both the metallated *and* demetallated weaves. The OPLS force field and its accompanying parameter set expansions,[37,79–81] captured most of the atomic interactions in COF-505. But there were still around 60 missing parameters, including 28 charges, three dihe-

dral (4-atom) interactions, and the Cu-N interaction in the metallated COF-505. This introduced two additional optimization objectives: 1) predicting appropriate charges using Electrostatic Potential calculations, and 2) matching missing interatomic potentials against energies predicted by Density Functional Theory calculations.

In the course of developing a force field for COF-505, we found that we needed a cyclical method to achieve this multi-objective optimization. While the charges and the DFT optimization proved to be the least important objectives in the context of our goals of understanding gas diffusion, we needed to perform this step first in order to complete the force field. Only then could we attempt to match macroscopic values for the elasticity and metallated crystal structure.

4.3.2 Charge interaction

The electrostatic interaction between two atoms is typically calculated from the Coulomb energy between two static atomic point charges. These charges for new and unmodeled materials are invariably derived from DFT calculations. This has been used to update the charges used in many force fields, such as DREIDING[86] or MM3.[87,88] Of the methods readily available to calculate atomic charges, we have found ChelpG[89] and Merz-Kollman[90] to offer the best compromise between accuracy and computational cost since these methods calculate atomic charges from the electrostatic potential (ESP) derived from the results of Quantum Mechanical calculations. They can be used to assign point charges in the periodic structure using non-periodic clusters. Here we use the Merz-Kollman (MK) method since comparison studies[91] suggest that this method offers the best matching of electrostatic potentials. However, care must apparently be taken to account for the

directionality dependence of MK charges.[91]

The DFT functional and basis set chosen to determine the charges must balance both performance and accuracy. There is a temptation to rely on historic functional and basis set pairings like B3LYP/6-31G* due to convenience and perceived reliability. However, recent comprehensive benchmark studies[92]have shown that these QM methods are often less accurate than other choices and can sometimes provide misleading results.

In this study, we used the B97 functional for initial geometry optimizations and the more expensive PW6B95 functional for refined optimizations and energy calculations. The presence of copper in the metallated COF-505 restricts the basis set to a minimum of def2-TZVP. A dispersion correction is added to all functionals for increased long-range accuracy.[92] All DFT calculations were performed using ORCA, an *ab initio* quantum chemistry package.[93]

In selecting representative subsections of COF-505 to model, the sample cluster should have the same structure and environment as the bulk material of interest. We are ultimately interested in modeling COF-505 under mechanical and thermal stress. To that end, we wanted to calculate the material's characteristic charges over a range of suitably stressed atomic configurations. The ideal representative model is a molecular analogue of COF-505 containing all of the atomic types of interest; hence, only one suite of simulations would be needed to calculate all the necessary charges. In the experimental characterization of COF-505, Liu *et al.*[61] synthesized Cu(I)-bis[(1E,1'E)-1,1'-((1,10-phenanthroline-2,9-diyl)bis(4,1-phenylene))bis(N-([1,1'-biphenyl]-4-yl)methanimine)] [$Cu(PBM)_2$] as part of their own validation of the COF-505 structure. Similarly, we selected $Cu(PBM)_2$ (Figure 4.1a) as our molecular analogue for the charge variation simulations. We found

that only a few of the charges are the same for both the metallated and demetallated analogues [$(PBM)_2$]. In order to simulate the expansion and contraction of the weave material, the PBM linkers were forced to extend to certain distances apart, as shown in Figure 4.1a. The calculated DFT energies covered a sufficient energy range (over many multiples of kT) to confirm that all possible configurational states were covered (Figure 4.1b). The charges for each state were calculated using Merz-Kollman fitting. The average charge of each atomic type was used as a starting guess for subsequent optimizations described below.

4.3.3 Cu-N interaction

Metal-ligand interactions are difficult to parameterize due to the complexity of their electronic structure. Copper coordination complexes are subject to Jahn-Teller instability, in which *d*-electrons lead to non-symmetric structural chemistry in Cu-N bonding.[94,95] Any general theoretical description of Cu coordination complexes needs to capture the electronic effect of the ligand field stabilization energy (LFSE). Fortunately, the Cu-N bonds present in $Cu(PBM)_2$ are placed in a unique environment that makes it easier to model. The presence of the phenanthroline backbone attached to the bonding nitrogen atoms restricts the allowed configurational space. In addition, the copper is almost completely encapsulated within the phenanthroline environment, shielding the copper from external interactions. Finally, no free electrons are present in Cu(I), allowing us to use a simple metal-ligand interaction with only Cu-N bonds and N-Cu-N angles needed to be taken into account.

Consistent with the charge calculations, DFT geometry optimizations for the Cu-N interaction were run using PW6B95/TZVP. The representative model is

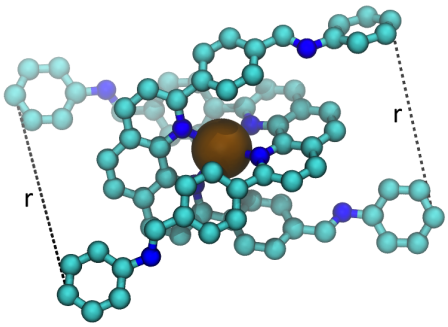

(a) Representative model for the metallated COF-505 monomer ($Cu(PBM)_2$).

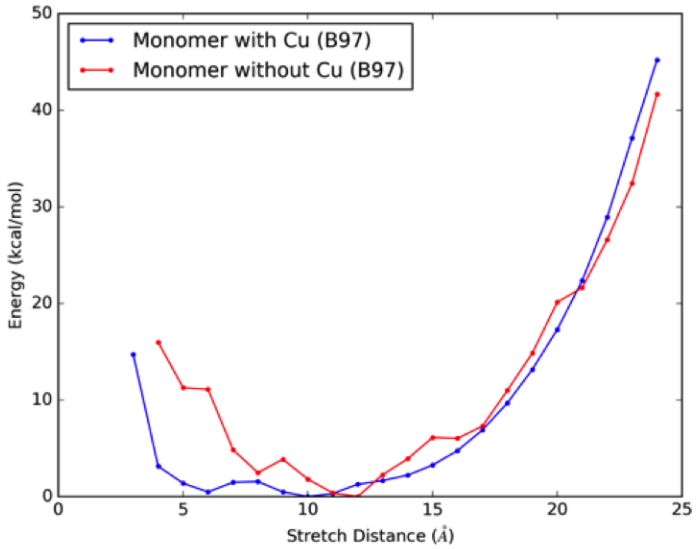

(b) Monomer energies for both the metallated (blue) and demetallated (red) versions of COF-505.

Figure 4.1: (a) Visualization of the model for the metallated COF-505 monomer ($Cu(PBM)_2$). The large central brown atom represents the copper atom, the dark blue atoms are nitrogen and the teal-colored atoms are carbon. Hydrogen is omitted for clarity. Distance r represents the constraint imposed between PBM linkers during DFT calculations. The interatomic distance between two PBM ends, r, was varied to monitor the DFT-derived energy under stretched and compressed conditions. (b) Monomer energy of the metallated (blue dots connected by lines to guide the eye) and demetallated (red dots) versions of COF-505, showing that the minimum energy configuration differs significantly between the two systems. The x-axis describes the distance between the two PBM ends. An unusually broad energy minimum can be seen for both versions when these ends are between 8-15 Å apart, reflecting the elastic nature of the material. Both versions show a similar energetic response at longer distances. The demetallated version shows accessibility at short distances, presumably due to the bonding afforded by the presence of the metal which holds the structure more tightly together.

shown in Figure 4.2a below. The DFT energies were sampled at fixed Cu-N bond distances, allowing us to determine the force constant and equilibrium bond length. Figure 4.2b shows the Cu-N bond energy calculated from MD versus the DFT-derived energy. Looking at geometry-optimized configurations, we found that the CuN_4 metal-ligand complex deviated from a purely tetrahedral geometry. To supplement van der Waals (vdW) forces, we found that introducing the N1-Cu-N2 angle induced a planar driving force that provided more correct geometries. We empirically found that this degree of freedom helped improve the reproduction of the MD-derived lattice parameters, as described below. The DFT-derived Cu-N bond distance is 2.08 Å, which was well matched to the MD-calculated Cu-N bond distance of 2.10 Å. Both simulated bond distances are within an acceptable distance from the XRD Cu-N bond distance of 2.06 Å.

4.3.4 Dihedral interactions

The reaction between the copper(I)-bisphenanthroline connector with the benzidine linker produces a R-CH-N-R' bridge. There are three dihedral interactions associated with this bridge that were missing from the OPLS force field: CA-C!-NX-CW, C!-NX-CW-C!, and NX-CW-C!-CA. Here, CA is an aromatic carbon, C! is an aromatic carbon linking to another molecular subsection, and the bridge is composed of a nitrogen and carbon (NX and CW). To remedy this knowledge gap, we ran DFT geometry optimizations using PW6B95/TZVP with phenyl-CH-N-phenyl as the representative cluster (Figure 4.3a). Torsional scans (in 15-degree increments) were performed for each missing dihedral, which served as a training set for the force field parameterization. The dihedral parameters were optimized until the energy predicted by the MD force field matched the energy predicted

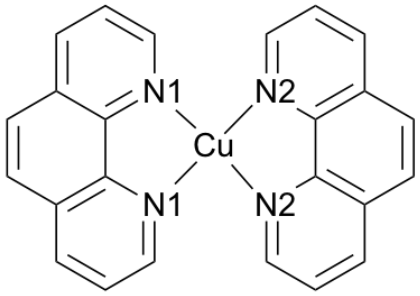

(a) Cu(Phenanthroline)$_2$ representative model

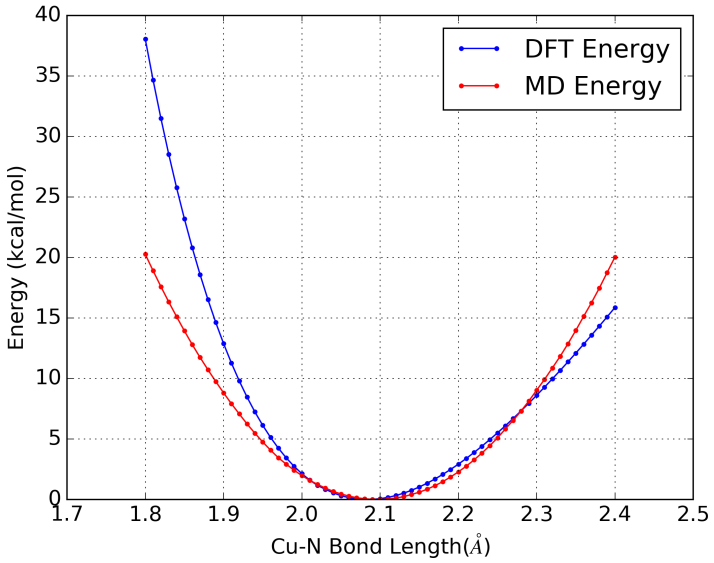

(b) Cu-N bond energy

Figure 4.2: (a) A representative model for Cu(Phenanthroline)$_2$ simulated using DFT. b. Bond energies derived from DFT and MD calculations for the metallated Cu(PBM)$_2$ material are shown as a function of a fixed Cu-N bond distance. The blue dots show the DFT-derived energies. The red dots show the best fit of the MD-derived model force field to the DFT data. Lines between dots are shown to guide the eye. Close reproduction of the two sources of the energy data can be clearly seen for up to ±10% expansions and contractions of the lattice about the energy minimum.

from DFT. This methodology has been used many times to extend the OPLS force field.[80,81,96] The dihedral parameters continued to be updated during the process of matching macroscopic properties. Figures 4.3 show the final torsional energies predicted by MD for each parameterized dihedral.

4.3.5 Crystal structure

Optimizations of crystal structures usually involve the minimization of two metrics: displacement of atom positions and crystal lattice parameters.[84,97] Many published force fields use the Root Mean Squared (RMS) displacement of atom positions as a validation of their parameterization.[98–100] In the case of COF-505, the crystal structure is strongly coupled to long-range and nonbonded energy terms. Deformation of the crystal lattice would cause all the atomic positions to shift, making RMS displacement a weak target for optimization. Instead, it was more efficient to optimize directly against lattice parameters, which provided a more holistic measure of parameter accuracy.

Optimization against lattice parameters required experimental data for validation. For COF-505, the experimental unit cell parameters were determined with 3D electron-diffraction tomography and refined with powder x-ray diffraction studies. Once the space group was determined, a structure model was built and validated against the PXRD data.[61] Experimental lattice parameters are only available for the metallated COF-505, limiting our ability to validate the structure of the demetallated, woven COF-505 crystal.

To calculate the model lattice parameters, Molecular Dynamics simulations were run for a unit cell of the metallated COF-505 structure. The system was

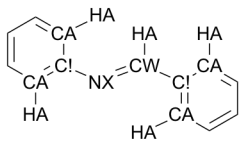

(a) Representative model for R-CH-N-R' bridge

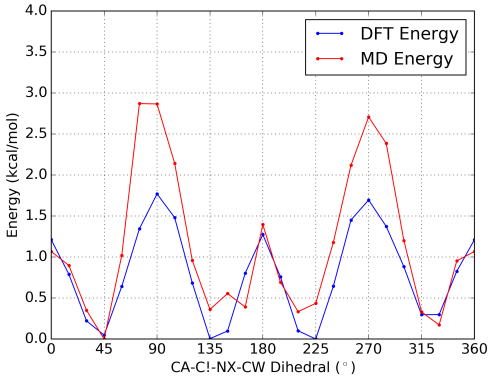

(b) CA-C!-NX-CW

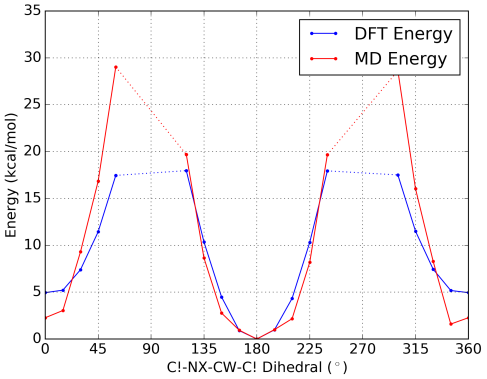

(c) C!-NX-CW-C!

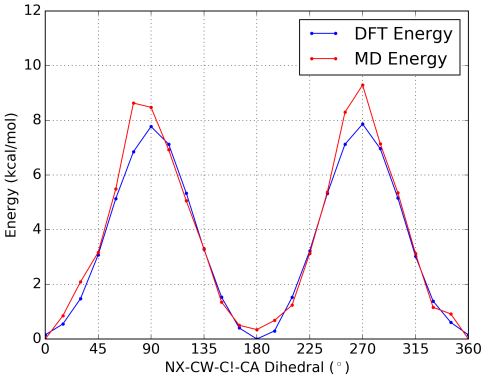

(d) NX-CW-C!-CA

Figure 4.3: (a) A representative model for the R-CH-N-R' bridge was simulated using DFT. The torsional energy calculated from DFT simulations versus the energy predicted from MD are shown for (b) CA-C!-NX-CW, (c) C!-NX-CW-C!, and (d) NX-CW-C!-CA. The RMS errors are 0.57 kcal/mol, 4.5 kcal/mol, and 0.59 kcal/mol, respectively.

run with an isothermal, isobaric (NPT) ensemble at 300 K and 1 atm for 1 ns. Long-range electrostatics were handled using the particle-particle particle-mesh (PPPM) method. Periodic boundary conditions were utilized in all directions simulate bulk COF-505. The final lattice parameters are compared to experimental lattice parameters in Figure 4.4 below.

We found that lattice parameters were highly sensitive to the values used for the charges. The close-packed nature of the COF-505 structure meant that even slight variations in charge altered the entire structure. We expect that future improvements to the charge distribution could improve simulated lattice parameters.

4.3.6 Elasticity

Woven materials like COF-505 are promising due to the inherent flexibility present in this fabric-like material. To that end, elasticity was the most important parameterization target for our study. The experimental Young's modulus, a measure of anisotropic stiffness, was determined from AFM measurements and showed a 10-fold decrease in stiffness from the metallated to the demetallated COF-505.[61] Our target was to match the absolute calculated Young's modulus and try to approach the experimental ratio of elasticities.

Young's modulus is the uniaxial stiffness of material and measures a material's resistance to being deformed elastically when a stress is applied along a single axis. The formula for Young's modulus is shown in equation 4.1 below,

$$E = \frac{\sigma}{\epsilon} = \frac{P}{\partial L / L_0} \tag{4.1}$$

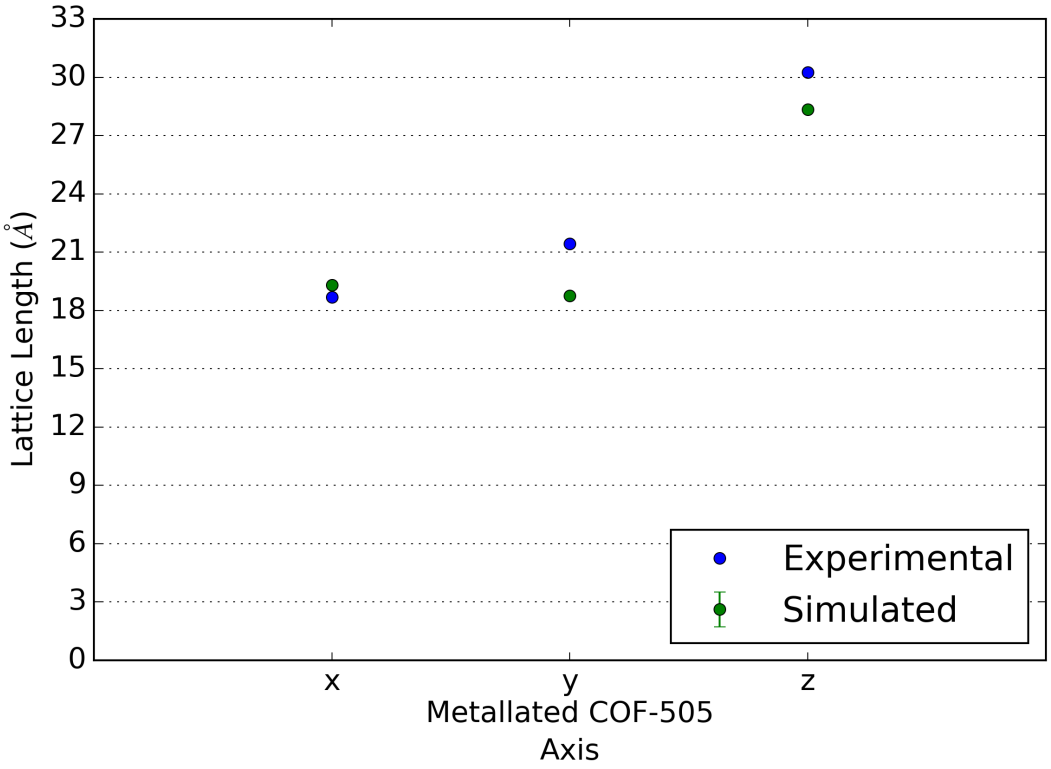

Figure 4.4: The experimental and simulated MD lattice parameters for the metallated COF-505 are compared. Both experimental and simulated MD lattice parameters retain the same 2:2:3 ratio for the a:b:c lattice parameters.

where E is the Young's modulus, σ is the stress, ϵ is the strain, P is the uniaxial pressure on the system, ∂L is the change in the corresponding axis length and L_0 is the original axis length. This formulation is only accurate within the linear elastic region. Accordingly, we restrict all elasticity simulations to $\pm 2\%$ axis deformation.[101] This dynamic deformation simulation method has been used by others to calculate the elasticity of similar materials: polymer?carbon nanotube composites[45,101] and thermosetting polymers.[44]

We employ our NPT ensemble methodology, described previously, to apply a constant external stress and to measure the corresponding strain. We used the annealed system as the initial state for elasticity measurements. The external pressure was varied at a rate of 0.01 GPa/ps, which is typical for MD studies.[45] Elasticity measurements at this stress rate exhibited hysteresis, as expected. To counteract this, the strain was cycled back and forth between $+2\%$ and -2% twice, which we found led to more consistent elasticity measurements.

The experimental elasticity was reported as an effective Young's modulus, neglecting anisotropy. Since the periodic computational cell is triclinic, the system is not isotropic. Thus, the effective Young's modulus was calculated by taking the average value in the $x-$, $y-$ and $z-$ directions. The calculated elasticity was compared to the experimental Young's modulus, as shown in Figure 4.5, below.

Through trial and error, we found that matching the experimentally measured metallated crystal structure did not guarantee matching its calculated elasticity. Similarly to the crystal structure, we found that the elasticity was highly sensitive to the long-range interactions, especially charge.

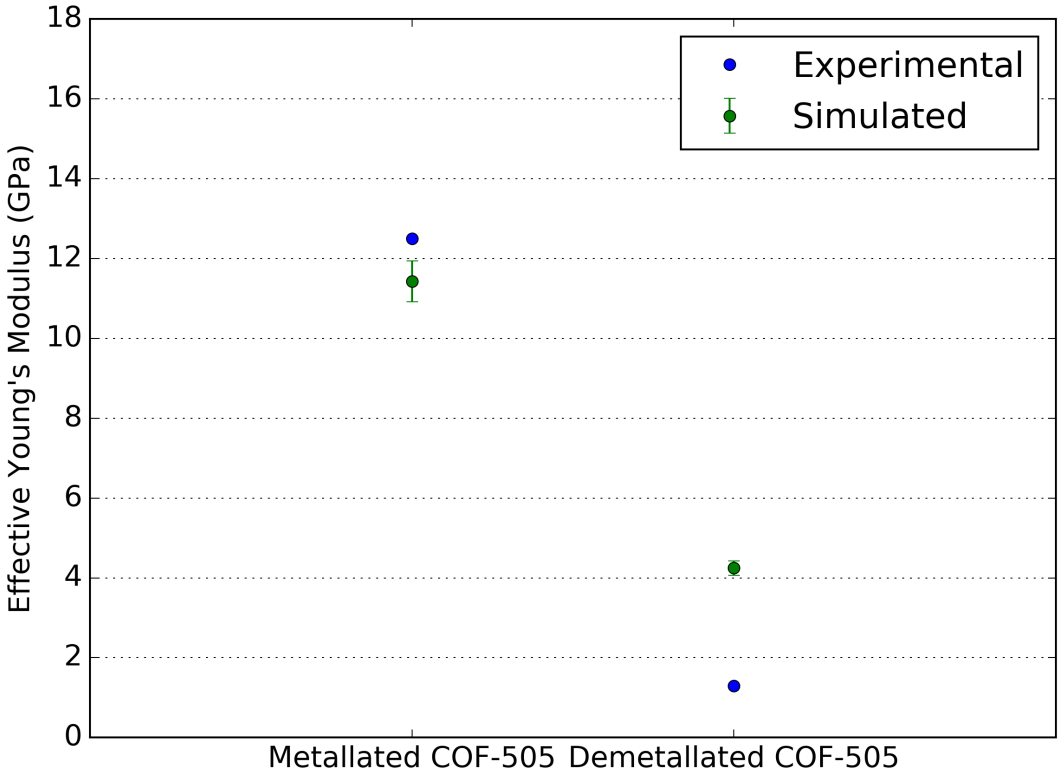

Figure 4.5: Comparison of the experimentally and MD-simulated values for the effective Young's Modulus. The simulated elasticity shares a similar order of magnitude and ratio with the experimentally determined elasticity.

4.3.7 Optimization Methodology

For a given form of the force field, there is a plurality of parameter sets that will accurately describe the energy and dynamics of a system under a certain set of conditions. A consequence of this observation is that defining a parameter set that will accurately represent many objectives can be difficult and tenuous. Therefore, establishing the scope and goals of a force field and parameter set is fundamental to a successful parameterization. Moreover, establishing the success of any single objective is nontrivial. The reader will therefore benefit from understanding the methodology used and the lessons learned in this study. All optimizations were performed using the python implementation of the NLopt nonlinear-optimization package.[102]

The two energy minimizations, the Cu-N interaction, and the dihedral interactions, were conducted by comparing the energies derived from gas-phase DFT and MD simulations. Because long-range interactions are neglected and atomic positions constrained, the optimization is fast and precise. The objective function was established as the sum of RMS errors between the DFT and MD potential energies in each atomic configuration. Assuming the starting parameters are close to the optimum, conventional gradient-based optimization methods are efficient. We found that the COBYLA[103] and Sbplx[104] algorithms produced the most consistent performance. COBYLA constructs successive linear approximations of the objective function and can handle inequality and equality constraints. This was useful during optimization of the Cu-N interaction so that charges did not vary unrealistically. Sbplx is a variant of the Nelder-Mead algorithm and can handle discontinuous functions while being very efficient and robust. Together, the energy error was reduced to <1 kcal/mol for the single-bonded dihedrals (CA-C!-NX-CW

and NX-CW-C!-CA) and <5 kcal/mol for the double-bonded dihedral (C!-NX-CW-C!).

The two macroscopic properties that we chose to calculate were more difficult to optimize. The high density of COF-505 and its sensitivity to long-range interactions influence both the crystal structure and the elasticity. It is impossible to determine *a priori* which parts of the force field and the parameter set will be most important for these objectives. Initial efforts focused on matching the crystal structure, since there was a discrepancy between experimental and simulated lattice parameters. The objective function of this optimization was the RMS error of the experimental lattice parameters against the simulated lattice parameters. In order to keep the optimization results consistent with DFT calculations and the other OPLS parameters, we initially imposed certain constraints. First, charges were restricted to be the same sign and magnitude predicted by DFT charge calculations. Second, we imposed a constraint on system charge neutrality. Empirically, we found that convergence was improved if the system charge was allowed to fluctuate within a narrow band (± 1), which prevented the parameters from getting trapped in a minimization well. Finally, only new parameters defined by this study were allowed to fluctuate. Similar to the energy minimizations, the COBYLA algorithm was useful for optimizing the lattice parameters while obeying constraints. In addition, Sbplx and evolutionary[105] methods were used for validation that the true minimum had been achieved. It is important to note that our approach to charge differs from the contemporary practice of leaving charges unchanged from their DFT values. Optimization of the lattice parameters would not have been possible without targeting point charges.

Despite the parameterization reaching an apparent minimum error, the final

lattice parameters for the metallated COF-505 still showed a discrepancy between experimental and simulation-derived lattice parameters (a,b,c). We wanted to understand whether the model was capable of reproducing the elasticity. The objective function was the RMS error of the experimental Young's modulus against the simulated effective Young's modulus. While initial elasticity calculations showed that the metallated COF-505 was more stiff than the demetallated COF-505, as expected, the exact values for elasticity and the ratio between the metallated and demetallated COF-505 elasticities did not match experiment. Using the same three charge and parameter constraints described above in the lattice optimization, the parameters optimized to the lowest possible error. Due to the nonlinear response of the elasticity to the parameter values, we could not rely on the COBYLA method to find a minimum. Here, we depended upon Sbplx to overcome the noisy macroscopic property measurements and narrow down the solution while COBYLA, brute force, and evolutionary methods served as validation.

Once we had determined the final minimum parameters to optimize the relative elasticities of metallated versus demetallated systems, we discovered two problems: First, the parameter set that optimized the ratio of elasticities and that which optimized the lattice parameters diverged from each other. Second, our existing constraints were too restrictive to allow us to match the experimental macroscopic properties. To address the first problem, we decided to use the aforementioned cyclical optimization process. The optimization for the energy minimization, lattice matching, and elasticity measurements would be sequentially optimized until all three were acceptable. To address the second problem, we relaxed the constraint that only new parameters could be varied, instead allowing a suite of OPLS parameter types to be adjusted for all atoms: pair potentials (vdW radius, vdW energy, point charge), three-body interactions (equilibrium angle and energy), and

four-body interactions (dihedral energies).

Unlocking all of those parameters posed a new problem: with an unbounded optimization, how do you decide which values are worth changing? If you haphazardly change the parameter set, you risk losing its compatibility with the core OPLS parameters. In the interest of reducing this riskiness and also promoting parameter transferability, we added one new constraint: parameters should only be changed if they cause a statistically significant improvement in the optimization goals. Otherwise, the default was for parameter values to stay the same.

To derive statistically significant parameters, the CRS2 (controlled random search variant) method was used to randomly sample parameter sets. Each parameter value was bounded to $\pm 10\%$ of its original value, to prevent excessive or unrealistic changes. The error function for lattice parameters and elasticity were plotted against each parameter value and fitted with first-order and second-order polynomials. If the coefficient of determination was significant ($R^2 >= 0.5$), then the parameter value was adjusted to the optimum lowest. This was process was iterated until no further statistical correlations were observed. This correlation-based optimization was coupled with the cyclical approach to generate the final parameter set.

4.3.8 COF-505 Force Field Results

The final parameters for the COF-505 force field offer a compromise between matching the experimental metallated COF-505 lattice parameters and the experimental Young's modulus. The simulated lattice parameters for the metallated and demetallated COF-505 are shown in Figure 4.6. The demetallated COF-505

structure removes the copper, which links the threads together. The relaxed demetallated unit cell, for which no experimental data are available, has an a:b:c ratio closer to 2:1:2. This deformation suggests the general flexibility of the demetallated structure. This was confirmed by looking at the anisotropic Young's modulus for the metallated and demetallated COF-505 materials, shown in Figure 4.7. The metallated COF-505 is most stiff along the $c-$axis, whereas the demetallated COF-505 has approximately equal flexibility in all lattice directions (as we might expect).

This force field emphasizes reliable lattice parameters and elasticity at standard temperature and pressure. We expect the model to reliably highlight the differences between the metallated and demetallated structure under thermal and mechanical stress. We will use this model to predict how gas molecules within the weave will behave under those same thermal and mechanical stresses. Future force fields could prioritize other parts of the force fields as more experimental data becomes available.

4.4 Diffusion Studies

4.4.1 Gas Diffusion Simulations

Understanding the diffusion of molecules within the pores of COF-505 will be important for all gas separation-related applications of this woven material. For isntance, separations can be derived by exploiting differences in the diffusion coefficients of the gas molecules. The diffusional behavior of molecules can be difficult to measure experimentally. In contrast, Molecular Dynamics offers an efficient

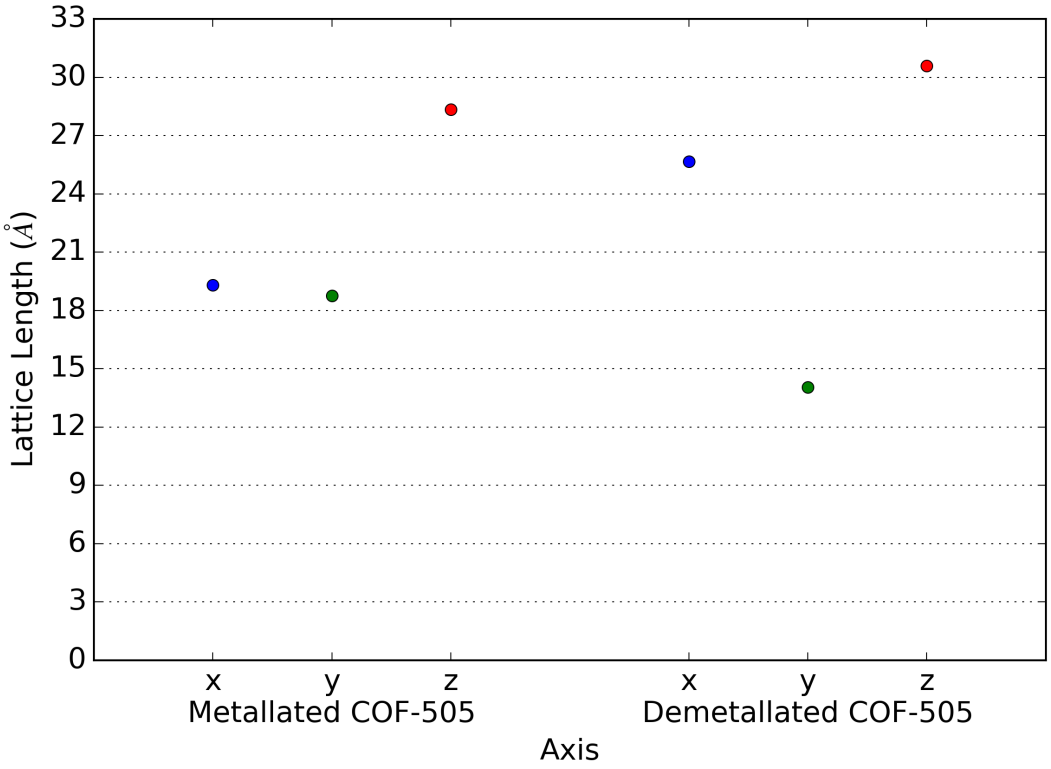

Figure 4.6: MD-simulated values for the lattice parameters of the metallated and demetallated versions of COF-505.

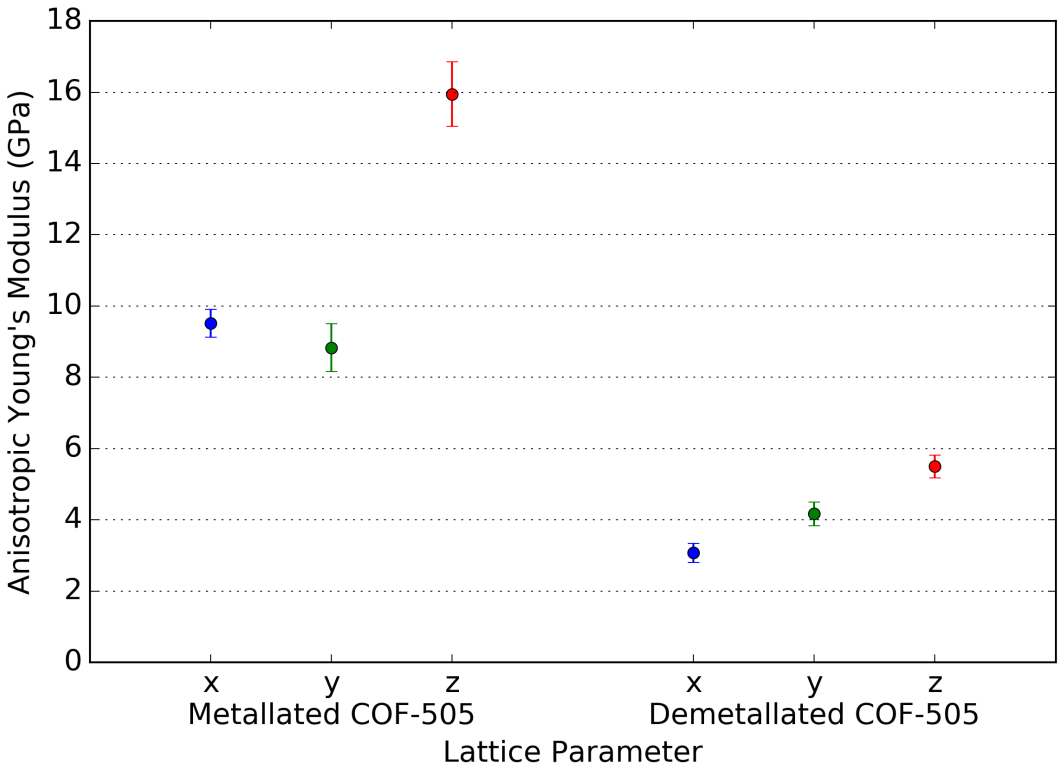

Figure 4.7: Simulated values for the anisotropic Young's Modulus for both the metallated and demetallated versions of COF-505.

compuational approach to predict how gas molecules travel through dense materials. The high density of COF-505 precludes the diffusion of large molecules at room temperature. Instead, we focus on the diffusion of small molecules of interest to material scientists.

Our first test involved the study of the simplest systems consisting of spherical atoms of different sizes, He, Ne, and Ar.[37] We also studied the diffusion of two diatomic molecules, O_2[106] and N_2[107], which are of interest in terms of permeability studies due to their similar size and shape.[108] H_2O was studied due to its relevance in filtration and separation applications. The TIP4P model was used to model water since it offers a good compromise between computational efficiency and charge accuracy.[53] CO_2 is of interest for carbon-capture purposes and offers a similar, but contrasting shape, to H_2O. The CO_2 molecule was modeled using a rigid three-site model with EPM2 potential parameters, which was optimized to give good agreement with experimental vapor?liquid coexistence curves.[109] The final molecule studied was CH_4, which is of interest to energy storage applications. In order to capture geometric constraints, all-atom OPLS parameters were used in this study.[37]

For particles which exhibit purely diffusive behavior, the self-diffusion coefficient can be calculated from the Einstein equation, below,

$$< r^2 >= 2dD_s t \tag{4.2}$$

where $< r^2 >$ is the mean squared displacement, d is the dimensionality, D_s is the self-diffusion coefficient, and t is time. Einstein's equation is based on the assumption that Brownian motion is present in the case where $< r^2 > \sim t$. The

mean squared displacement of the selected gas particles was measured using an MD derived trajectory. A unit cell of the metallated and demetallated COF-505 is annealed using an isothermal, isobaric (NPT) ensemble for 1 ns. The gas particle is randomly inserted into the material and briefly annealed for 10 ps to thermalize the particle. The particle trajectory is then collected over the following 1 ns. This was repeated using 10 random initial positions per temperature and pressure to improve statistics.

4.4.2 Transport Diffusion Simulations

For most practical applications, the transport diffusion or Fick diffusion coefficient is a better measure of transport phenomena. Transport diffusion measures diffusion as a function of the concentration gradient imposed on the system. Transport diffusion is distinct from self-diffusion in that the system is under non-equilibrium conditions with an associated mass flux. The transport diffusion coefficient can be calculated from Fick's first law[110], which in 1D is

$$J = -D_t \frac{d\rho}{dx} \tag{4.3}$$

where J is the mass flux, D_t is the transport diffusion coefficient, ρ is the fluid density and x is the diffusion distance.

In order to induce a concentration gradient, we employed boundary driven nonequilibrium molecular dynamics (BD-NEMD). In this method, an external force is applied at the boundaries of the material in order to generate a steady-state density gradient. Periodic boundary conditions ensure that no particles are lost.

NEMD simulations[111] have been used to study water permeation[112,113], gas permeability[114], and transport of hydrocarbons.[115] This approach is similar to dual- control volume Grand Canonical Molecular Dynamics (DCV-GCMD) simulations[116], where a flow is generated by connecting the material under study to two reservoirs of fluids at different densities. However, BD-NEMD is purely deterministic since no stochastic moves like particle insertion and deletion are needed.

While previous NEMD studies used a slab of material surrounded by the fluid of interest, we chose to use a long continuous periodic material. This allowed us to exert thermal and mechanical forces on the system without the demetallated COF-505 contorting to unrealistic shapes. To prepare the NEMD system, a system length of five unit cells was annealed using an isothermal, isobaric (NPT) ensemble for 1 ns. The gas molecules were randomly placed within the simulation cell[117] and briefly equilibrated using an isothermal (NVT) ensemble for 10 ps. BD-NEMD simulations were run by applying a constant force to the gas molecules along the boundary. The COF-505 mesh was run with an NVT ensemble with a weak harmonic force applied to keep the material stationary. The gas molecules were run using a constant energy (NVE) ensemble to avoid artificially influencing the molecular trajectories. The BD-NEMD simulation was run for 5 ns, with data collection occurring after the first 0.5 ns. A schematic of the BD-NEMD simulation system is shown in Figure 4.8.

To explore any anisotropic diffusional characteristics, BD-NEMD simulations were performed along the a, b, and c lattice directions of the demetallated COF-505. Due to computational cost, we were limited to simulating only helium transport diffusion through the material. This has the added benefit of serving as a probe for concentration-driven porosity calculations.

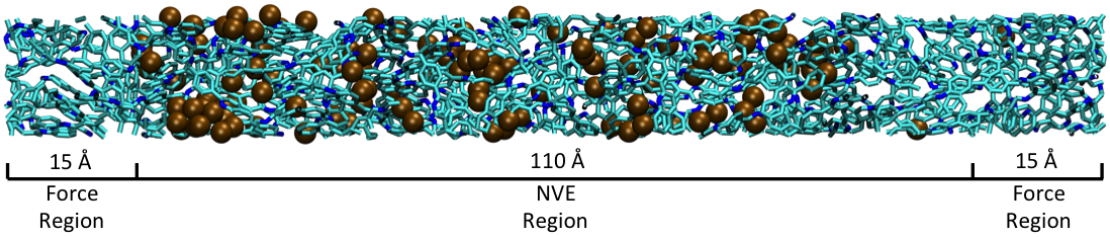

(a) Simulation cell for the BD-NEMD methodology.

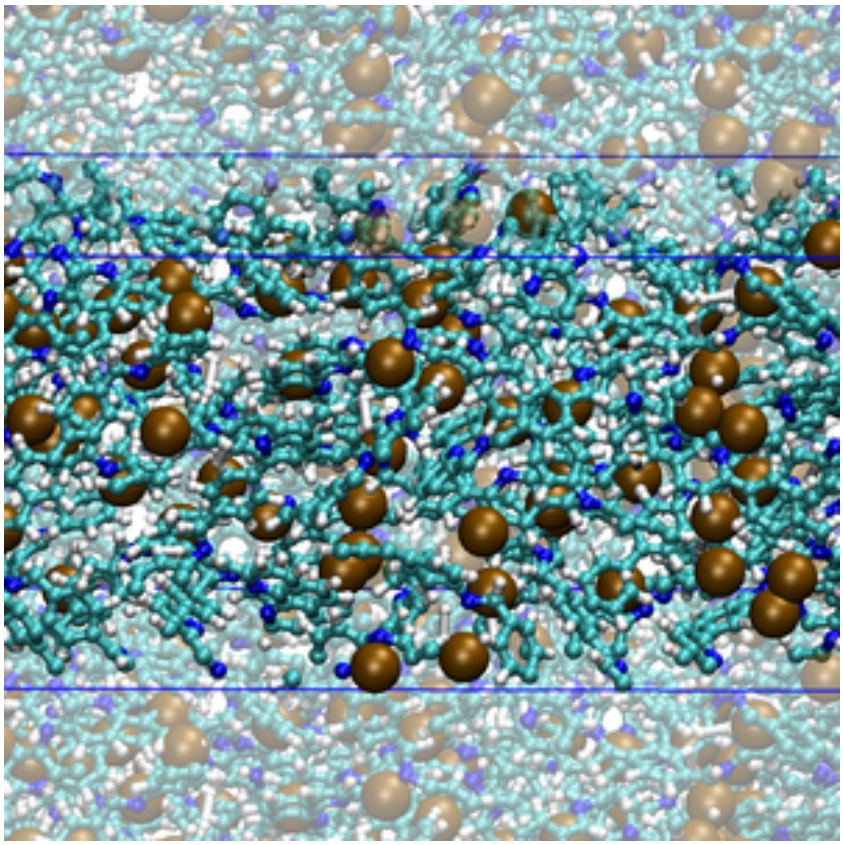

(b) Close up view of Helium transport diffusion simulation.

Figure 4.8: (a) Simulation cell for the BD-NEMD calculations of Helium transport diffusion through COF-505. Force is only exerted on helium atoms within the force region. Otherwise, the helium atoms are simulated with an NVE ensemble. The brown atoms represents helium, the dark blue atoms are nitrogen and the teal atoms are carbon. Hydrogen atoms are omitted for clarity.(b) Close up view of helium atoms penetrating the cof weave structure.

4.5 Results

4.5.1 Characterization of Diffusion in COF-505

Single particle gas diffusion simulations were run for He, Ne, Ar, O_2, N_2, H_2O, CO_2, and CH_4 at four temperatures (200 K, 300 K, 400 K, and 500 K) and three pressures (-1000 atm, 1 atm, and 1000 atm) to show the trends and limits in behavior. Data for each gas, temperature and pressure state were collected over 10 ns, totaling 840 ns of simulation time for the study.

The self-diffusion coefficient for helium, for both the metallated and demetallated COF-505, is shown in Figure 4.9. Diffusion in the demetallated COF-505 is an order of magnitude greater than the diffusion in the metallated COF-505; the flexibility of the demetallated weave provides significantly fewer barriers to diffusion relative to the small size of helium. As expected, the diffusion of helium through the metallated and demetallated COF-505 is accelerated at higher temperatures. Pressure does not strongly influence diffusion for the metallated COF-505; however, low pressure conditions allow particles to diffuse more freely in the demetallated COF-505. This shows that the inherent flexibility of demetallated COF-505 can be harnessed to improve diffusion under varying mechanical stress.

We showed that diffusion depends on particle size, as shown by the self-diffusion coefficients of He, Ne, and Ar at 300 K and 1 atm. in Figure 4.10. All three exhibit faster diffusion in the demetallated COF-505. Comparing the three noble gases shows that the size of the particle has the strongest effect on diffusion, with He traveling faster than Ne and Ar for both the metallated and demetallated materials.

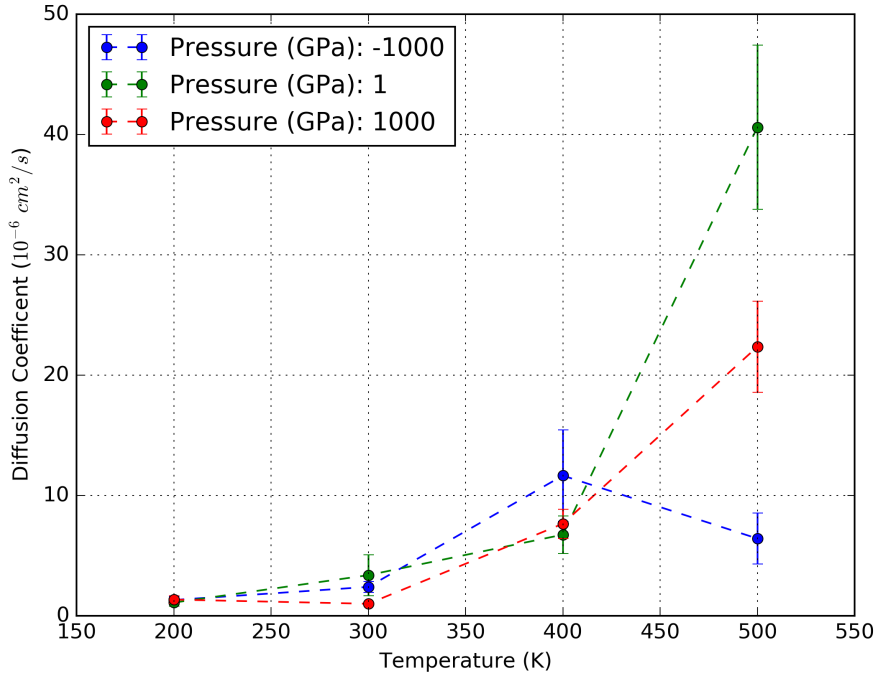

(a) Helium Diffusion in Metallated COF-505

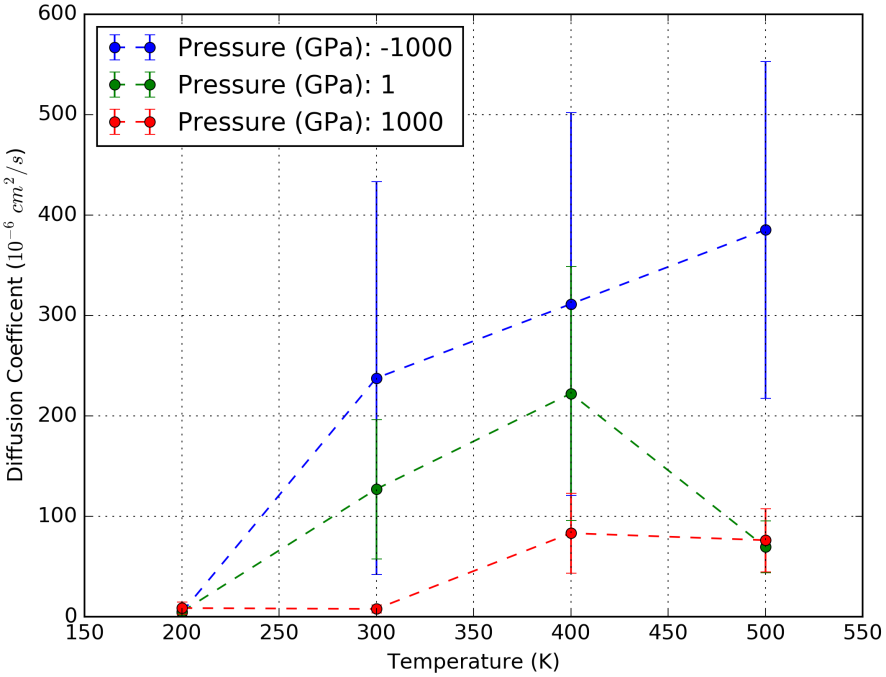

(b) Helium Diffusion in Demetallated COF-505

Figure 4.9: The self-diffusion coefficient for helium is shown within (a) metallated COF-505 and (b) demetallated COF-505.

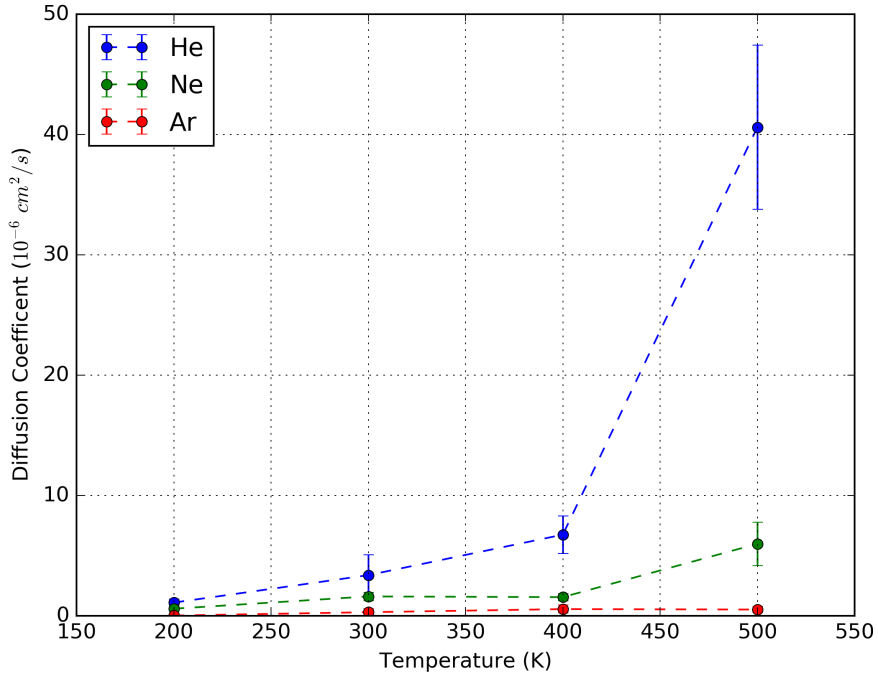

(a) Noble Gas Diffusion in Metallated COF-505

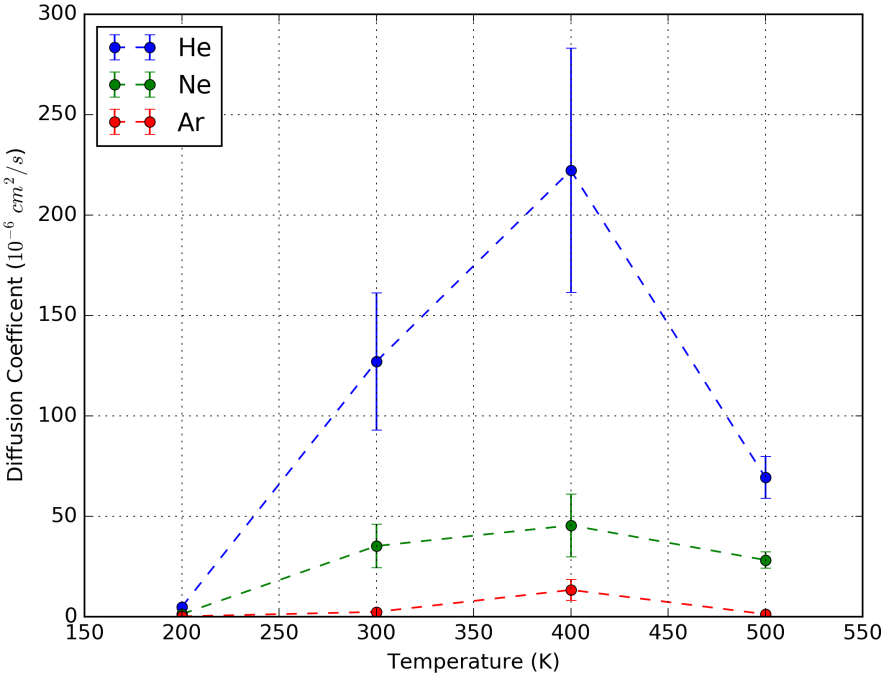

(b) Noble Gas Diffusion in Demetallated COF-505

Figure 4.10: Self-diffusion coefficients for helium, neon, and argon at 1 atm and 300 K are compared for both (a) metallated and (b) demetallated COF-505.

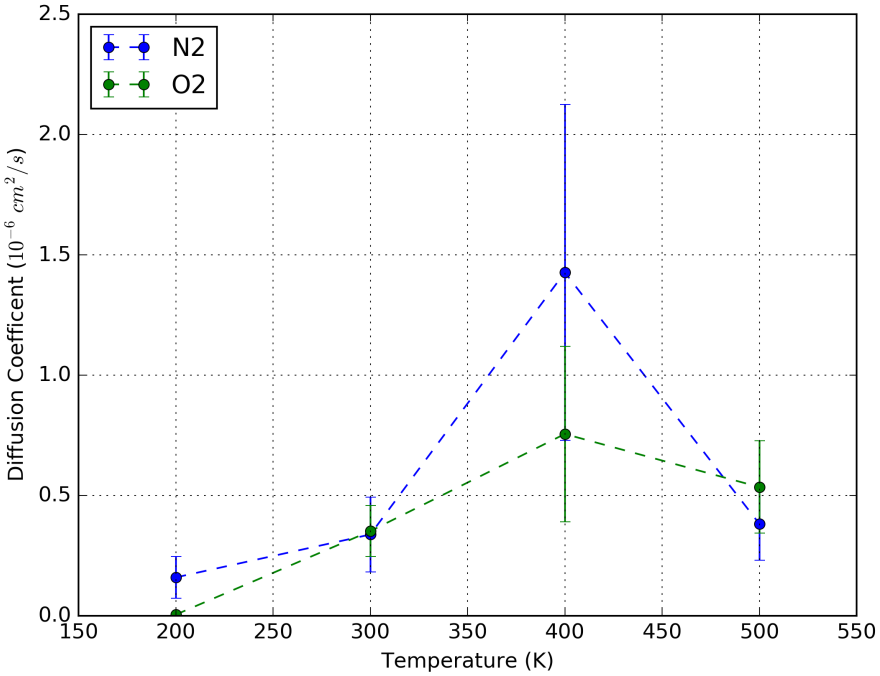

(a) Diatomic Molecule Diffusion in Metallated COF-505

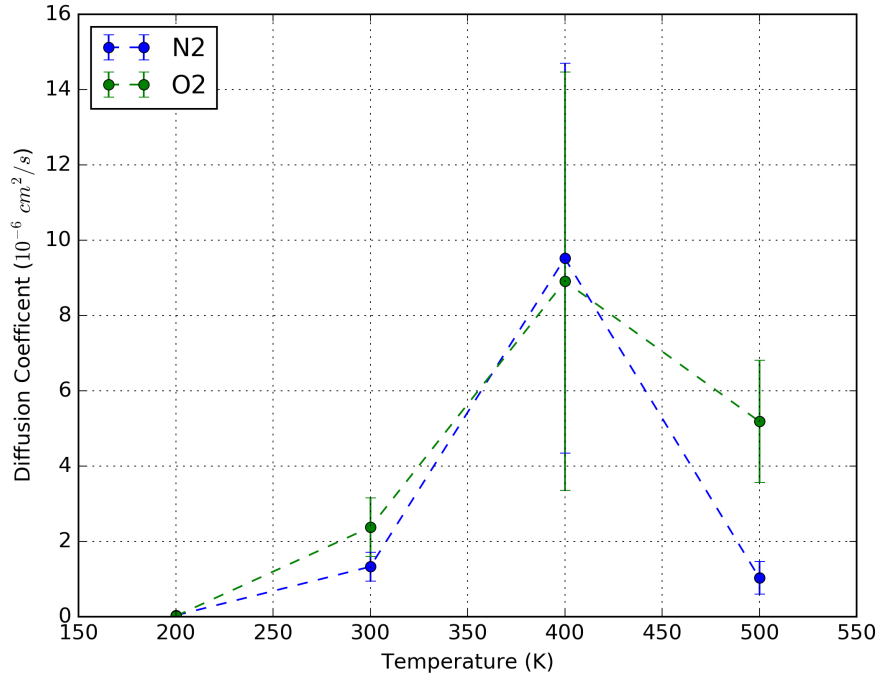

(b) Diatomic Molecule Diffusion in Demetallated COF-505

Figure 4.11: The self-diffusion coefficients for O_2 and N_2 at 1 atm and 300 K are compared for (a) metallated and (b) demetallated COF-505.

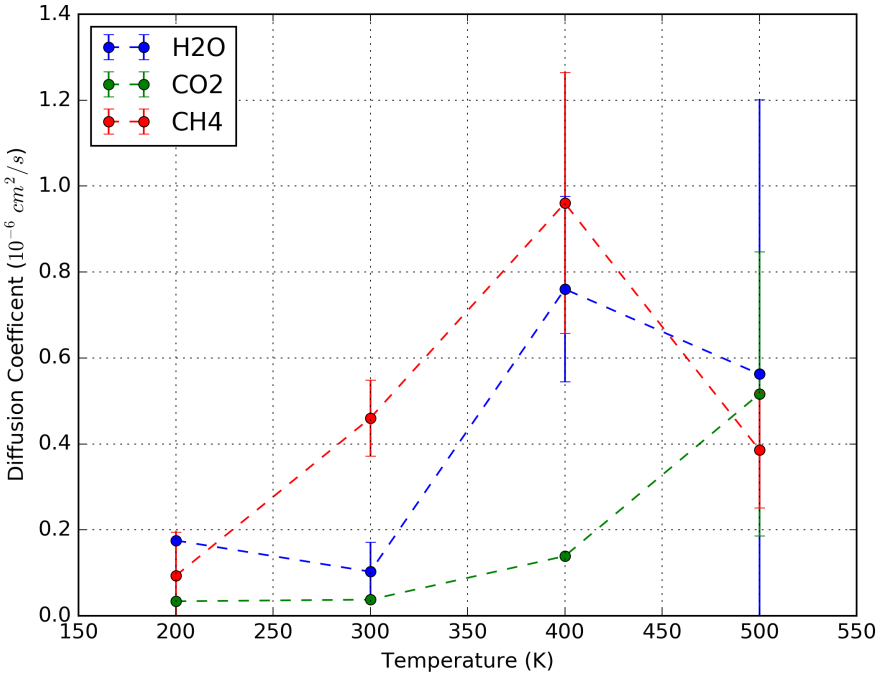

(a) Triatomic Molecule Diffusion in Metallated COF-505

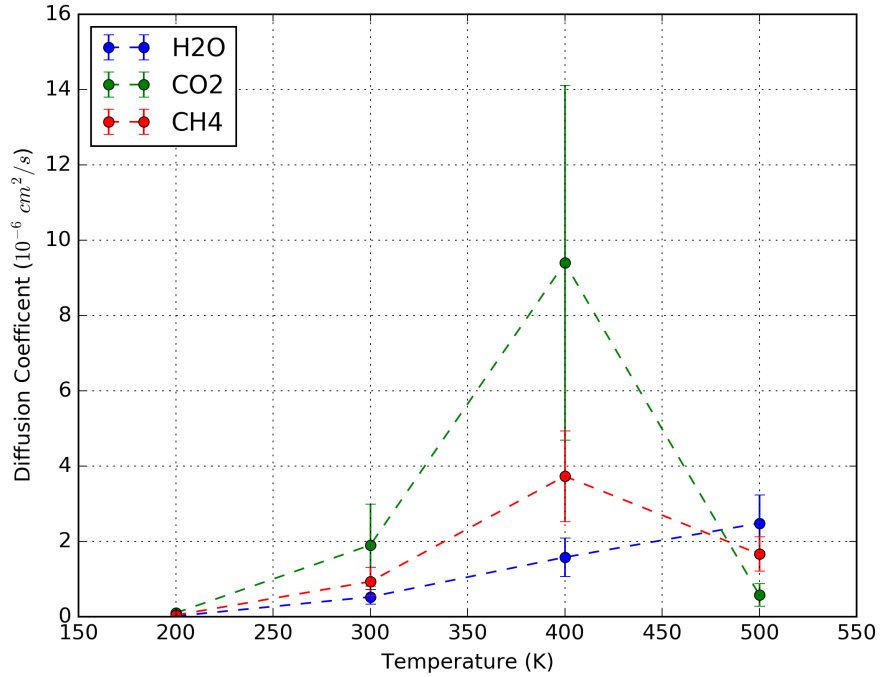

(b) Triatomic Molecule Diffusion in Demetallated COF-505

Figure 4.12: The self-diffusion coefficients for H_2O, CO_2, and CH_4 at 1 atm and 300 K are compared for (a) metallated and (b) demetallated COF-505.

The self-diffusion coefficients for the diatomic molecules, O_2 and N_2, and the triatomic molecules, H_2O, CO_2, and CH_4, are shown in Figures 4.11 and 4.12. The high density and restrictive nature of the pore channels restricts diffusion within both the metallated and demetallated COF-505. In a similar way to the monoatomic gases, diffusion is dependent on temperature for both the metallated and demetallated COF-505, but only the demetallated material shows pressure-dependence. A comparison of the self-diffusion coefficient of O_2, N_2, H_2O, CO_2, and CH_4 shows that the diffusion of all five polyatomic molecules are largely the same. This suggests that diffusional speed can only be regulated in molecules that can already freely travel through the material, such as the noble gases.

NEMD transport diffusion simulations were run for helium at four temperatures (200 K, 300 K, 400 K, and 500 K) and three pressures (-1000 atm, 1 atm, and 1000 atm) to show the trends and limits in behavior. Five replicate simulations with different random seeds were run for each temperature and pressure, allowing us to compile 25 ns of data per state. The high density of COF-505 necessitated a correspondingly high helium density of 16 kg/m^3 (100x density at STP) and a pressure gradient of 500 GPa at the boundary region to drive transport diffusion of helium and derive a strong concentration gradient. While the pressure gradient is in excess of experimental conditions, we expect the trends to be representative.

The transport diffusion coefficients for He within the demetallated COF-5050 along the a, b, and c lattice directions is shown in Figure 4.13. In a similar way to the self-diffusion coefficient results, the transport diffusion exhibits a stronger dependence on temperature than pressure. This suggests that pressure-driven diffusion through COF-505 will be limited by the high density of the material.

To show the dependence of transport diffusion on diffusion pathway, the trans-

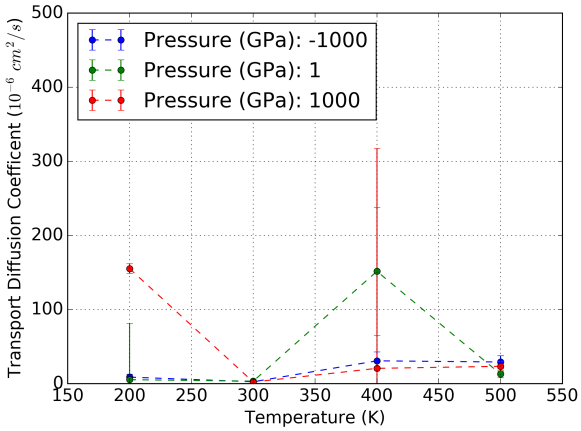

(a) Transport Diffusion Along the X-Direction

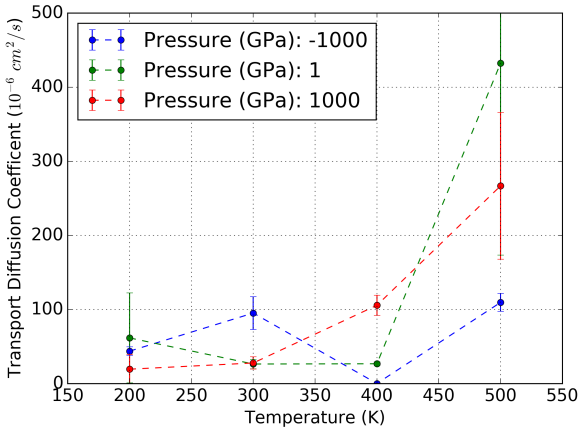

(b) Transport Diffusion Along the Y-Direction

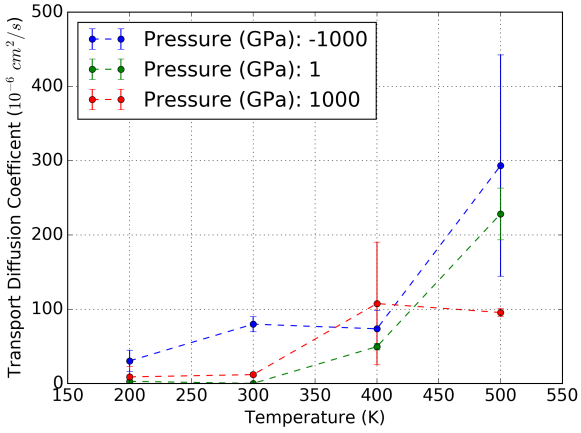

(c) Transport Diffusion Along the Z-Direction

Figure 4.13: The transport diffusion for He along the (a) x-direction, (b) y-direction, and (c) z-direction as a function of temperature and pressure. Error bars estimate the standard deviation of individual transport diffusion samples.

port diffusion coefficient of He along the a, b, and c lattice directions at 300 K and averaged across all pressures is compared in Figure 4.14. The results suggest a preference for helium to diffuse along the c lattice, with $\sim$8 times the rate of diffusion compared to the a lattice. This direction is orthogonal to the direction of the molecular threads, suggesting that pores between crossing threads are the most available pathways. Diffusion along the b lattice shows a similar trend, with $\sim$7 times higher rate of diffusion compared to the a lattice. To illustrate the diffusional pathways, the transport diffusion simulations were used to generate spatial distribution maps for helium diffusion at 300 K and 1 atm along the a, b, and c lattice directions, shown in Figure 4.15. The spatial distribution maps were consolidated into one unit cell for clarity. Pressure-driven diffusion along the a lattice direction shows helium aggregation into vertical pockets, whereas diffusion along the b and c lattice directions show preferential pathways, leading to a faster transport diffusion.

4.6 Discussion and Conclusions

As the first woven material consisting of molecularly defined strands, COF-505 has unique properties that we are only just beginning to understand. The inherent flexibility of woven materials, coupled with their resistance to mechanical stress, make COF-505 a potentially interesting material for gas separations. In the absence of extensive experimental work, we explored how COF-505 could be used for selective separation of gas molecules.

The high density of COF-505, coupled with its elasticity, made this material challenging to model. Our approach required simultaneous optimization of lattice

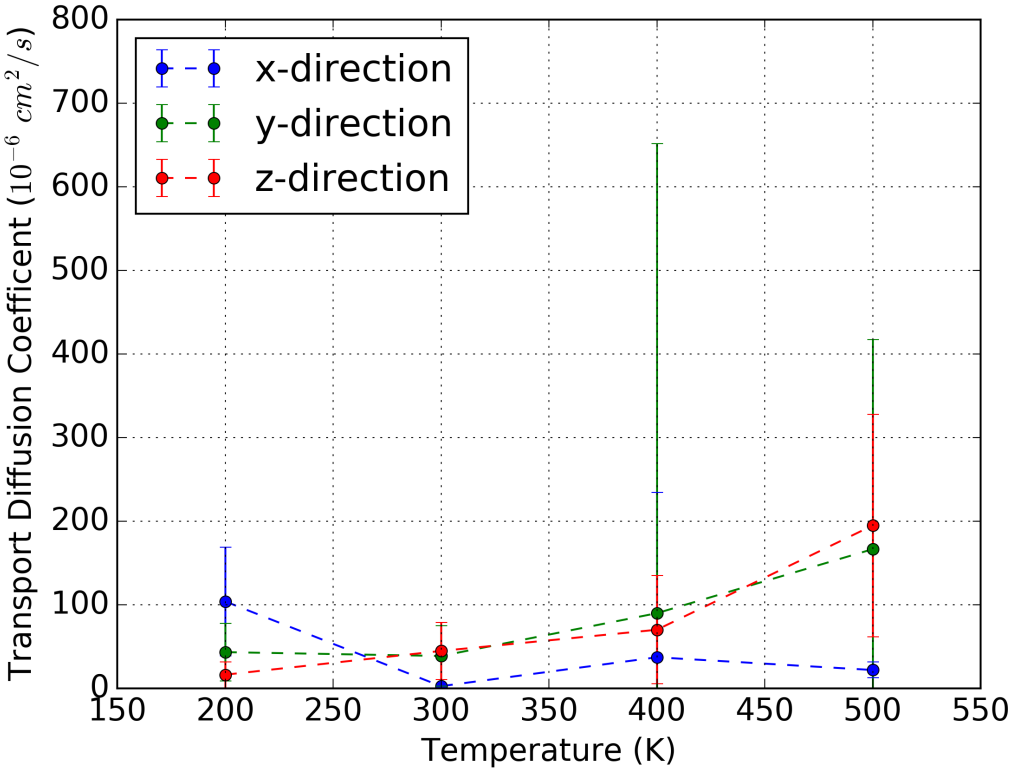

Figure 4.14: Transport Diffusion of He along the a, b, and c lattice directions are compared at 300 K and averaged across all pressures. Error bars estimate the standard deviation of individual transport diffusion samples.

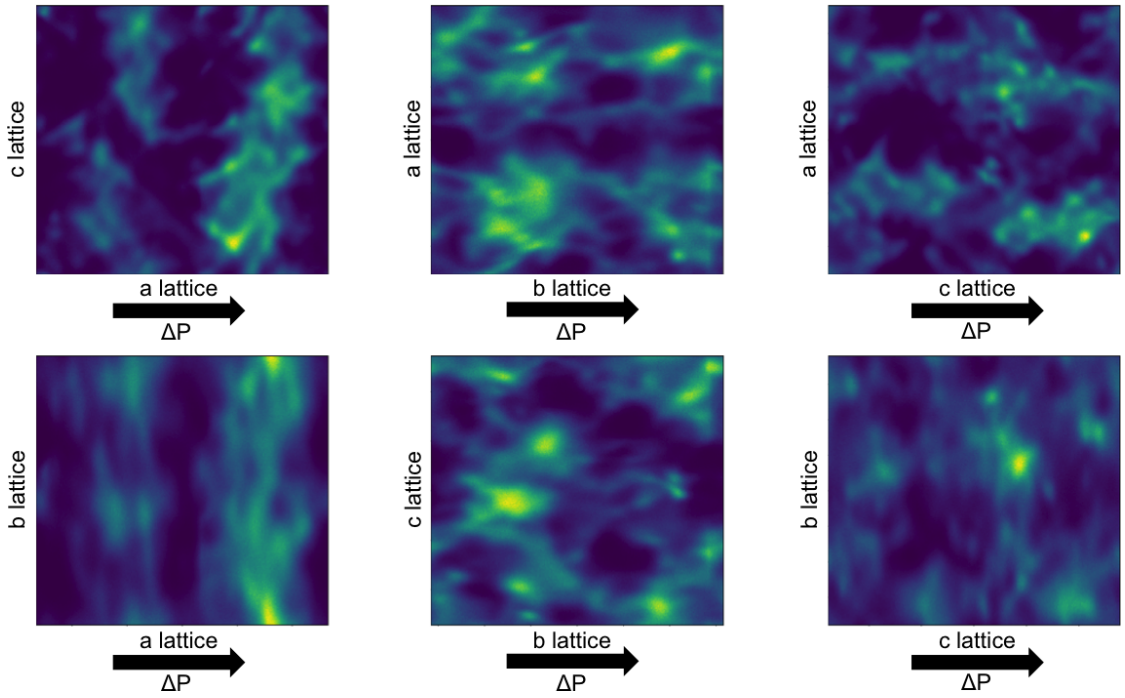

Figure 4.15: Spatial distribution map for BD-NEMD He diffusion at 300 K and 1 atm along the a, b, and c lattice directions. Lighter areas are regions of high occupancy probability. The five unit cells along the pressure-driven direction are consolidated into one unit cell for clarity. Pressure-driven flow along the a direction shows that He aggregates into vertical pockets, while pressure-driven flow along the b and c lattices shows clear diffusion pathways for He.

parameters and elasticity using DFT-derived energy barriers and available experimental results. As computational scientists tackle more challenging materials, we expect this work to provide a roadmap for the successful development of atomistic models.

Our investigation of gas diffusion within COF-505 showed that gas diffusion is sensitive to both particle size, temperature, and pressure. In particular, the flexibility of demetallated COF-505 increases the sensitivity of gas diffusion to pressure. This shows that mechanical stress could be used to tune gas diffusion in woven materials, particularly for smaller gas molecules. Of interest, gases preferentially diffused along the c lattice direction, which is orthogonal to the intersecting molecular threads. This finding could potentially be exploited in the design of new molecular woven materials to help improve either diffusion or selectivity. The high density of the material, which was not particularly apparent in the original paper reporting COF-505, clearly acts as an effective trap for all the small molecules we investigated, which might, as just one possible application, suggest the value of COF-505 as a protective mesh material for personal safety.

CHAPTER 5

CONCLUSIONS AND FUTURE WORK

5.1 Accomplishments

The study of condensed organic molecules continues to inspire research into their properties due to the promise of safe, lower cost alternatives to metallic and organometallic materials. Increasingly, there is a need to expose the mechanical and electronic properties of organic molecules to be defined at the molecular, and even atomic, scale. While experimental methods are continuously being developed and extended to characterize micro- and nano- scale morphologies, computational approaches offer powerful and inimitable research capabilities to provide atomic-level insight. This dissertation has shown how all-atom Molecular Dynamics, coarse-grained Molecular Dynamics, and kinetic Monte Carlo can be used to probe molecular ensembles acting at different time and size scales. By following practices of judicious model verification and validation, these computational methods can not only confirm experimental results, but, more enterprisingly, to drive the design of new organic molecules to satisfy a given set of properties, to explore new research pathways, and to elucidate previously unknown mechanisms or to test posited experimentally derived mechanisms which are invariably difficult to determine in the laboratory. Below, we summarize the main accomplishments of this dissertation.

For the project related to thin film deposition of C_{60} on pentacene, our aim was to accurately simulate heteroepitactical growth and elucidate the role of interface morphology on multilayer growth. To date, there is just one other computational study of heteroepitactical growth in the literature, speaking to the difficulty of

simulating the growth of A on B where A and B have differing preferred crystal habit. Of course, this is by far, the most common situation, and hence there is a continued need to study such systems. Invariably, it is not known, at the outset, how best to conduct such a molecular simulation, using what choice of approach? Chapter 2 tackles that issue. Due to the larger system size and longer time scale of this project, our approach considered the suitability of using two reduced models, kinetic Monte Carlo (kMC) and coarse-grained Molecular Dynamics (CGMD), each with its own advantages and disadvantages. kMC is fast but only once all important energy barriers for events during the process are known (in practise, a very considerable computational burden). It is also invariably a lattice-based model, which is inherently unsuitable for heteroepitactical growth. CGMD is somewhat slower to run than kMC, but its main disadvantage is that it assumes that accurate coarse-grained models exist for the species at hand (as in our case), or that they can be developed (which takes time and care). On the other hand, CGMD has no lattice-based constraints, hence defect generation occurs more naturally.

Our 2nd-generation epitactical KMC code, originally developed by Rebecca Cantrell Stehle for sub-monolayer growth, was significantly extended to allow us to simulate a large system that covered the growth of multiple layers (here, more than six layers) of C_{60} molecules over a pentacene substrate. We were able to validate the model by predicting the growth of C_{60} on C_{60} at high and low temperatures and showed that layer-by-layer growth and island growth could be recovered appropriately similar to the 3-barrier KMC study by Bommel et al. [39]. Similarly, coarse-grained MD simulations for sub-monolayer growth of C_{60} on pentacene were validated against experimental results by Breuer and Witte [24] . Differences between the predictions of film growth between KMC and CGMD became apparent as we compared simulation results over a range of temperatures suggested by experi-

ments. While higher temperature KMC simulations suggest Stranski-Krastenov growth (layer(s) followed by islands), corresponding CGMD simulations showed that C_{60} deposition at a pentacene step edge will yield C_{60} aggregates preferentially along the pentacene step edge. Since pentacene terraces form naturally under experimental conditions, this implies that single crystalline C_{60} thin films may be impossible at high temperatures unless the formation of pentacene terraces can be regulated. Instead, CGMD simulations suggest that the kinetic trapping present at low temperatures will promote smooth but disordered thin film growth. Our CGMD results thus confirm that the roughness of the growth can be influenced by higher temperatures and suggest that the interface morphology will be disordered. Overall, we recommend that future computational studies of heteroepitactic and strained growth use CGMD, which, given a sufficiently accurate coarse-grained potential, appears to accurately simulate the defects promoted in these systems which a lattice-based KMC cannot do.

For the sulfonated oligoTEAs project, we used all-atom Molecular Dynamics to simulate oligomers and characterize their chain dynamics, conformational ensemble and mobility as a function of length of the carbon backbone (2mer to 12mer) and individual monomer functional groups. We expanded experimental understanding by demonstrating how entropic and hydrophobic forces can promote structural collapse of these flexible oligomers. At atomistic time scales, this collapse is stronger than intramolecular electrostatic repulsion, a computational prediction of ours which was validated by experimental results by the Alabi group at Cornell. Our approach balanced the high computational cost of aqueous Molecular Dynamics simulations while still generating value by discerning experimentally unobtainable insight into the ensemble of highly flexible oligoTEAs.

For the Covalent Organic Framework weave project, we characterized and evaluated the properties of a novel organic woven materials using Molecular Dynamics. A considerable effort in this regard was to develop a suitably accurate semi-empirical force field that represents this unique highly flexible material in both its metallated and demetallated versions (the former being an integral part of the chemical synthesis). As yet, there are no known practical applications of COF-505. Our investigation explored the propensity of COF-505 to be suitable for small-molecule gas diffusion within the dense COF-505 matrix. Our results showed that gas diffusion is sensitive to both particle size, temperature, and pressure. In particular, the flexibility of demetallated COF-505 increases the sensitivity of gas diffusion to pressure. This shows that mechanical stress could be used to tune gas diffusion in woven materials, particularly for smaller gas molecules. We found that COF-505 was permeable to H_2 and He but not for larger molecules like H_2O and CO_2. It is particuarly interesting to note our prediction that gases preferentially diffused along a pathway orthogonal to the intersecting molecular threads. This finding could potentially be exploited in the design of new molecular woven materials to help improve either diffusion or selectivity. The high density of this particular material, which was not particularly apparent in the original paper by Yaghi *et al.* that reported the synthesis of COF-505, clearly acts as an effective trap for all the small molecules we investigated, which might, as just one possible application, suggest the value of COF-505 as a protective mesh material for personal safety.

5.2 Future Work

As systems of interest become more specialized and as properties of interest become more dependent on precise atomic configurations, researchers will continue to exploit simulations to overcome the limitations of experimental approaches. Computational chemical and materials scientists must understand the uncertainties in their models and validate them appropriately based on the intended purpose. In this dissertation, I have shown how Density Functional Theory, explicit all-atom Molecular Dynamics, coarse-grained Molecular Dynamics, and kinetic Monte Carlo methods can be leveraged to understand difficult and dynamic problems. Importantly, each of these problems required highly specialized model parameterization. For the C_{60} growth on pentacene project, kinetic Monte Carlo depended heavily on computationally expensive DFT calculations of energy barriers and coarse-grained Molecular Dynamics used force field representations specifically designed for C_{60} molecules. For the sulfonated oligoTEAs project, Molecular Dynamics parameters were compiled from a variety of sources and contexts. For the Covalent Organic Framework weave project, we have created a set of parameters that can be readily incorporated into well-used MD codes, like LAMMPS, for COF-505 that did not exist prior to this thesis. The high density of COF-505, coupled with its elasticity, made this material challenging to model at a semi-empirical level, testing the limits of conventional atomistic simulations. Our approach required simultaneous optimization of lattice parameters and elasticity using DFT-derived energy barriers and available experimental results. The need for macroscopic properties for force field development leveraged methods from the original molecular dynamics parameterization work. The future of molecular modeling will rely on scientists becoming more comfortable with created specialized models, rather than compromising in favor of transferability. In the case of COF-505, this compromise position

was hard to establish and is surely not unique.

In total, this dissertation can be viewed as three case studies that highlight the rigorous methodology and model development that will be required of future molecular scale studies. The model development strategies presented here will be crucial for programs like the Materials Genome Initiative, which seeks to "Integrate experiment, computation, and theory." One-size-fits-all strategies cannot hope to address the breadth and depth required to develop a global materials knowledge base and solve energy, climate change, and health challenges. The rigorous development of specialized force field models will promote reproducible and valuable starting points for an exploration and exploitation of new materials.

APPENDIX A

SELECTED SNAPSHOTS FOR MULTILAYER HETEROEPITACTIC GROWTH OF C_{60} ON PENTACENE

A.1 Multilayer Growth: KMC Results

Figures A.1 and A.2 show initial and final snapshots for KMC simulations of C_{60} on C_{60}, respectively. Figures A.3 and A.4 show final snapshots for KMC simulations of C_{60} on pentacene.

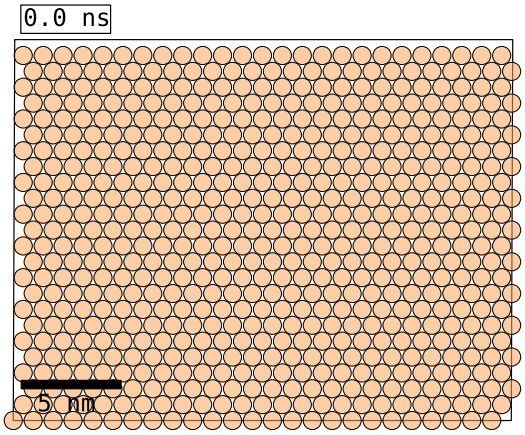

Figure A.1: Initial condition for KMC simulations of C_{60} on C_{60}.

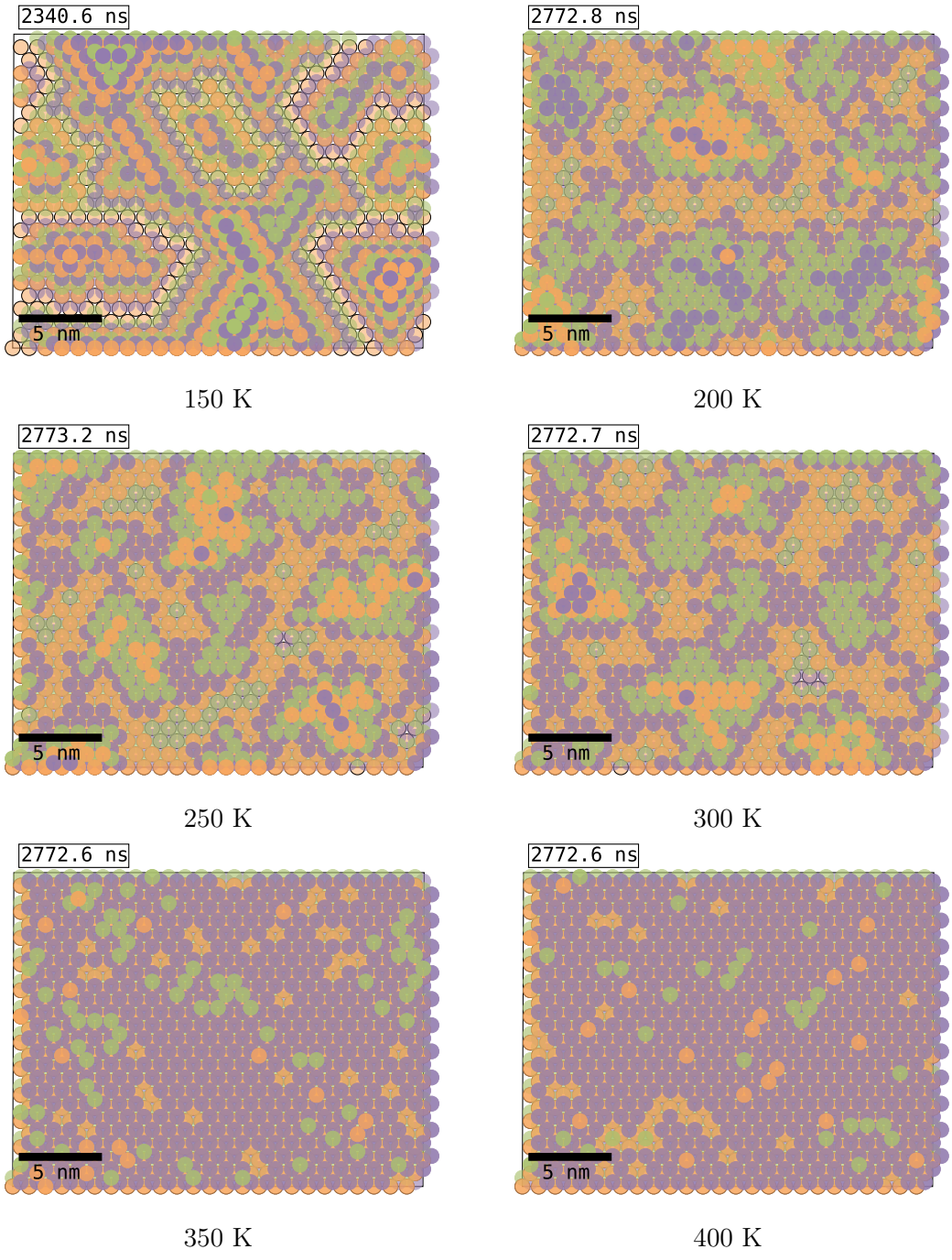

Figure A.2: Final snapshots of KMC Simulations of C_{60} on C_{60}. Lower temperature simulations show the result of an island growth mode, while high temperature simulations show layer-by-layer growth.

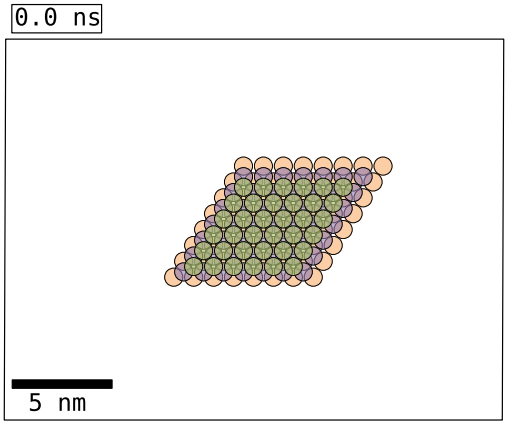

Figure A.3: Initial condition for KMC simulations of C_{60} on Pentacene. An initial island of C_{60} molecules is present to simulate the effects of a pentacene terrace. The island is 3 C_{60} molecules tall to approximate the height of a monolayer high pentacene terrace.

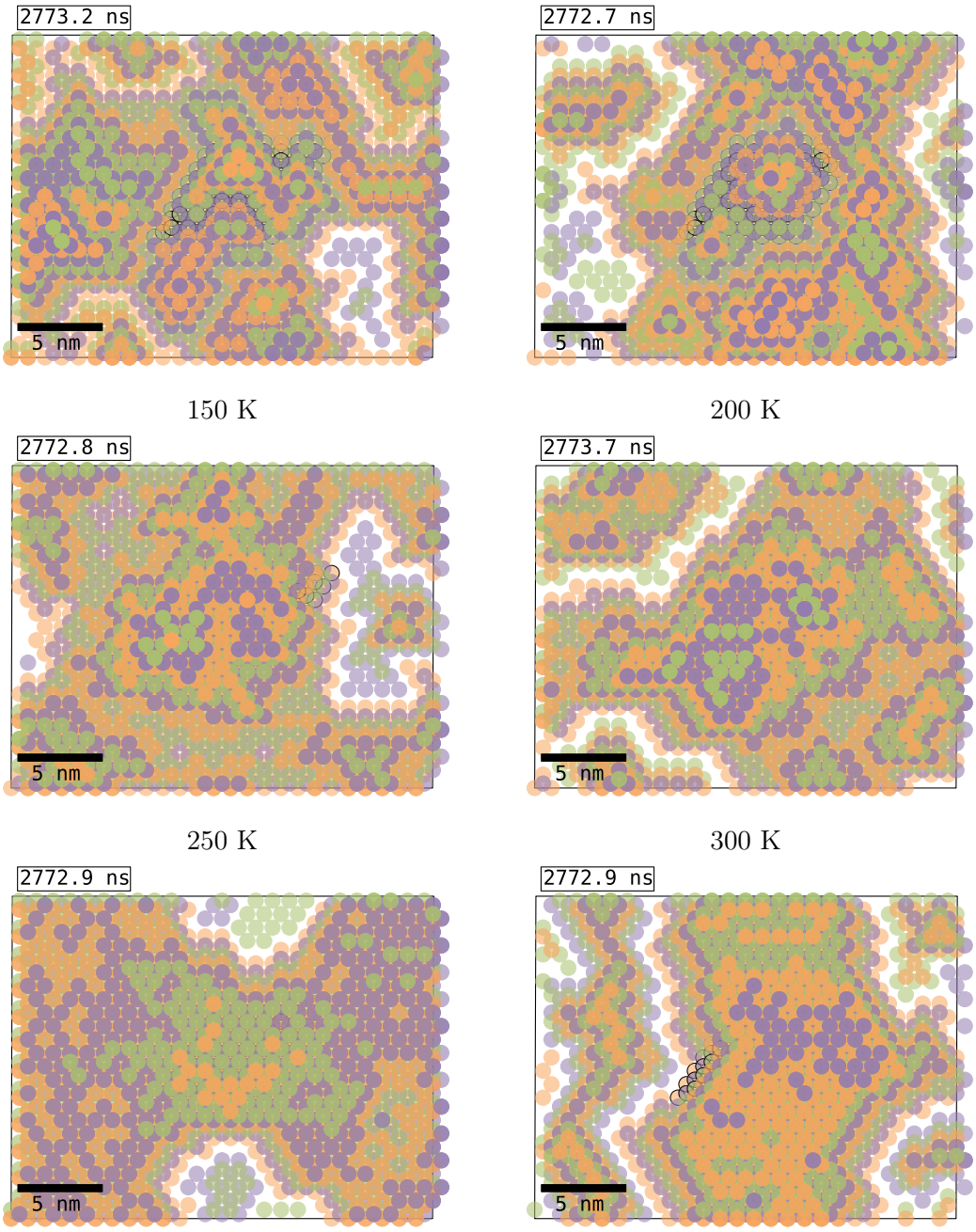

Figure A.4: Final snapshots of KMC simulations of C_{60} on pentacene. Lower temperature simulations show the results of an island growth mode, while high temperature simulations show layer-plus-island growth mode.

A.2 Sub-Monolayer Growth: CGMD Results

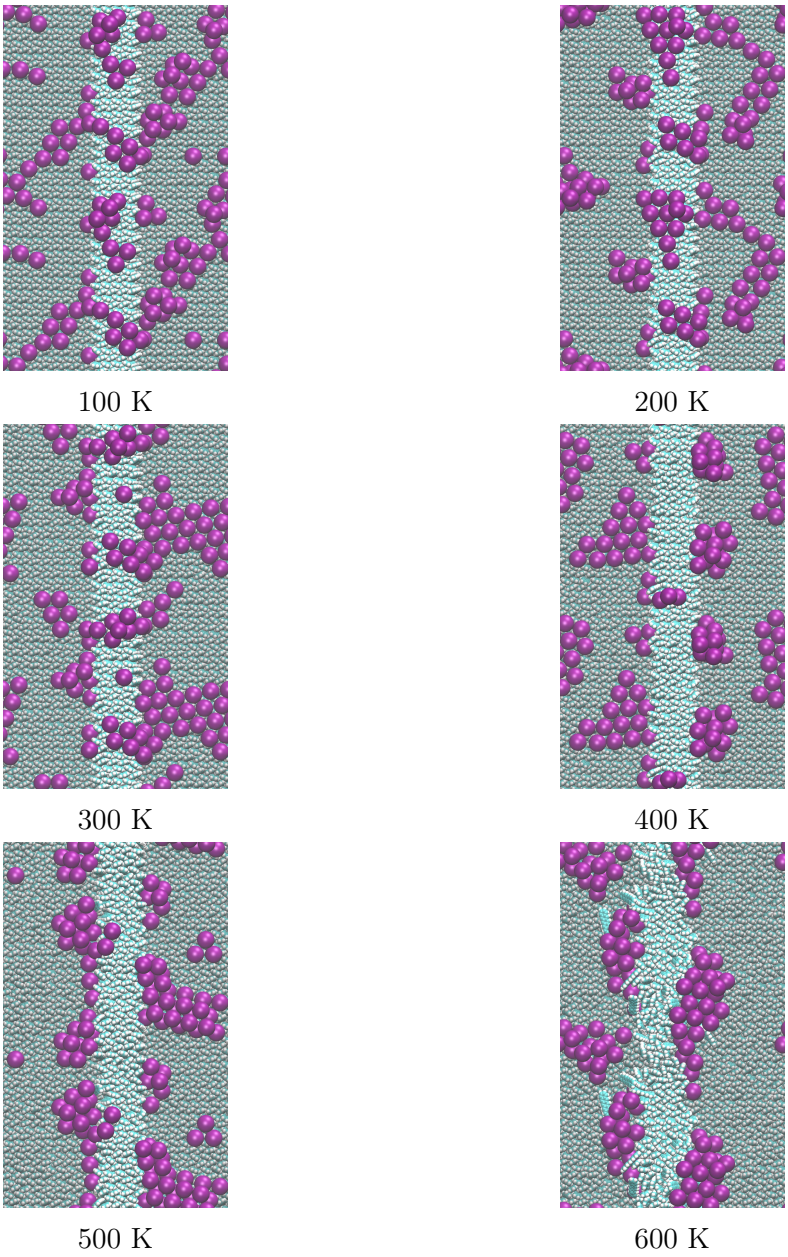

Figure A.5: Final snapshots of CGMD simulations of 0.5 nm C_{60} deposition on pentacene. Lower temperature simulations show the results of an island growth mode with a mostly even distribution of C_{60} molecules, while high temperature simulations show island growth mode with preferential aggregation along the pentacene terrace. The results at 600 K shows the beginnings of disorder as the temperature stability limit is approached.

APPENDIX B

OPLS FORCE FIELD PARAMETERS FOR COF-505

Force field parameters were developed for the OPLS force field to fully simulate COF-505. The atom types and their geometric arrangement for the metallated COF-505 are shown in Figure B.1. All atom types and force field parameters for the demetallated COF-505 are assumed to be identical to the metallated COF-505 unless otherwise shown below.

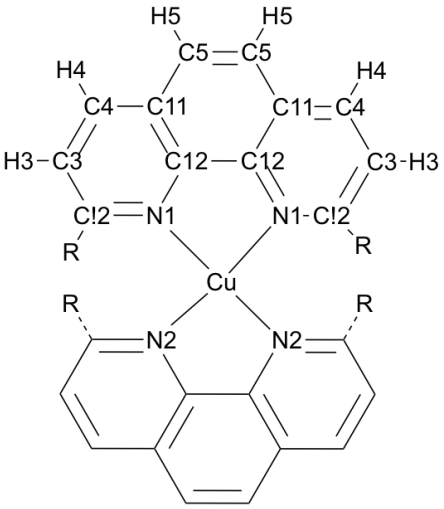

(a) Metallated COF-505 Connector

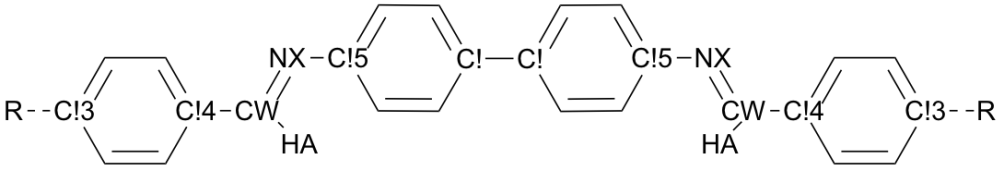

(b) Metallated COF-505 Linker

Figure B.1: OPLS atom types for (a) Metallated COF-505 connector and (b) Metallated COF-505 linker

Table B.1: OPLS Atoms (Connector)

Atom Name	Atom Type	ϵ (kcal/mol)	σ (Å)	q (e)
Cu	Cu	0.2977	1.9724	-0.1808
N1	N1	0.1647	2.8194	-0.2414
N2	N2	0.1647	2.8194	-0.2414
C!2^{M}	C!	0.0789	3.55	0.1759
C3^{M}	CA	0.0805	3.6368	-0.0798
C4^{M}	CA	0.0773	3.55	-0.2641
C5^{M}	CA	0.0616	3.3184	-0.1081
C11^{M}	CA	0.0781	3.55	0.1499
C12^{M}	CA	0.0644	3.109	0.3135
H3^{M}	HA	0.0345	2.42	0.2327
H4^{M}	HA	0.03	2.3073	0.1786
H5^{M}	HA	0.0288	1.8853	0.2843
NC^{D}	NC	0.17	3.25	-0.4472
C!2^{D}	C!	0.07	3.55	0.6033
C3^{D}	CA	0.07	3.55	-0.3535
C4^{D}	CA	0.07	3.55	-0.1327
C5^{D}	CA	0.07	3.55	-0.1797
C11^{D}	CA	0.07	3.55	0.1615
C12^{D}	CA	0.07	3.55	0.2592
H3^{D}	HA	0.03	2.42	0.1932
H4^{D}	HA	0.03	2.42	0.0129
H5^{D}	HA	0.03	2.42	0.2024

^{M} Metallated COF-505; ^{D} Demetallated COF-505;

Table B.2: OPLS Atoms (Linker)

Atom Name	Atom Type	ϵ (kcal/mol)	σ (Å)	q (e)
C!3^M	C!	0.0759	3.6373	0.1403
C!3^D	C!	0.07	3.55	0.1254
C!4	C!	0.0623	3.3871	0.1225
C!5	C!	0.0781	4.1187	-0.3912
NX	NX	0.1644	3.7635	-0.575
CW	CW	0.0508	3.2954	0.1807
HA	HA	0.0267	2.7161	0.0606

^{M} Metallated COF-505; ^{D} Demetallated COF-505;

Table B.3: OPLS Bond Parameters

Bond Type	r_0 (Å)	k_b (kcal mol^{-1} $Angstrom^{-2}$)
CA-CA	1.4	469
CA-HA	1.08	367
CA-NC	1.339	483
CA-CW	1.367	546
CA-C!	1.4	469
HA-CW	1.08	367
NC-C!	1.339	483
CW-C!	1.46	385
CW-NX	1.38	427
C!-C!	1.46	385
C!-N1	1.44	385
C!-N2	1.44	385
Cu-N1	2.093	53.5
Cu-N2	2.093	53.5
NX-C!	1.44	385

Table B.4: OPLS Angle Parameters

Angle Type	θ_0 (°)	k_v (kcal mol^{-1} rad^{-2})
CA-CA-CA	126.7	60
CA-CA-HA	121.9	33.4
CA-CA-NC	118.2	69.8
CA-CA-C!	127	55.1
CA-NC-C!	111.7	67.1
CA-C!-CA	106.5	56.1
CA-C!-NC	124.3	69.5
CA-C!-CW	110.9	61.9
CA-C!-C!	136.6	65
CA-C!-N1 / CA-C!-N2	122.9	67.6
HA-CA-C!	125.9	35.1
NC-C!-C!	138.8	67.1
C!-CW-HA	130.4	35.2
C!-C!-N1 / C!-C!-N2	101.5	62
C!-N1-Cu / C!-N2-Cu	128.1	33.3
NX-C!-CA	125.4	60
N1-Cu-N1 / N2-Cu-N2	-	0
N1-Cu-N2	118.3	5.33

Table B.5: OPLS Dihedral Parameters (kcal mol^{-1})

Dihedral Type	V_1	V_2	V_3	V_4
-CA-CA-	0	9.44	0	0
-CA-NC-	0	6.95	0	0
*-CW-C!-CA	0	2.04	0	0
-CW-N1- / *-CW-N2-*	0	2.19	0	0
-CW-N1- / *-CW-N2-*	0	2.19	0	0
-N1-Cu- / *-N2-Cu-*	0	0	0	0
CA-CA-CW-N1 / CA-CA-CW-N2	0	5.41	0	0
CA-CA-C!-CA	0	6.27	0	0
CA-CA-C!-NC	0	7.58	0	0
CA-CA-C!-C!	0	7.39	0	0
CA-CA-C!-NX	0	6.77	0	0
CA-CA-C!-N1 / CA-CA-C!-N2	0	6.26	0	0
CA-NC-C!-CA	0	7.18	0	0
CA-NC-C!-C!	0	7.25	0	0
CA-C!-C!-CA	0	2.15	0	0
CA-C!-C!-NC	0	2.22	0	0

Table B.6: OPLS Dihedral Parameters 2 (kcal mol^{-1})

Dihedral Type	V_1	V_2	V_3	V_4
CA-C!-C!-N1 / CA-C!-C!-N2	0.95	0.34	10.26	10.6
CA-C!-N1-CW / CA-C!-N2-CW	0	2.19	0	0
CA-C!-N1-Cu / CA-C!-N2-Cu	0	8.00	0	0
HA-CA-C!-CA	0	7.77	0	0
HA-CA-C!-NC	0	7.14	0	0
HA-CA-C!-C!	0	7.24	0	0
HA-CA-C!-N1 / HA-CA-C!-N2	0	7.43	0	0
CW-C!-CA-CA	0	7.15	0	0
CW-C!-CA-HA	0	5.15	0	0
CW-NX-C!-CA	0.64	1.02	7.2	-0.26
CW-N1-C!-C! / CW-N2-C!-C!	0	8.67	0	0
C!-CW-NX-C!	4.17	14.69	-10.09	0.34
C!-C!-N1-Cu / C!-C!-N2-Cu	0	7.1	0	0
C!-NX-CW-HA	3.2	25.96	-4.97	0.35
NX-C!-CA-HA	0	5.37	0	0

APPENDIX C

SELF-DIFFUSION COEFFICIENTS FOR GAS MOLECULES IN COF-505

Single particle gas diffusion simulations were run for He, Ne, Ar, O_2, N_2, H_2O, CO_2, and CH_4 at four temperatures (200 K, 300 K, 400 K, and 500 K) and three pressures (-1000 atm, 1 atm, and 1000 atm) to show the trends and limits in behavior. Data for each gas, temperature and pressure state were collected over 10 ns, totaling 840 ns of simulation time for the study. Self-diffusion coefficients for He at all conditions are shown in Figure 4.9. Self-diffusion coefficients coefficients at all conditions are shown below for Ne (Figure C.1), Ar (Figure C.2), O_2 (Figure C.3), N_2 (Figure C.4), H_2O (Figure C.5), CO_2 (Figure C.6), and CH_4 (Figure C.7). A comparison of all gas molecules studied is shown in Figure C.8.

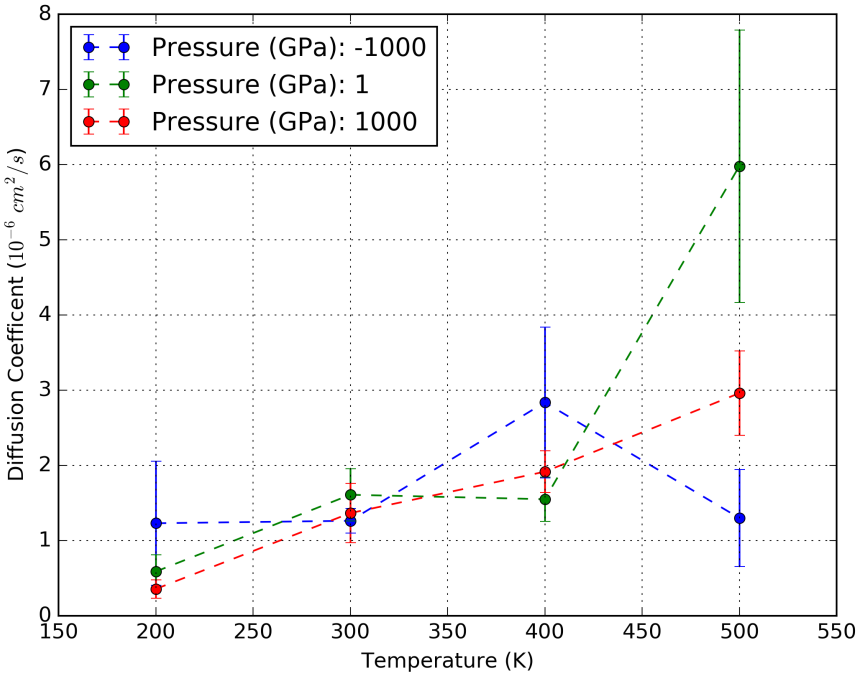

(a) Neon Diffusion in Metallated COF-505

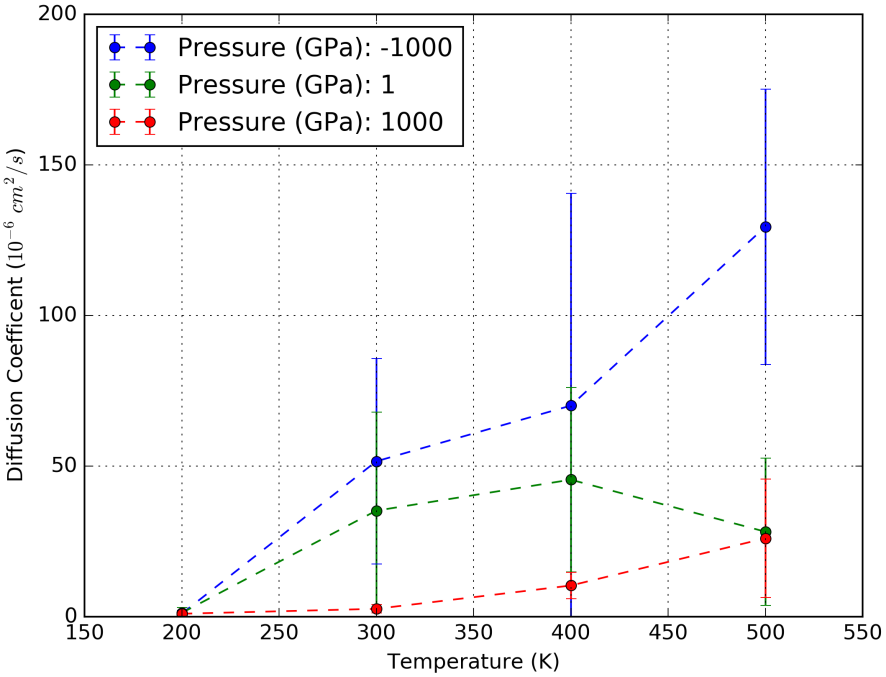

(b) Neon Diffusion in Demetallated COF-505

Figure C.1: The self-diffusion coefficient for neon is shown within (a) metallated COF-505 and (b) demetallated COF-505.

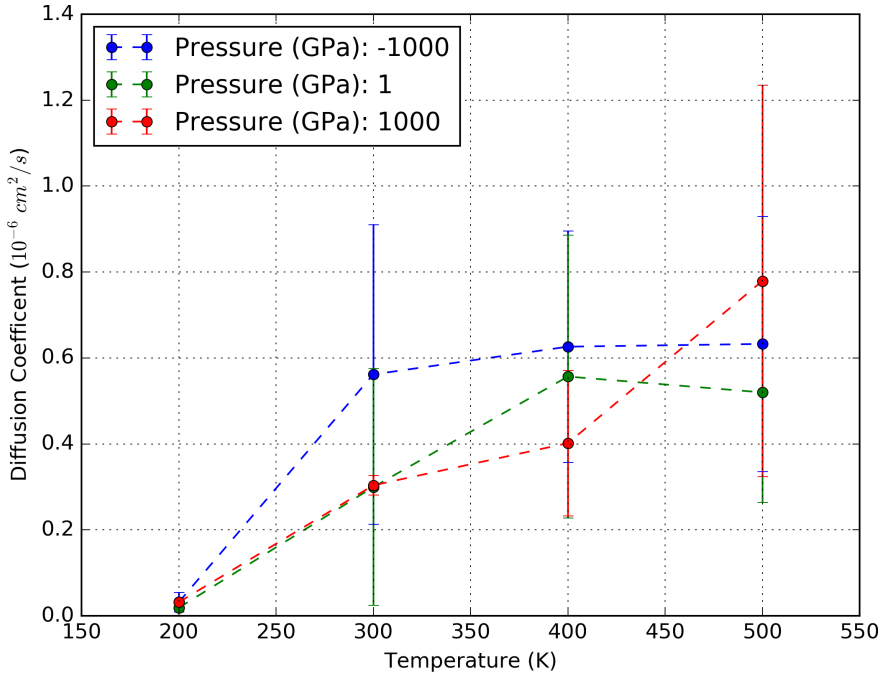

(a) Argon Diffusion in Metallated COF-505

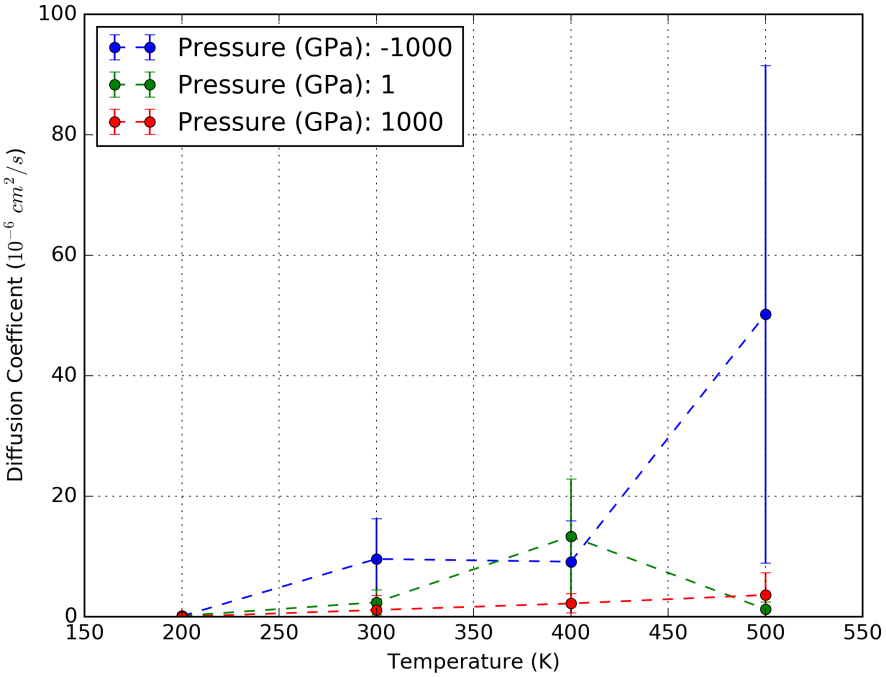

(b) Argon Diffusion in Demetallated COF-505

Figure C.2: The self-diffusion coefficient for argon is shown within (a) metallated COF-505 and (b) demetallated COF-505.

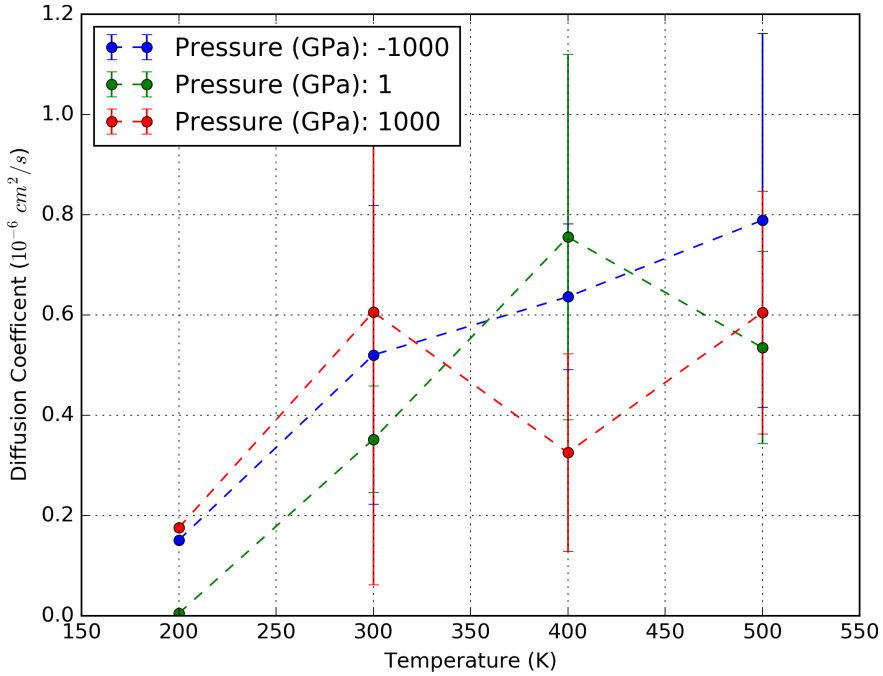

(a) O_2 Diffusion in Metallated COF-505

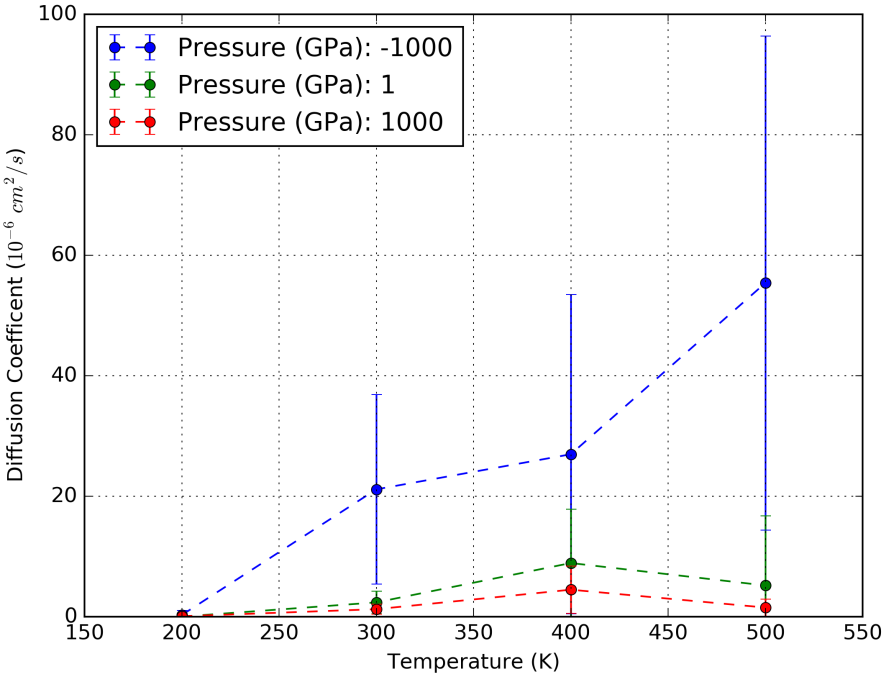

(b) O_2 Diffusion in Demetallated COF-505

Figure C.3: The self-diffusion coefficient for oxygen is shown within (a) metallated COF-505 and (b) demetallated COF-505.

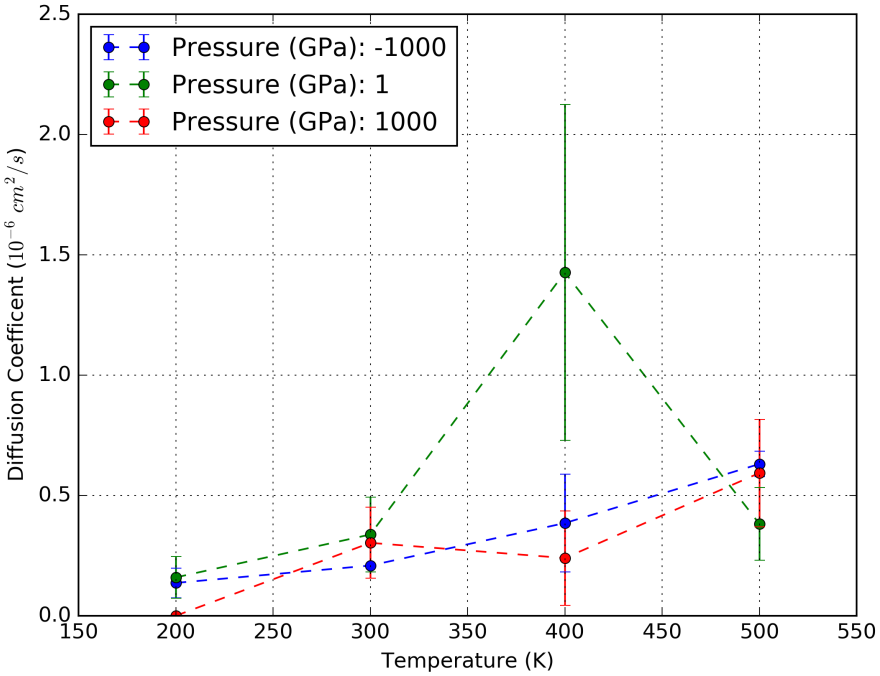

(a) N_2 Diffusion in Metallated COF-505

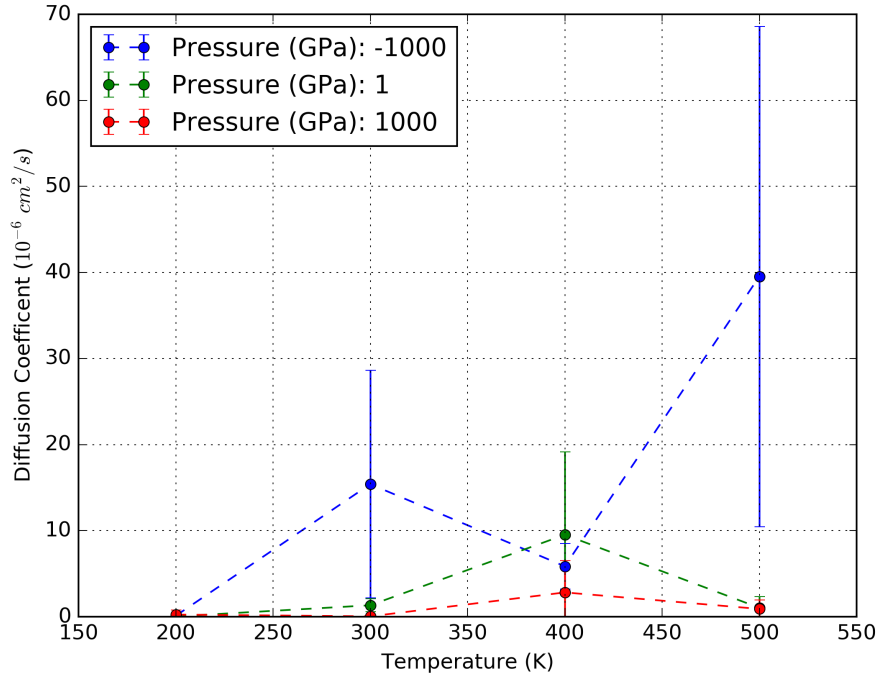

(b) N_2 Diffusion in Demetallated COF-505

Figure C.4: The self-diffusion coefficient for nitrogen is shown within (a) metallated COF-505 and (b) demetallated COF-505.

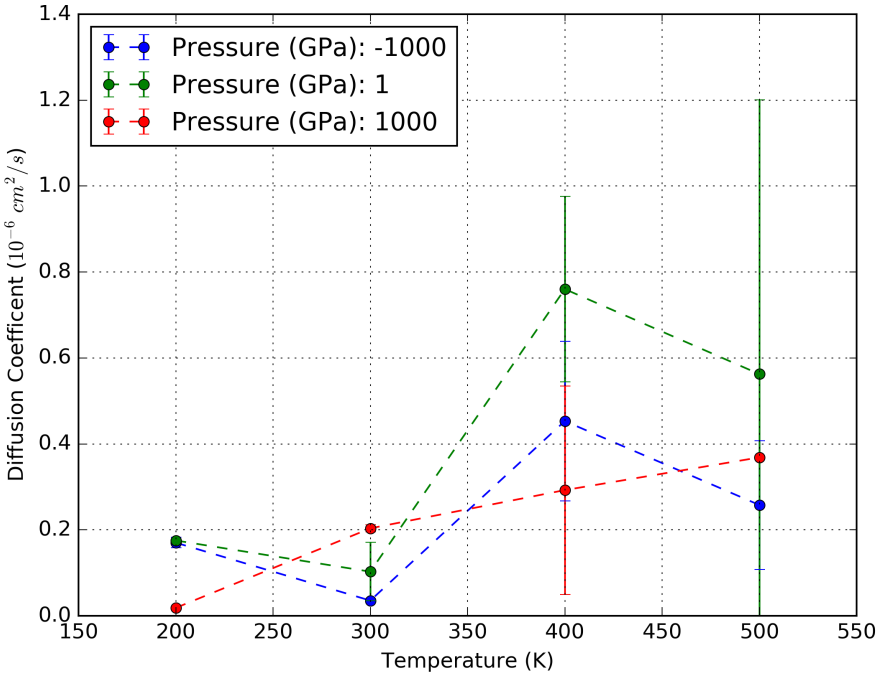

(a) H_2O Diffusion in Metallated COF-505

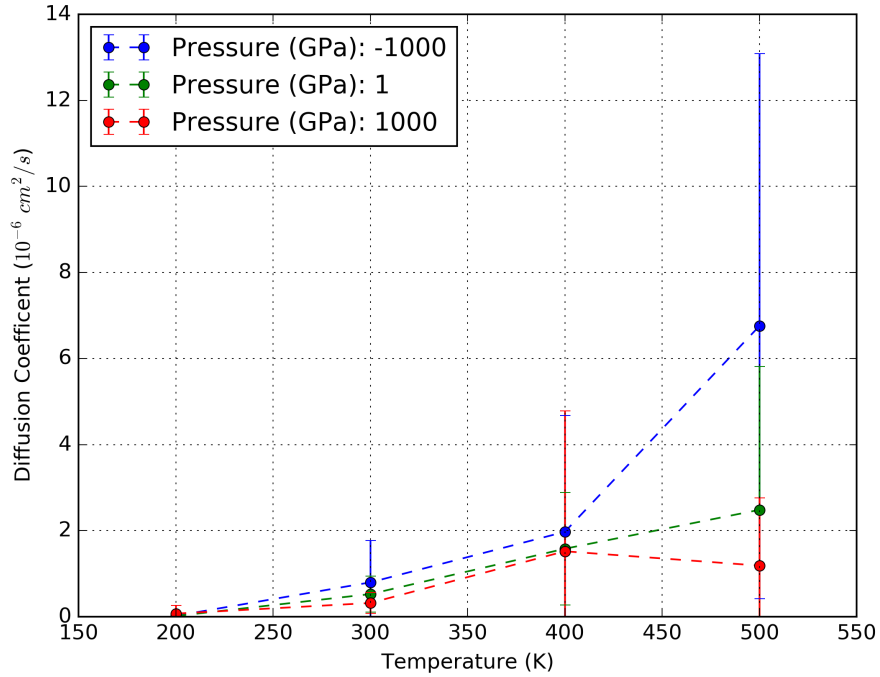

(b) H_2O Diffusion in Demetallated COF-505

Figure C.5: The self-diffusion coefficient for water is shown within (a) metallated COF-505 and (b) demetallated COF-505.

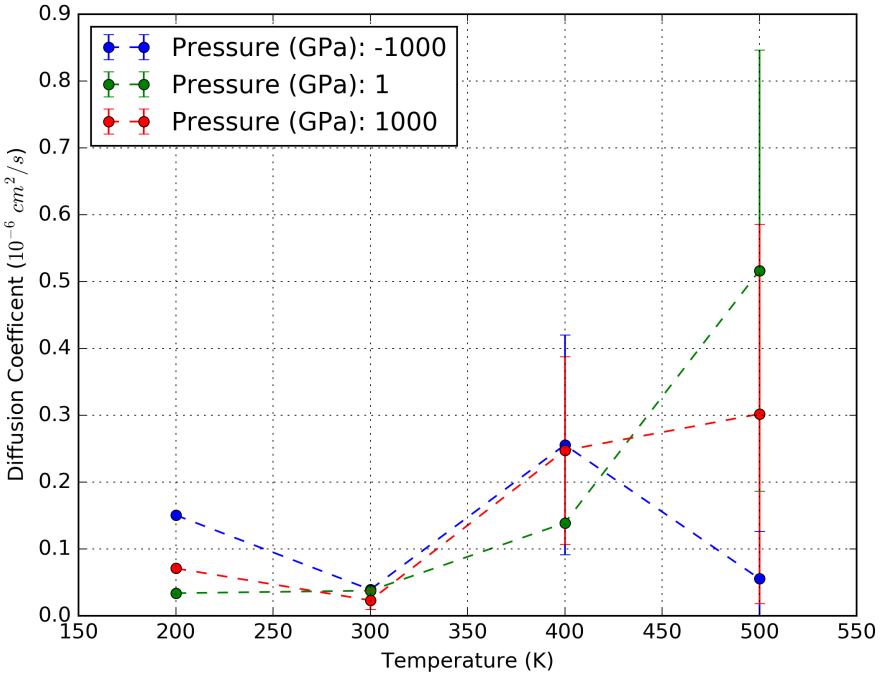

(a) CO_2 Diffusion in Metallated COF-505

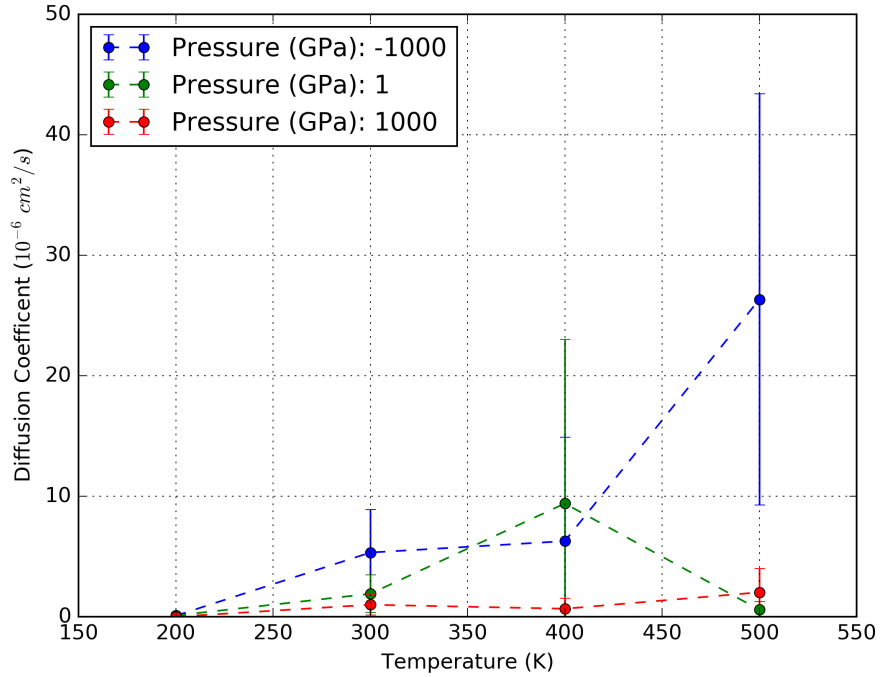

(b) CO_2 Diffusion in Demetallated COF-505

Figure C.6: The self-diffusion coefficient for carbon dioxide is shown within (a) metallated COF-505 and (b) demetallated COF-505.

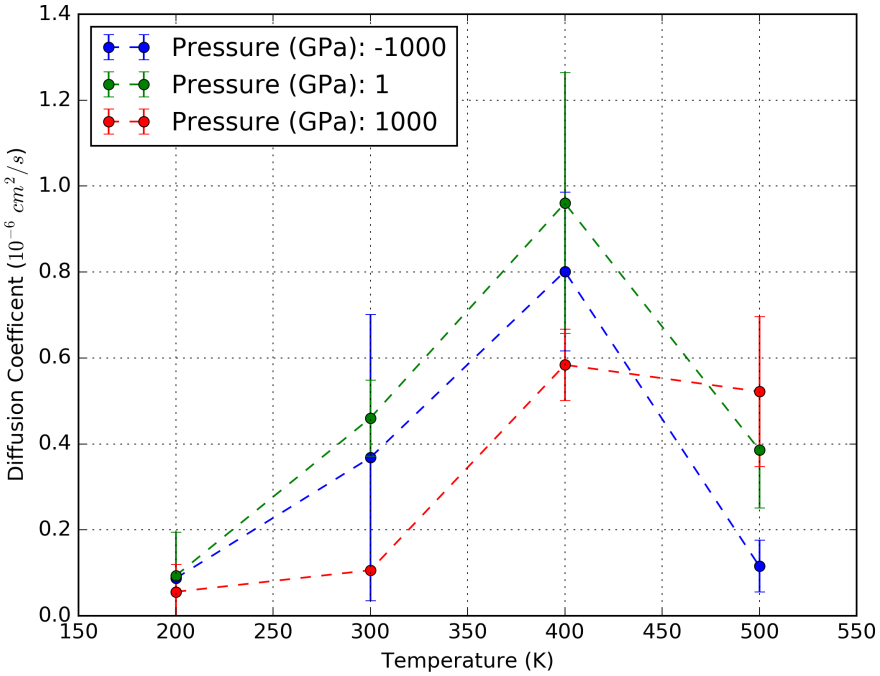

(a) CH_4 Diffusion in Metallated COF-505

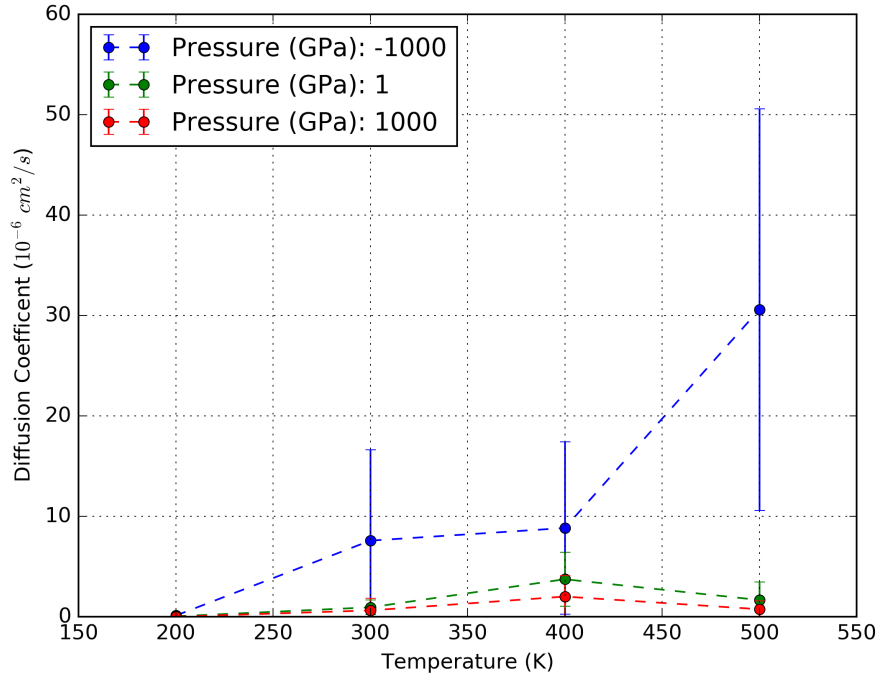

(b) CH_4 Diffusion in Demetallated COF-505

Figure C.7: The self-diffusion coefficient for methane is shown within (a) metallated COF-505 and (b) demetallated COF-505.

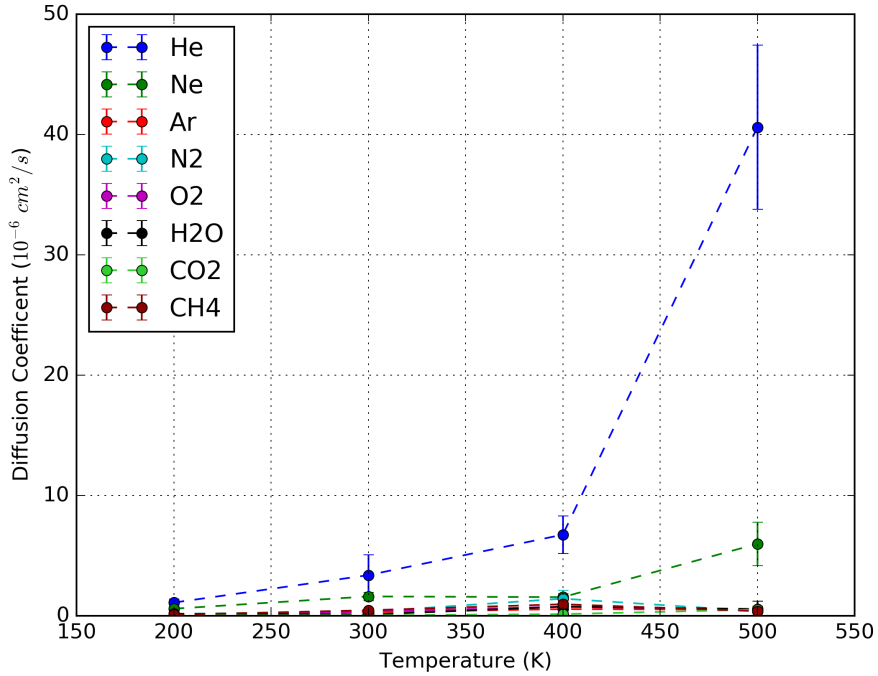

(a) Gas Molecule Diffusion in Metallated COF-505

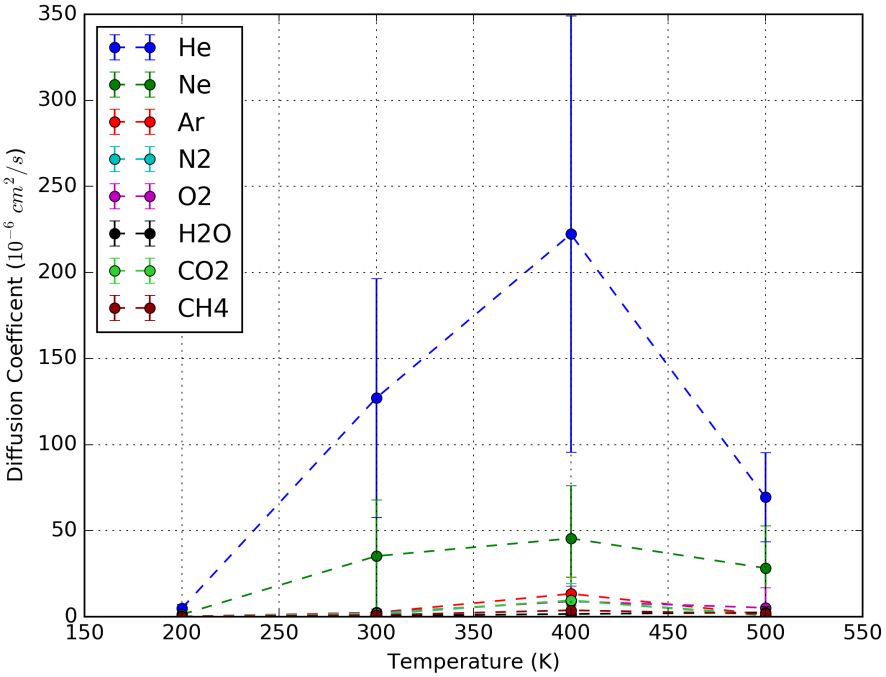

(b) Gas Molecule Diffusion in Demetallated COF-505

Figure C.8: The self-diffusion coefficients for He, Ne, Ar, O_2, N_2, H_2O, CO_2, and CH_4 at 1 atm and 300 K are compared for (a) metallated and (b) demetallated COF-505.

BIBLIOGRAPHY

[1] Cantrell, R. A.; Clancy, P. A New Kinetic Monte Carlo Algorithm for Heteroepitactical Growth: Case Study of C60 Growth on Pentacene. *Journal of Chemical Theory and Computation* **2012**, *8*, 1048–1057.

[2] Brown, J. S.; Acevedo, Y. M.; He, G. D.; Freed, J. H.; Clancy, P.; Alabi, C. A. Synthesis and Solution-Phase Characterization of Sulfonated Oligothioetheramides. *Macromolecules* **2017**, *50*, 8731–8738.

[3] Wikimedia Commons, Ellipsoid: sphere, ellipsoid of revolution, triaxial ellipsoid. 2015; `https://commons.wikimedia.org/wiki/File:Ellipsoide.svg`.

[4] Stehlik, D. E. A. Silinsh: Organic Molecular Crystals, Their Electronic States Springer Series in Solid-State Sciences, Nr. 16, Revidierte Übersetzung der russischen Ausgabe, übersetzt von J. Euduss in Zusammenarbeit mit dem Autor, Springer Verlag, Berlin-Heidelberg-. *Berichte der Bunsengesellschaft für physikalische Chemie* **2010**, *85*, 724–724.

[5] Acevedo, Y. M.; Cantrell, R. A.; Berard, P. G.; Koch, D. L.; Clancy, P. Multiscale Simulation and Modeling of Multilayer Heteroepitactic Growth of C60 on Pentacene. *Langmuir* **2016**, acs.langmuir.5b04500.

[6] Anderson, A. E.; Ellis, B. J.; Weiss, J. A. Verification, validation and sensitivity studies in computational biomechanics. *Computer Methods in Biomechanics and Biomedical Engineering* **2007**, *10*, 171–184.

[7] Zhang, Z.; Lagally, M. G. Atomistic Processes in the Early Stages of Thin-Film Growth. *Science* **1997**, *276*, 377–383.

[8] Evans, J. W.; Thiel, P. A.; Bartelt, M. C. Morphological evolution during epitaxial thin film growth: Formation of 2D islands and 3D mounds. *Surface Science Reports* **2006**, *61*, 1–128.

[9] Petrov, I.; Barna, P. B.; Hultman, L.; Greene, J. E. Microstructural evolution during film growth. *Journal of Vacuum Science & Technology A: Vacuum, Surfaces, and Films* **2003**, *21*, S117.

[10] Virkar, A. A.; Mannsfeld, S.; Bao, Z.; Stingelin, N. Organic Semiconductor Growth and Morphology Considerations for Organic Thin-Film Transistors. *Advanced materials* **2010**, *22*, 3857–3875.

[11] Ruiz, R.; Choudhary, D.; Nickel, B.; Toccoli, T.; Chang, K.-C.; Mayer, A. C.; Clancy, P.; Blakely, J. M.; Headrick, R. L.; Iannotta, S.; Malliaras, G. G. Pentacene Thin Film Growth. *Chemistry of Materials* **2004**, *16*, 4497–4508.

[12] Yang, J.; Yan, D. Weak epitaxy growth of organic semiconductor thin films. *Chem. Soc. Rev.* **2009**, *38*, 2634–2645.

[13] Kowarik, S.; Gerlach, A.; Schreiber, F. Organic molecular beam deposition: fundamentals, growth dynamics, and in situ studies. *Journal of Physics-Condensed Matter* **2008**, *20*.

[14] Witte, G.; Wöll, C. Growth of aromatic molecules on solid substrates for applications in organic electronics. *Journal of Materials Research* **2004**, *19*, 1889–1916.

[15] Yang, F.; Shtein, M.; Forrest, S. R. Controlled growth of a molecular bulk heterojunction photovoltaic cell. *Nature materials* **2005**, *4*, 37–41.

[16] Locklin, J.; Roberts, M. E.; Mannsfeld, S. C. B.; Bao, Z. Optimizing the Thin Film Morphology of Organic Field-Effect Transistors: The Influence of

Molecular Structure and Vacuum Deposition Parameters on Device Performance. *dx.doi.org* **2007**, *46*, 79–101.

[17] Clancy, P. Application of Molecular Simulation Techniques to the Study of Factors Affecting the Thin-Film Morphology of Small-Molecule Organic Semiconductors†. *Chemistry of Materials* **2011**, *23*, 522–543.

[18] Clancy, P. Chemical engineering in the electronics industry: progress towards the rational design of organic semiconductor heterojunctions. *Current Opinion in Chemical Engineering* **2012**, *1*, 117–122.

[19] Schueppel, R.; Schmidt, K.; Uhrich, C.; Schulze, K.; Wynands, D.; Brédas, J.; Brier, E.; Reinold, E.; Bu, H. B.; Baeuerle, P.; Maennig, B.; Pfeiffer, M.; Leo, K. Optimizing organic photovoltaics using tailored heterojunctions: A photoinduced absorption study of oligothiophenes with low band gaps. *Physical Review B* **2008**, *77*, 085311.

[20] Sumpter, B. G.; Meunier, V. Can computational approaches aid in untangling the inherent complexity of practical organic photovoltaic systems? *Journal of Polymer Science Part B-Polymer Physics* **2012**, *50*, 1071–1089.

[21] Yi, Y.; Coropceanu, V.; Brédas, J. L. Exciton-Dissociation and Charge-Recombination Processes in Pentacene/C_{60} Solar Cells: Theoretical Insight into the Impact of Interface Geometry. *Journal of the American Chemical Society* **2009**, *131*, 15777–15783.

[22] Lin, B.-C.; Koo, B. T.; Clancy, P.; Hsu, C.-P. Theoretical Investigation of Charge-Transfer Processes at Pentacene–C 60Interface: The Importance of Triplet Charge Separation and Marcus Electron Transfer Theory. *Journal of Physical Chemistry C* **2014**, *118*, 23605–23613.

[23] Conrad, B. R.; Tosado, J.; Dutton, G.; Dougherty, D. B.; Jin, W.; Bonnen, T.; Schuldenfrei, A.; Cullen, W. G.; Williams, E. D.; Reutt-Robey, J. E.; Robey, S. W. C60 cluster formation at interfaces with pentacene thin-film phases. *Applied Physics Letters* **2009**, *95*, 213302.

[24] Breuer, T.; Witte, G. Diffusion-Controlled Growth of Molecular Heterostructures: Fabrication of Two-, One-, and Zero-Dimensional C60 Nanostructures on Pentacene Substrates. *ACS Applied Materials & Interfaces* **2013**, *5*, 9740–9745.

[25] Hoffman, M. J. CO Oxidation on Palladium Using Multi-Lattice Kinetic Monte Carlo. Ph.D. thesis, 2010.

[26] Cantrell, R.; Clancy, P. A molecular dynamics study of the effect of pentacene polymorphs on C_{60} surface adsorption and diffusional properties and the tendency to form nanowires. *Molecular Simulation* **2010**, *36*, 590–603.

[27] Muccioli, L.; D'Avino, G.; Zannoni, C. Simulation of Vapor-Phase Deposition and Growth of a Pentacene Thin Film on C60 (001). *Advanced materials* **2011**,

[28] Trofimov, V. I.; Mokerov, V. G. Homoepitaxial growth kinetics in the presence of a Schwoebel barrier. *Computational Materials Science* **2000**, *17*, 510–514.

[29] Amassian, A.; Desai, T. V.; Kowarik, S.; Hong, S.; Woll, A. R.; Malliaras, G. G.; Schreiber, F.; Engstrom, J. R. Coverage dependent adsorption dynamics in hyperthermal organic thin film growth. *Journal of Chemical Physics* **2009**, *130*, 124701.

[30] Woll, A. R.; Desai, T. V.; Engstrom, J. R. Quantitative modeling of *in situ* x-ray reflectivity during organic molecule thin film growth. *Physical Review B* **2011**, *84*, 075479.

[31] Tomellini, M.; Fanfoni, M. Mean field approach for describing thin film morphology. *Journal of Physics-Condensed Matter* **2006**, *18*, 4219–4230.

[32] Plimpton, S. Fast parallel algorithms for short-range molecular dynamics. *Journal of Computational Physics* **1995**, *117*, 1–19.

[33] Girifalco, L. A. Interaction potential for carbon (C60) molecules. *The Journal of Physical Chemistry* **1991**, *95*, 5370–5371.

[34] Pacheco, J.; Prates Ramalho, J. First-Principles Determination of the Dispersion Interaction between Fullerenes and Their Intermolecular Potential. *Physical Review Letters* **1997**, *79*, 3873–3876.

[35] Liu, F.-L.; Wang, J. The intermolecular potential function of eSmith-Thakkar type for C-60. *Journal of Molecular Structure-Theochem* **2006**, *778*, 105–109.

[36] Lim, T.-C. United Atom Model Approach for Describing C_{60} Interaction Energy in Molecular Mechanics. *Journal of Theoretical and Computational Chemistry* **2011**, *10*, 423–434.

[37] Jorgensen, W. L.; Maxwell, D. S.; Tiradorives, J. Development and testing of the OPLS all-atom force field on conformational energetics and properties of organic liquids. *Journal of the American Chemical Society* **1996**, *118*, 11225–11236.

[38] Cantrell, R.; Clancy, P. A computational study of surface diffusion of C60 on pentacene. *Surface Science* **2008**, *602*, 3499–3505.

[39] Bommel, S.; Kleppmann, N.; Weber, C.; Spranger, H.; Schäfer, P.; Novak, J.; Roth, S. V.; Schreiber, F.; Klapp, S. H. L.; Kowarik, S. Unravelling the multilayer growth of the fullerene C60 in real time. *Nature Communications* **2014**, *5*, 5388.

[40] Fu, Y. T.; Risko, C.; Brédas, J. L. Intermixing at the Pentacene-Fullerene Bilayer Interface: A Molecular Dynamics Study. *Advanced materials* **2013**, *25*, 878–882.

[41] Kwiatkowski, J. J.; Frost, J. M.; Nelson, J. The Effect of Morphology on Electron Field-Effect Mobility in Disordered C60 Thin Films. *Nano Letters* **2009**, *9*, 1085–1090.

[42] Porel, M.; Brown, J.; Alabi, C. Sequence-Defined Oligothioetheramides. *Synlett* **2015**, *26*, 565–571.

[43] Lutz, J. F.; Ouchi, M.; Liu, D. R.; Sawamoto, M. Sequence-Controlled Polymers. *Science* **2013**, *341*, 1238149–1238149.

[44] Shenogina, N. B.; Tsige, M.; Patnaik, S. S.; Mukhopadhyay, S. M. Molecular modeling of elastic properties of thermosetting polymers using a dynamic deformation approach. *Polymer* **2013**, *54*, 3370–3376.

[45] Griebel, M.; Hamaekers, J. Molecular dynamics simulations of the elastic moduli of polymer–carbon nanotube composites. *Computer Methods in Applied Mechanics and Engineering* **2004**, *193*, 1773–1788.

[46] DuBay, K. H.; Hall, M. L.; Hughes, T. F.; Wu, C.; Reichman, D. R.; Friesner, R. A. Accurate Force Field Development for Modeling Conjugated Polymers. *Journal of Chemical Theory and Computation* **2012**, *8*, 4556–4569.

[47] Singh, M. K.; Ilg, P.; Espinosa-Marzal, R. M.; Kröger, M.; Spencer, N. D. Polymer Brushes under Shear: Molecular Dynamics Simulations Compared to Experiments. *Langmuir* **2015**, *31*, 4798–4805.

[48] Gangemi, F.; Longhi, G.; Abbate, S.; Lebon, F.; Cordone, R.; Ghilardi, G. P.; Fornili, S. L. Molecular Dynamics Simulation of Aqueous Solutions of 26-Unit Segments of p(NIPAAm) and of p(NIPAAm) "Doped" with Amino Acid Based Comonomers. *Journal of Physical Chemistry B* **2008**, *112*, 11896–11906.

[49] Neyertz, S.; Brown, D.; Douanne, A.; Bas, C.; Albérola, N. D. The Molecular Structure and Dynamics of Short Oligomers of PMDA-ODA and BCDA-ODA Polyimides in the Absence and Presence of Water. *Journal of Physical Chemistry B* **2002**, *106*, 4617–4631.

[50] Tesei, G.; Paradossi, G.; Chiessi, E. Poly(vinyl alcohol) Oligomer in Dilute Aqueous Solution: A Comparative Molecular Dynamics Simulation Study. *Journal of Physical Chemistry B* **2012**, *116*, 10008–10019.

[51] Pádua, A. A. H.; Shimizu, K.; Canongia Lopes, J. N. *Molecular Force Field for Ionic Liquids IV:âĂĽ Trialkylimidazolium and Alkoxycarbonyl-Imidazolium Cations; Alkylsulfonate and Alkylsulfate Anions*; American Chemical Society, 2008; Vol. 112.

[52] Canongia Lopes, J. N.; Pádua, A. A. H. CL&P: A generic and systematic force field for ionic liquids modeling. *Theoretical Chemistry Accounts* **2012**, *131*, 1129.

[53] Jorgensen, W. L.; Chandrasekhar, J.; Madura, J. D.; Impey, R. W.;

Klein, M. L. Comparison of simple potential functions for simulating liquid water. *Journal of Chemical Physics* **1983**, *79*, 926–935.

[54] Macchioni, A.; Ciancaleoni, G.; Zuccaccia, C.; Zuccaccia, D. Determining accurate molecular sizes in solution through NMR diffusion spectroscopy. *Chemical Society Reviews* **2008**, *37*, 479–489.

[55] Schulze, B. M.; Watkins, D. L.; Zhang, J.; Ghiviriga, I.; Castellano, R. K. Estimating the shape and size of supramolecular assemblies by variable temperature diffusion ordered spectroscopy. *Organic & Biomolecular Chemistry* **2014**, *12*, 7932–7936.

[56] Perrin, F. Mouvement brownien d'un ellipsoide - I. Dispersion diélectrique pour des molécules ellipsoidales. *Journal de Physique et le Radium* **1934**, *5*, 497–511.

[57] Perrin, F. Mouvement Brownien d'un ellipsoide (II). Rotation libre et dépolarisation des fluorescences. Translation et diffusion de molécules ellipsoidales. *Journal de Physique et le Radium* **1936**, *7*, 1–11.

[58] Koenig, S. H. Brownian motion of an ellipsoid. A correction to Perrin's results. *Biopolymers* **1975**, *14*, 2421–2423.

[59] Ortega, A.; de la Torre, J. G. Hydrodynamic properties of rodlike and disklike particles in dilute solution. *The Journal of Chemical Physics* **2003**, *119*, 9914–9919.

[60] Frenkel, D.; Smit, B. *Understanding molecular simulation: from algorithms to applications*; Elsevier (formerly published by Academic Press), 2002; Vol. 1.

[61] Liu, Y.; Ma, Y.; Zhao, Y.; Sun, X.; Gándara, F.; Furukawa, H.; Liu, Z.; Zhu, H.; Zhu, C.; Suenaga, K.; Oleynikov, P.; Alshammari, A. S.; Zhang, X.; Terasaki, O.; Yaghi, O. M. Weaving of organic threads into a crystalline covalent organic framework. *Science* **2016**, *351*, 365–369.

[62] Champsaur, A. M.; Mézière, C.; Allain, M.; Paley, D. W.; Steigerwald, M. L.; Nuckolls, C.; Batail, P. Weaving Nanoscale Cloth through Electrostatic Templating. *Journal of the American Chemical Society* **2017**, *139*, 11718–11721.

[63] Zhao, Y.; Guo, L.; Gándara, F.; Ma, Y.; Liu, Z.; Zhu, C.; Lyu, H.; Trickett, C. A.; Kapustin, E. A.; Terasaki, O.; Yaghi, O. M. A Synthetic Route for Crystals of Woven Structures, Uniform Nanocrystals, and Thin Films of Imine Covalent Organic Frameworks. *Journal of the American Chemical Society* **2017**, jacs.7b07457.

[64] Rungtaweevoranit, B.; Diercks, C. S.; Kalmutzki, M. J.; Yaghi, O. M. Spiers Memorial Lecture: : Progress and prospects of reticular chemistry. *Faraday Discuss.* **2017**, *201*, 9–45.

[65] Côté, A. P.; Benin, A. I.; Ockwig, N. W.; O'Keeffe, M.; Matzger, A. J.; Yaghi, O. M. Porous, Crystalline, Covalent Organic Frameworks. *Science* **2005**, *310*, 1166–1170.

[66] El-Kaderi, H. M.; Hunt, J. R.; Mendoza-Cortes, J. L.; Côté, A. P.; Taylor, R. E.; O'Keeffe, M.; Yaghi, O. M. Designed Synthesis of 3D Covalent Organic Frameworks. *Science* **2007**, *316*, 268–272.

[67] Yu, J.-T.; Chen, Z.; Sun, J.; Huang, Z.-T.; Zheng, Q.-Y. Cyclotricatechylene based porous crystalline material: Synthesis and applications in gas storage. *Journal of Materials Chemistry* **2012**, *22*, 5369–5373.

[68] Li, Y.; Yang, R. T. Hydrogen storage in metal-organic and covalent-organic frameworks by spillover. *AIChE Journal* **2007**, *54*, 269–279.

[69] Furukawa, H.; Yaghi, O. M. Storage of Hydrogen, Methane, and Carbon Dioxide in Highly Porous Covalent Organic Frameworks for Clean Energy Applications. *Journal of the American Chemical Society* **2009**, *131*, 8875–8883.

[70] Spitler, E. L.; Dichtel, W. R. Lewis acid-catalysed formation of two-dimensional phthalocyanine covalent organic frameworks. *Nature Chemistry* **2010**,

[71] Ding, S. Y.; Gao, J.; Wang, Q.; Zhang, Y. Construction of Covalent Organic Framework for Catalysis: Pd/COF-LZU1 in Suzuki–Miyaura Coupling Reaction. *Journal of the American Chemical Society* **2011**,

[72] Dalapati, S.; Jin, S.; Gao, J.; Xu, Y.; Nagai, A.; Jiang, D. An Azine-Linked Covalent Organic Framework. *Journal of the American Chemical Society* **2013**, *135*, 17310–17313.

[73] Smit, B.; Maesen, T. L. M. Molecular Simulations of Zeolites: Adsorption, Diffusion, and Shape Selectivity. *Chemical Reviews* **2008**, *108*, 4125–4184.

[74] Skoulidas, A. I.; David S Sholl, *Self-Diffusion and Transport Diffusion of Light Gases in Metal-Organic Framework Materials Assessed Using Molecular Dynamics Simulations*; American Chemical Society, 2005; Vol. 109.

[75] Skoulidas, A. I.; Sholl, D. S. *Molecular Dynamics Simulations of Self-Diffusivities, Corrected Diffusivities, and Transport Diffusivities of Light Gases in Four Silica Zeolites To Assess Influences of Pore Shape and Connectivity*; American Chemical Society, 2003; Vol. 107.

[76] Koo, B. T.; Clancy, P. Towards optimal packing and diffusion of fullerene molecules in the Pc-PBBA covalent organic framework. *Molecular Simulation* **2014**, *40*, 58–70.

[77] Mayo, S. L.; Olafson, B. D.; Goddard, W. A. DREIDING: a generic force field for molecular simulations. **2002**,

[78] MacKerell Jr., A. D. et al. All-Atom Empirical Potential for Molecular Modeling and Dynamics Studies of Proteins †. *Journal of Physical Chemistry B* **1998**, *102*, 3586–3616.

[79] Canongia Lopes, J. N.; Agílio A H Pádua, *Molecular Force Field for Ionic Liquids III:âĂĽ Imidazolium, Pyridinium, and Phosphonium Cations; Chloride, Bromide, and Dicyanamide Anions*; American Chemical Society, 2006; Vol. 110.

[80] Dahlgren, M. K.; Schyman, P.; Tirado-Rives, J.; Jorgensen, W. L. Characterization of Biaryl Torsional Energetics and its Treatment in OPLS All-Atom Force Fields. *Journal of Chemical Information and Modeling ()* **2013**, *53*, 1191–1199.

[81] Robertson, M. J.; Tirado-Rives, J.; Jorgensen, W. L. Improved peptide and protein torsional energetics with the OPLS-AA force field. *Journal of Chemical Theory and Computation* **2015**, *11*, 3499–3509.

[82] Fang, H.; Demir, H.; Kamakoti, P.; Sholl, D. S. Recent developments in first-principles force fields for molecules in nanoporous materials. *J. Mater. Chem. A* **2014**, *2*, 274–291.

[83] Heinz, H.; Lin, T.-J.; Kishore Mishra, R.; Emami, F. S. Thermodynamically Consistent Force Fields for the Assembly of Inorganic, Organic, and Bio-

logical Nanostructures: The INTERFACE Force Field. *Langmuir* **2013**, *29*, 1754–1765.

[84] Coupry, D. E.; Addicoat, M. A.; Heine, T. Extension of the Universal Force Field for Metal–Organic Frameworks. *Journal of Chemical Theory and Computation* **2016**, *12*, 5215–5225.

[85] Neumann, M. A. Tailor-Made Force Fields for Crystal-Structure Prediction. *Journal of Physical Chemistry B* **2008**, *112*, 9810–9829.

[86] Svard, M.; Rasmuson, A. C. Force Fields and Point Charges for Crystal Structure Modeling. *Industrial & Engineering Chemistry Research* **2009**, *48*, 2899–2912.

[87] Marcon, V.; Raos, G. Molecular modeling of crystalline oligothiophenes: Testing and development of improved force fields. *Journal of Physical Chemistry B* **2004**, *108*, 18053–18064.

[88] Koo, B. T.; Dichtel, W. R.; Clancy, P. A classification scheme for the stacking of two-dimensional boronate ester-linked covalent organic frameworks . *Journal of Materials Chemistry* **2012**, *22*, 17460–17469.

[89] Heinz, H.; Suter, U. W. Atomic Charges for Classical Simulations of Polar Systems. *Journal of Physical Chemistry B* **2004**, *108*, 18341–18352.

[90] Besler, B. H.; Merz, K. M.; Kollman, P. A. Atomic charges derived from semiempirical methods. *Journal of Computational Chemistry* **1990**, *11*, 431–439.

[91] Sigfridsson, E.; Ryde, U. Comparison of methods for deriving atomic charges from the electrostatic potential and moments. *Journal of Computational Chemistry* **1998**, *19*, 377–395.

[92] Goerigk, L.; Grimme, S. A thorough benchmark of density functional methods for general main group thermochemistry, kinetics, and noncovalent interactions. *Physical Chemistry Chemical Physics* **2011**, *13*, 6670–6688.

[93] Neese, F. The ORCA program system. *Wiley Interdisciplinary Reviews: Computational Molecular Science* **2012**, *2*, 73–78.

[94] Deeth, R. J.; Hearnshaw, L. J. A. Molecular modelling for coordination compounds: Cu(ii)– amine complexes. *Dalton Transactions* **2005**, *0*, 3638–3645.

[95] Deeth, R. J.; Anastasi, A.; Diedrich, C.; Randell, K. Molecular modelling for transition metal complexes: Dealing with d-electron effects. *Coordination Chemistry Reviews* **2009**, *253*, 795–816.

[96] Harder, E. et al. OPLS3: A Force Field Providing Broad Coverage of Drug-like Small Molecules and Proteins. *Journal of Chemical Theory and Computation* **2016**, *12*, 281–296.

[97] Moreno, M.; Casalegno, M.; Raos, G.; Meille, S. V.; Po, R. Molecular Modeling of Crystalline Alkylthiophene Oligomers and Polymers. *Journal of Physical Chemistry B* **2010**, *114*, 1591–1602.

[98] Jorgensen, W. L.; Tiradorives, J. The Opls Potential Functions for Proteins - Energy Minimizations for Crystals of Cyclic-Peptides and Crambin. *Journal of the American Chemical Society* **1988**, *110*, 1657–1666.

[99] Halgren, T. A. Merck molecular force field. I. Basis, form, scope, parameterization, and performance of MMFF94. *Journal of Computational Chemistry* **1996**, *17*, 490–519.

[100] Wang, J.; Wolf, R. M.; Caldwell, J. W.; Kollman, P. A.; Case, D. A. Development and testing of a general amber force field. *Journal of Computational Chemistry* **2004**, *25*, 1157–1174.

[101] Han, Y.; Elliott, J. Molecular dynamics simulations of the elastic properties of polymer/carbon nanotube composites. *Computational Materials Science* **2007**, *39*, 315–323.

[102] Johnson, S. G. The NLopt nonlinear-optimization package. **2014**,

[103] Powell, M. J. D. Direct search algorithms for optimization calculations. *Acta Numerica* **2008**, *7*, 287–336.

[104] Rowan, T. H. Functional stability analysis of numerical algorithms. **1990**,

[105] Kaelo, P.; Ali, M. M. Some variants of the controlled random search algorithm for global optimization. *Journal of Optimization Theory and Applications* **2006**, *130*, 253–264.

[106] Klein, M. L.; Levesque, D.; Weis, J. J. Molecular-dynamics study of solid γ-O_2. *Physical Review B* **1980**, *21*, 5785–5792.

[107] Murthy, C. S.; Singer, K.; Klein, M. L.; McDonald, I. R. Pairwise additive effective potentials for nitrogen. *Molecular Physics* **2006**, *41*, 1387–1399.

[108] Arora, G.; Sandler, S. I. Mass Transport of O_2 and N_2 in Nanoporous Carbon (C_{168} Schwarzite) Using a Quantum Mechanical Force Field and Molecular Dynamics Simulations. *Langmuir* **2006**, *22*, 4620–4628.

[109] Harris, J. G.; Yung, K. H. Carbon Dioxide's Liquid-Vapor Coexistence Curve and Critical Properties as Predicted by a Simple Molecular Model. *Journal of Physical Chemistry* **1995**,

[110] Bird, R. B.; Stewart, W. E.; Lightfoot, E. N. *Transport Phenomena, 2nd ed.*; Wiley: New York, 2002.

[111] Frentrup, H.; Avendaño, C.; Horsch, M.; Salih, A.; Müller, E. A. Transport diffusivities of fluids in nanopores by non-equilibrium molecular dynamics simulation. *Molecular Simulation* **2012**, *38*, 540–553.

[112] Turgman-Cohen, S.; Araque, J. C.; Hoek, E. M. V.; Escobedo, F. A. Molecular Dynamics of Equilibrium and Pressure-Driven Transport Properties of Water through LTA-Type Zeolites. *Langmuir* **2013**, *29*, 12389–12399.

[113] Daly, K. B.; Benziger, J. B.; Panagiotopoulos, A. Z.; Debenedetti, P. G. Molecular Dynamics Simulations of Water Permeation across Nafion Membrane Interfaces. *Journal of Physical Chemistry B* **2014**, *118*, 8798–8807.

[114] Frentrup, H.; Hart, K.; Colina, C.; Müller, E. In Silico Determination of Gas Permeabilities by Non-Equilibrium Molecular Dynamics: CO2 and He through PIM-1. *Membranes* **2015**, *5*, 99–119.

[115] Collell, J.; Galliero, G.; Vermorel, R.; Ungerer, P.; Yiannourakou, M.; Montel, F.; Pujol, M. Transport of Multicomponent Hydrocarbon Mixtures in Shale Organic Matter by Molecular Simulations. *Journal of Physical Chemistry C* **2015**, *119*, 22587–22595.

[116] Boţan, A.; Vermorel, R.; Ulm, F.-J.; Pellenq, R. J. M. Molecular Simulations of Supercritical Fluid Permeation through Disordered Microporous Carbons. *Langmuir* **2013**, *29*, 9985–9990.

[117] Martínez, L.; Andrade, R.; Birgin, E. G.; Martínez, J. M. PACKMOL - A package for building initial configurations for molecular dynamics simulations. *Journal of Computational Chemistry* **2009**, *30*, 2157–2164.